2024

Simplification of high graphene/n-Si Schottky junction solar efficiency

AL Busaidi, HILAL

COPYRIGHT STATEMENT

[1] *E.g.* in the example of third party copyright materials reused in the thesis.
[2] In accordance with best practice principles such as, *Marking/Creators/Marking third party content* (2013). Available from: https://wiki.creativecommons.org/wiki/Marking/Creators/Marking_third_party_content [accessed 28th February 2022]

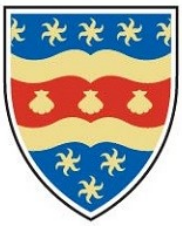

UNIVERSITY OF PLYMOUTH

Simplification of high graphene/n-Si Schottky junction solar efficiency

by

HILAL ALBUSAIDI

A thesis submitted to the University of Plymouth in partial fulfilment of the degree of

DOCTOR OF PHILOSOPHY

School of Engineering, Computing and Mathematics

September 2024

Acknowledgements

First, I would like to thank Allah (God) for giving me the time, opportunity, capability and strength to undertake this study and do my ultimate best to complete it.

I want to thank my supervisors, Dr David, Professor Pan and Dr. Ahmed, for the support and patience they have shown me throughout the research. Thanks should also go to my colleagues, Mr Fry and Dr Suhail, who were generous with their time and assistance during the study.

My acknowledgements would be incomplete without thanking the most significant source of my strength, my family and my wife. Thank you for encouraging me in my pursuits and inspiring me to follow my dreams. I am incredibly grateful to my parents for their support and never-ending love.

Author's Declaration

At no time during the registration for the degree of Doctor of Philosophy has the author been registered for any other University award without prior agreement of the Doctoral College Quality Sub-Committee.

Work submitted for this research degree at Plymouth University has not formed part of any other degree either at Plymouth University or at another establishment.

This study was financed with the aid of a scholarship from the government of Oman.

Relevant conferences were attended at which work was often presented and several papers prepared for publication.

Publications:

1. Al Busaidi, Hilal, Ahmed Suhail, David Jenkins, and Genhua Pan. (2023): "Developed graphene/Si Schottky junction solar cells based on the top-window structure." Carbon Trends Volume 10, 100247.

   DOI: https://doi.org/10.1016/j.cartre.2023.100247

   Link: https://www.sciencedirect.com/science/article/pii/S2667056923000020

2. Al Busaidi, Hilal, Ahmed Suhail, David Jenkins, and Genhua Pan. (2024): " Remarkable enhancement of graphene/Si Schottky junction solar cell performance with effective chemical treatments." Materials Chemistry and Physics, Volume 316

   DOI: https://doi.org/10.1016/j.matchemphys.2024.129101

   Link: https://www.sciencedirect.com/science/article/abs/pii/S0254058424002268

Presentations at conferences:

1. Al Busaidi, Hilal, Ahmed Suhail, Genhua Pan, David Jenkins, 48th Annual National Solar Conference (ASES SOLAR 2019), Minneapolis, USA, (2019).
2. Al Busaidi, Hilal, Ahmed Suhail, Genhua Pan, David Jenkins, Kamrul Islam, Effect of PMMA residue on the *J-V* behaviour of graphene/Si Schottky junction solar cell, Middle East Energy 2023, Dubai, United Arab Emirates, (2023).

Word count of main body of thesis: 29,151 words

Signed: Hilal AL Busaidi

Date: 26/09/2024

Abstract

Hilal Badar Saif Al Busaidi

Simplification of high graphene/n-Si Schottky junction solar efficiency.

Because of the outstanding properties of graphene such as optical transmission and mobility of charges [1], it incorporates to Schottky solar cells. These properties of graphene also reduces the optical and electrical losses which are in solar cells made of p-n structures. To increase the performance of electronic devices, researchers developed 3 designs using graphene with silicon solar cell technology. Schottky junction solar cells made of graphene and n-silicon have attained efficiency values comparable to p-n junction silicon solar cells. Nevertheless, issues remain such as how to simplify the creating process to improve the fill factor and stability of devices. This doctoral study will focus on various phases of the progression of graphene/silicon solar cells toward greater efficiency and stability. The study will discuss the simplicity of top-window-structured graphene/n-Si Schottky junction photovoltaic devices. It will also deal with developing the fill factor and stability of devices. Until now, top window devices have required complex preparation processes for SiO_2 including etching a part of it to create the top window design. To accomplish the process, a simple method of sputtering to form coated SiO_2 layers has been developed and will be described in this study. The thickness of SiO_2 is thoroughly investigated to constitute an effective top window design. This research is also conducted to enhance the fill factor of samples after introducing multi-graphene layers which form

the Schottky junction. This was achieved after decreasing the amount of PMMA residue by developed techniques such as annealing, DUV and chemical treatments.

Evaporation of chemical dopants which was another problem that causes low stability of doped devices within a week. It was found in this work that a layer of PMMA coated onto prepared devices significantly improves the stability of doped samples.

List of Contents

List of Tables

List of Figures

List of Abbreviations

a - Lattice unit vector

AFM - Atomic force microscope

AM - Air mass

α - Absorption coefficient

B - Coefficient of radiative recombination

BSR - Back Surface Reflector

BSRV - Back Surface Recombination Velocity

CVD - Chemical vapour deposition

DI - Deionised

DLAR - Double layer anti-reflection coating

DUV - Deep UV

E_g - Energy gap

EQE - External Quantum efficiency

FET - Field effect transistor

FF - Fill Factor

Φ_B - Schottky barrier height

GO - Graphene Oxide

HIT - Heterojunction intrinsic thin-layer

I - Current

I_{Dark} - Dark current

I_L - Light current

J_{SC} - Short circuit current density

□- Wavelength

MGL - multi-graphene layers

n - Concentration of electrons

p - Concentration of holes

PCE - Power conversion efficiency

PECVD - Plasma Enhanced Chemical Vapour Deposition

P_{in} - Input power

P_{max} - Maximum power

PMMA - poly (methyl methacrylate)

PV - Photovoltaics

PVD - Physical vapour deposition

R_C - Contact resistance

RF - Radio frequency

SiO_2 - Silicon dioxide

SLAR - Single layer anti-reflection coating

T - Temperature

UV - Ultraviolet light

V – Voltage

V_{bi} - Built-in potential

V_{OC} - Open-circuit current density

XPS - X-ray photoelectron spectroscopy

W - Channel width

1. Introduction

1.1 Importance of Solar Cell Technology

Energy that is generated by solar cells is abundant and sustainable. Solar technologies are those that harness solar radiation for thermal and electrical energy that is generated in the home and workplace. Investing in renewable energy resources has become an urgent necessity due to the alarming depletion rate of the major conventional energy resources such as coal, petroleum, and natural gas. In addition, the environmental degradation is caused by harnessing these sources has made investment in renewable energy resources a necessity. These renewable resources will, in the future, provide adequate amounts of power without degrading the environment through the emission of greenhouse gases. Although the sun is an immense source of energy, there are challenges involved in collecting solar electricity. A primary problem is the limited efficiency of the array cells. Most solar cells in the market have an ideal conversion efficiency level that falls between 10 and 20%. Recent developments in solar cell technology have provided significant improvements, although the efficiency of these cells remains about 20%.

Furthermore, methods used in their fabrication require complex machinery and a range of different materials. Since 2010, the technology has benefitted from using graphene, which has proved superior to the silicon previously used in fabrication [1, 2]. As a direct consequence, the present investigation is a continuation of the research into producing graphene/Si Schottky junction solar cells.

1.2 Research Aims and Objectives

The objective of the current study is to find ways to make the preparation of graphene/silicon Schottky junction devices more straightforward by using a top-

window approach. It also seeks to improve the effectiveness of these devices. To fulfil these aims, the following research objectives have been established:

To develop a novel way to create simple top window structure using a sputtering technique.

To study the features of *J-V* curves for prepared devices under various conditions.

To investigate how well-prepared samples hold up when exposed to air.

To study how multigraphene layers improve the fill factor of devices.

To examine the effect of a coated PMMA layer on doped graphene to avoid evaporation of the chemical dopant materials, thus achieving an improvement in the stability of doped devices.

1.3 Structure of Thesis

The major purpose and primary emphasis of this thesis will be to create ways to streamline the manufacture of graphene/silicon Schottky junction solar cells. The dissertation includes six chapters. The following is a presentation of the general framework of the thesis:

Chapter one explains the importance of solar cell technology and how graphene simplifies the process of fabrication of solar cell devices. The outlines of the chapter are also presented.

Chapter Two provides a background history of solar cell technology and its definition from different perspectives. The difficulties and challenges of various types of solar cells are comprehensively discussed, and developments that have increased the efficiency of solar cells are outlined. This chapter likewise provides

an overview of graphene/Si Schottky junctions and discusses the benefits and drawbacks associated with the many shapes these devices may take.

The third chapter describes the devices and materials used in this investigation and describes the experimental methodologies for creating innovative graphene/Si solar cells.

Chapters Four and Five demonstrate the results of prepared samples. In addition, these chapters display the findings obtained from the innovative solar devices under different conditions related to the preparation process and other factors that contribute to the improved efficiency and stability of the devices". The chapters also highlight the detrimental effects of PMMA residue on the properties of transferred graphene sheets and on graphene/n-Si solar cells. To mitigate the presence of PMMA residue and eliminate the s-shape observed in the *J-V* characteristics of samples, innovative techniques utilizing formamide and formamide have been developed. The text highlights the impact of increasing the p doping level in graphene with HNO_3 and utilizing anti-reflection coatings (ARCs) to reduce light reflection off silicon wafers. This process, in turn, enhances the efficiency of solar cells.

Chapter six summarises the work and shows the plan for additional projects that will further improve solar cell efficiency through different studies and develop the usage of graphene within silicon solar cell technologies.

2. Review of solar cell technologies

2.1 Basic Photovoltaic Principle

The fundamental of the photovoltaic is that photovoltaic converts the sunlight to usable energy. Solar cells are fabricated from semiconductors such as silicon and germanium [2]. In this chapter, the fundamental process of photovoltaic process, types and development of solar cell efficiency are explained. The recent improvements in Schottky junction solar cells that are made of graphene and silicon (Si) are also discussed.

2.1.1 Photovoltaic generation

The band structure in semiconductors such as Silicon (Si) contains valence (VB) and conduction (CB) bands. These bands are separated by an energy level called the band gap (E_g). Electrons relax at the valence band unless an electron absorbs sufficient energy from an incident light that contains photons which enables it to be exited to the conduction band by an instantaneous process. Photons that carry energies lower than the band gap will not be absorbed and transmitted into the material. This is because the band gap is greater than the energy of the photon. This means photons that have energy around the band gap will create electron-hole pairs, and electrons will excite the conduction band, leaving holes in the valance band, which will appear once an electron leaves its position, as shown in Figure 2.1. The lifetime of generated electrons in silicon is about 1 msec. It was reported that the diffusion length is within the range of 100-300 μm. Factors of lifetime and diffusion length indicate material quality and suitability for materials used in the preparation of solar cell.

The created holes and electrons by photons are also called excitons when they are involved to each other by the force of Coulomb. However, electrons created

by photons that carry energy much above the band gap will not contribute to the photo-electrical energy as these electrons will lose their energy as heat [3]. In contrast, the energy with a value around the energy gap will contribute to the photo-electrical energy if generated carriers are extracted and collected through contacts [4]. This means that the photogeneration of carriers involves three processes, which are the light absorption process in materials, the separation process of generation carriers and the collection process of carriers [4].

- Absorption process of photons in materials

The solar cell is usually made of materials that absorb the incident light energy ($h\upsilon = E_f - E_i$) if a device is exposed to light. The excitation of electrons will be obtained, and electrons will jump from their original energy level (E_i) to a higher level of energy (E_f). Those carriers are at varied levels of energy placed at the edge of the valence band (E_V) (or above the edge of the conduction band (E_C)). Energy states are not allowed between 2 bands [5]. Where an energy gap (E_g) is between the maximum valence band energy and the minimum conduction band energy. Bands are not flat and are based on their k-vectors, which describe the crystal momentum (p) of semiconductors. Based on the value of momentum, semiconductors can have indirect band gaps such as Silicon and Germanium or direct band gaps such as GaAs and InAs. In the case of a direct band gap semiconductor, electrons motivate from a lower level (valence band) to a higher level (conduction band) with no change in their momentums. This indicates that the two edges have the same value of momentum. In contrast, an electron in indirect band-gap semiconductors will be motivated after changing its crystal momentum. It shows that 2 edges of bands have different momentums [3]. In solar cell technology, direct-gap semiconductors are not preferable compared with indirect-gap semiconductors since the low cost of the preparation process

will be in the case of indirect-gap semiconductors. Besides, there is a process of radiative recombination that reduces solar cell efficiency when direct-gap semiconductors are used [6]. This shows that the generation of carriers is more than the recombination of carriers, referring to the improvement in the operation of devices.

- Separation process of generated carriers

When pairs of electron-hole are created in semiconductors, the separation of those carriers is achieved due to the electric field of the junction. This will not let an electron to get back to its initial level of energy E_i and causing the recombination process with a hole. This indicates that the period of this process must be less than that of the carriers [2].

- Collection process of charge carriers

Due to the electrical field around the junction, the movement of electrons and holes will be toward layers of n-type and p-type, respectively. Carriers will leave the device via contacts. Then, an electron recombines with a hole that was obtained in the valence band. Hence, electron-hole pairs are converted to the electric energy [7].

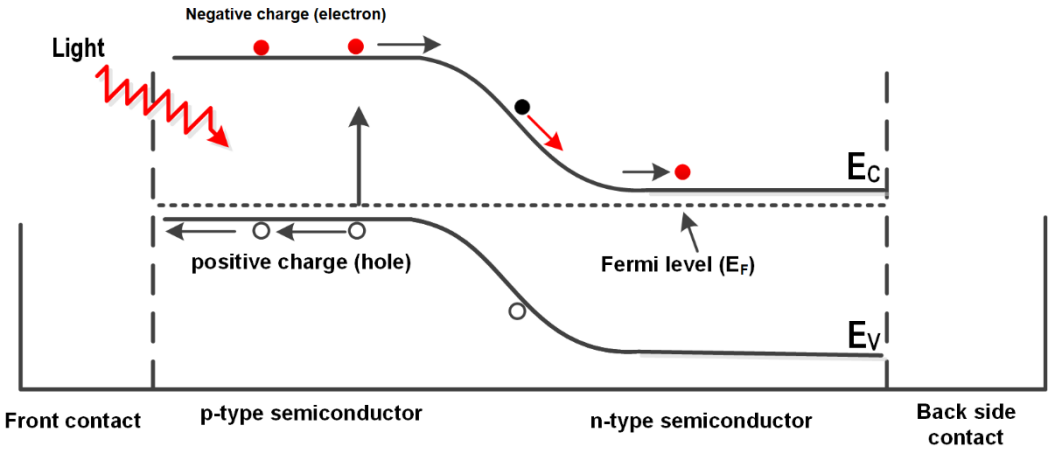

Figure 2- 1 Photo-generation process of carriers in p-n junction silicon solar cells.

2.1.2 P-n junction theory

A p-n junction is required in the photovoltaic device to facilitate the separation of electron-hole pairs, which is the primary goal of the process. The electrical circuit uses to extract the electron-hole generation from the p-n junction made of semiconductors in addition to contacts. There are two types of semiconductors. The first type of semiconductors is known as an n-type, and it has a much higher density of electrons compared to the number of holes. The second type, known as a p-type, has a more significant number of holes than electrons. The p-type and n-type semiconductors are designed by using a doping technique that introduces elements into the fundamental structure of semiconductors. Element from group III or group V can be considered as dopants. To get n-type, the group V elements are involved, whereas for p-type, group III elements are employed. As a result, n-type and p-type become donors and acceptors, respectively. Connecting p-type and n-type semiconductors results in forming a p-n junction. The interface of the junction is called a depletion region. This sort of junction is used in electronic circuitry. At the beginning of forming the junction, electrons

from the n-type will find their way to the p-type, and holes will diffuse from the p-type toward the n-type via the junction, which will start the process of creating the depletion area. The transfer process of carriers will produce an electric field directed from n-type to p-type. The movements of carriers in both sides will reach saturation point [7]. Currently, there is no current flowing through the region because it is isolated, electrically neutral, and in equilibrium. When a p-n junction is exposed to the sunlight, photons will be absorbed by electrons. This increases the number of electron-holes generated. In p-n junctions, the relationship between voltage and current (*J-V*) is presented in Figure 2.2.

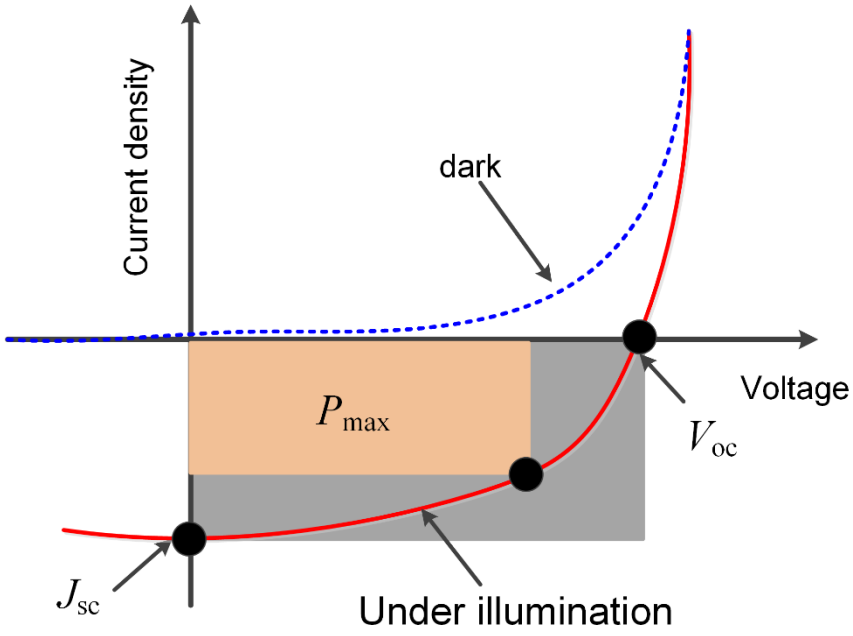

Figure 2- 2 A solar cell's *J-V* features when it is in dark and when it is in subjected to light.

P-n junction characteristics are displayed by the relationship between current and voltage levels under varying environmental circumstances. The junction can be measured in dark and light situations. The setup of dark conditions represents the application of different voltages without sunlight, as shown in the figure. P-n junction solar cells in this situation will experience two directions of external

voltage, forward and reverse biases. In a circuit with a reverse bias, the n-type semiconductor is linked to the positive battery terminal, while the p-type semiconductor is linked to the negative battery terminal. In a forward bias, the n-type semiconductor is coupled to the negative battery terminal, while the p-type semiconductor is connected to the positive battery terminal. As shown in Fig. 2.2, it is possible to demonstrate that the *J-V* graph of a solar cell under light illumination has the same form as the curve when the device operates in a state of darkness, a apart of high density of carriers in the case of an operation under the light condition. Since the direction of the current is counter to the same of that for electrons are flowing, the photocurrent has a negative charge under light condition. When the lighting situation is considered, the photovoltaic factors will be calculated. For instance, the short-circuit current density, known by the abbreviation J_{SC} for its abbreviation, refers to the amount of current that flows through the external circuit when the terminals of the p-n junction solar cells are short-circuited. This current density can be determined by connecting the terminals of solar cells in series with an Ammeter. The value of the J_{SC} varies with the area of devices and mechanisms of loss, both of which are described in more depth in the following sections. The maximum voltage that a p-n junction solar cell can provide to an external circuit when no current flows through the solar cell is referred to as the open circuit voltage, abbreviated as V_{oc}. The fill factor (*FF*) is the ratio of the maximum power density P_{max} produced by p-n junction solar cells to the product of V_{OC} and J_{SC}. This means that the *FF* is an essential photovoltaic component in solar cells. The power conversion efficiency (*PCE*) of a device is the fourth component that can be calculated from the *J-V* relationship, and it is the ratio of the maximum power (P_{max}) obtained from p-n junction solar cells to the incident light power (P_{in}), which is a 100 mW/cm^2.

2.2 Mechanisms of losses

The primary purpose of the solar cells is to convert the light into electrical energy. However, various conditions may cause interference between the incident light and solar cells. Most studies indicate that silicon solar cells have efficiency values ranging from 16% to 24%. This means that a large amount of incident energy is lost [8-10]. The mechanisms of losses in solar cells are categorised as either electronic or optical.

2.2.1 Electronic energy losses

It is well known that electron-hole generation occurs after a photon with a sum amount of energy, which is around the band gap, is absorbed. This pair generation has a certain time in which it can be extracted from the cells before it is recombined. This recombination is the main cause of the loss of electric energy. It affects both the open voltage circuit (*Voc*) and short current circuit (I_{sc}), which consequently affects power conversion efficiency (*PCE*). Several distinct mechanisms exist for recombining electrons and holes including, surface recombination, Shockley-read-hall recombination, auger recombination and radiative recombination [8-10].

- Surface recombination:

The impurities or defects on the surface of silicon elevate the surface recombination. This means that electron-hole recombination is very high on surfaces where the crystal lattice is disrupted. The recombination of surfaces has an important role in the performance of solar cells. The dangling bonds at the silicon surface are the reason for this recombination as presented in Figure 2.3. The bonds are due to the break in the structure of material crystals at surfaces. It was reported that dangling bonds are the source of a high density of defects in

the energy gap of semiconductors. The rate of this recombination (U_S) is obtained by:

$$U_S = \frac{n_s p_s - n_i^2}{\frac{n_s + n_1}{S_{po}} + \frac{p_s + p_{1S}}{S_{no}}} \qquad (2.1)$$

Where p_S and n_S are concentrations of holes and electrons at surfaces. S_{no} and S_{po} represent the velocities of the surface recombination for carriers. The relation was found between the capture of cross-sections (σ_p and σ_n) and velocities of the surface recombination is determined by:

$$S_{po} \equiv \sigma_p v_{th} N_{st} \qquad (2.2)$$

$$S_{no} \equiv \sigma_n v_{th} N_{st} \qquad (2.\ 3)$$

The N_{st} is the density of states at surface per unit area [10]. Both processes, which are the passivation and increase in minority carrier concentration, can reduce the loss of this recombination. In the case of the passivation process, it is achieved by a coated layer of dielectric (such as SiO_2) onto Si substrates. Hence, the density of free-dangling bonds will be less. This also improves the voltage of open circuits and performance of devices [11]. Regarding the enhance in minority carrier concentration is done by the reduction in the concentrations of minority carriers at the surface of Si. This is experimentally obtained by raising the doping of Si surfaces to resist the minority carriers at surfaces [9].

- Shockley-Read-Hall recombination:

The states of defect that are placed at the energy band of enhance increase the recombination process. These states are obtained from impurities in the lattice of semiconductors. Where the energy of an excited electron is lost if that electron is trapped in defect states as displayed in Fig. 2.4. Then, electrons recombine with holes, which are placed at the valence band. The recombination in this case is

obtained when a material with high defects is used in the fabrication process. This recombination

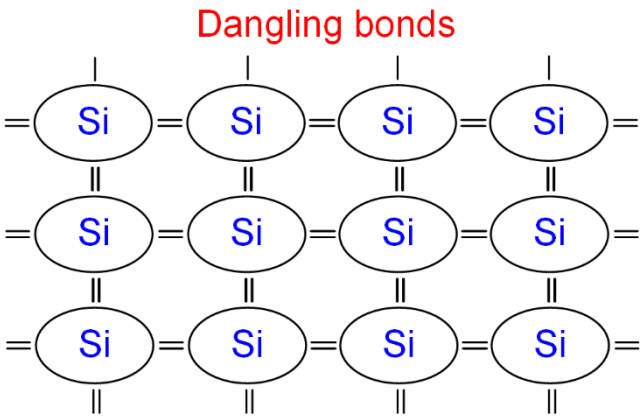

Figure 2- 3 Surface of Silicon and dangling bonds

was found by Shockley, Read and Hall. Hence, it is called SRH recombination. The SRH recombination (U_{SRH}) rate is introduced by the following equation:

$$\boldsymbol{U_{SRH}} = \frac{\boldsymbol{np - n_i^2}}{\boldsymbol{\tau_{po}(n + n_1) + \tau_{no}(p + p_1)}} \qquad (2.4)$$

Where τ_{po} and τ_{no} are lifetimes of carriers (holes and electrons). Lifetimes are linked to density trap (N_t), electrons cross-sections (σ_n) or holes (σ_p) and thermal velocity (v_{th}). These factors are given by:

$$\boldsymbol{\tau_{po}} = \frac{\boldsymbol{1}}{\boldsymbol{\sigma_p v_{th} N_t}} \quad \text{and} \quad \boldsymbol{\tau_{no}} = \frac{\boldsymbol{1}}{\boldsymbol{\sigma_n v_{th} N_t}} \qquad (2.5)$$

The cross-section factors are linked to states of defect possibility of that arrest charges. The concentration of each carrier (electrons (n_1) and holes (p_1)) is introduced by:

$$\boldsymbol{n_1} = \boldsymbol{n_i}\ \boldsymbol{exp}^{\frac{(E_t - E_i)}{KT}} \quad \text{and} \quad \boldsymbol{p_1} = \boldsymbol{n_i}\ \boldsymbol{exp}^{\frac{(E_i - E_t)}{KT}} \qquad (2.6)$$

Where E_i and n_i are the intrinsic level of energy and the intrinsic concentration of carrier, T is the temperature and k is the Boltzmann constant. Subsequently, the lifetime of SRH is calculated by:

$$\boldsymbol{\tau_{SRH}} = \frac{\boldsymbol{\tau_{po}(n+ n_1) + \tau_{no}\,(p+p_1)}}{\boldsymbol{n_o+p_o+\Delta n}} \qquad (2.7)$$

Under injection levels (low and high), the lifetimes of SRH recombination will be as shown:

n-type Si $\quad \boldsymbol{\tau_{SRH,LLI} = \tau_{po} + \frac{\tau_{no}(\Delta n+p_1)}{N_D}}$ and $\boldsymbol{\tau_{SRH,HLI} = \tau_{no} + \tau_{po}}$ (2.8)

p-type Si $\quad \tau_{SRH,LLI} = \tau_{no} + \frac{\tau_{po}(\Delta n+n_1)}{N_A}$ and $\tau_{SRH,HLI} = \tau_{no} + \tau_{po}$ (2.9)

If defect states are at the middle of the energy gap, both p_1 and n_1 are equal to n_i. So, the lifetime of SRH is extracted as:

n-type Si $\quad \tau_{SRH,LLI} = \tau_{po}$ for mid–gap traps (2.10)

p-type Si $\quad \tau_{SRH,LLI} = \tau_{no}$ for mid – gap traps (2.11)

This shows that the value of the lifetime of SRH is small in the case of traps in the middle of an energy gap [6, 12]. This also presents that high-quality semiconductors should be utilized in the preparation process of Si devices.

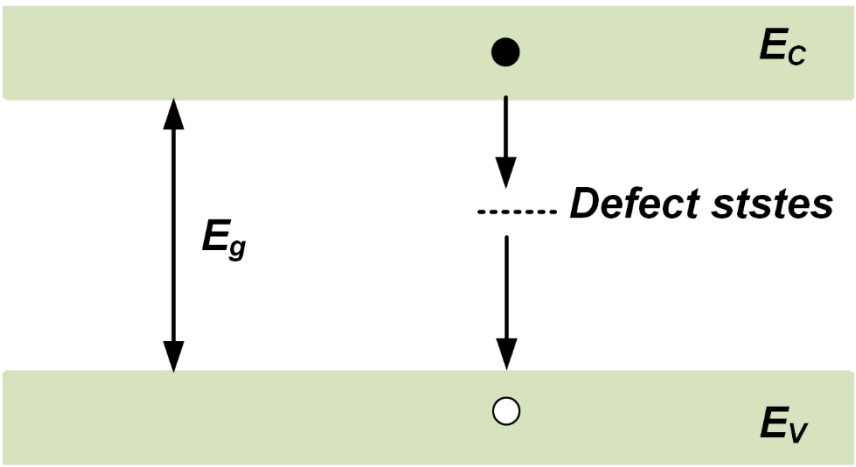

Figure 2- 4 Process of Shockley-Read-Hall recombination.

- Auger recombination:

This type of recombination obtains due to the interaction of 3 particles that are two holes with an electron or two electrons with a hole as presented in Fig. 2.5. During the Augur recombination, an electron placed at the conduction band recombines with a hole at the valence band energy. Subsequently, another particle, such as an electron or hole, absorbs the released energy and becomes excited to a higher energy level. The rate of Auger recombination (U_{Auger}) consists of 2 processes which are (U_{eeh} and U_{hhe}), and it is presented by:

$$U_{Auger} = U_{eeh} + U_{ehh} \quad or \quad U_{Auger} = C_n n^2 p + C_p n p^2 \qquad (2.12)$$

Where C_p and C_n are factors for Auger coefficients of holes and electrons [13]. Lifetimes of the recombination if low and high levels of injection are used. They are determined by:

For p-type silicon

$$\tau_{Auger,LLI} = \frac{1}{C_n N_D^2} \quad \text{and} \quad \tau_{Auger,HLI} = \frac{1}{(C_n + C_p)\Delta p^2} \qquad (2.13)$$

For n-type silicon

$$\tau_{Auger,light} = \frac{1}{C_p N_A^2} \quad \text{and} \quad \tau_{Auger,high} = \frac{1}{(C_n + C_p)\Delta n^2} \qquad (2.14)$$

Based on the above equations, for heavy-doped Si, the Auger recombination is greater than the radiative recombination. Besides, the lifetime of Augur is inversely related to the carrier density squared. In contrast, the lifetime of radiative linearly reduces with a concentration of dopants. This shows that the recombination of Auger is the major factor at emitters and the back surface of devices [14, 15]. It has also

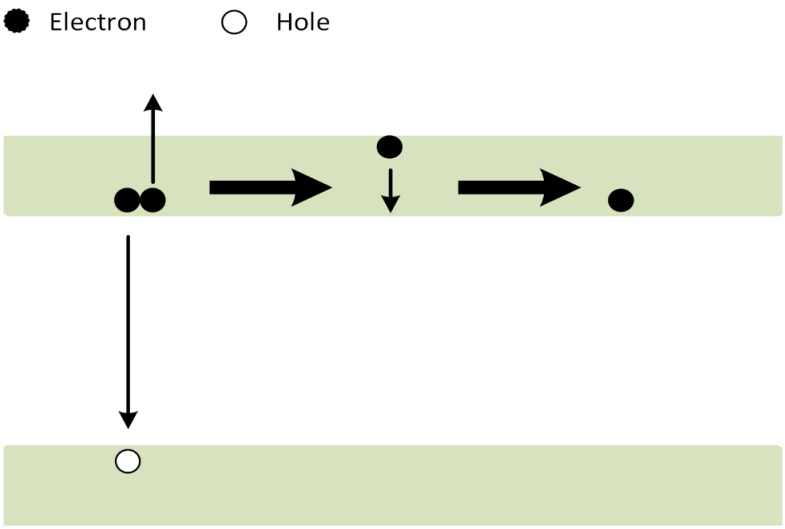

Figure 2- 5 Auger recombination process.

been reported that the recombination of Auger is 3 times greater than in p-type Si when heavy-doped n-type Si is used. This is because C_n and C_p are 2.8×10^{-31} and 9.9×10^{-32} cm^6/s for the Si that has a dopant concentration of about 5×10^{18} cm^{-3}. This leads to devices made of p-type Si substrates are more precious by this recombination [13].

- Radiative (band-to-band) recombination:

Radiative recombination or band-to-band recombination happens if an electron directly comes back from the band of conduction into the band of valence. This electron recombines with a hole. Due to the difference between states, photon releases as presented in Fig. 2.5. This recombination (U_{rad}) rate is presented by formela numbered 2.7. This is proportionally dependent on concentrations of electrons in the case of an n-type semiconductor and holes in the case of another type of semiconductor.

$$U_{rad} = Bnp \qquad (2.15)$$

The factor of *B* refers to the radiative coefficient, *p* and *n* are concentrations of holes and electrons for p and n types of semiconductors. The radiative recombination lifetime (τ_{BB}) is obtained by:

$$\tau_{BB} = \frac{\Delta n}{B \cdot (n_o + \Delta n) \cdot (p_o + \Delta n)} \qquad (2.16)$$

The parameter of Δn refers to the differential electron concentration, p_o and n_o are the thermal equilibrium concentrations of free carriers. Accordingly, the lifetimes of radiative recombination when a low injection (*LLI*) and high injection (*HLI*)) levels are used as below:

$$\tau_{BB,LLI} = \frac{1}{B \cdot N_{doped}} \quad \text{and} \quad \tau_{BB,HLI} = \frac{1}{B \cdot \Delta n} \qquad (2.17)$$

Where N_{doped} is the acceptor and donor concentration for p or n-type of semiconductors. For low levels of the injection, the lifetime of radiative recombination is constant. Whereas, for medium and high injection levels, it drops. Hence, the usage of indirect band gap semiconductors results in low radiative recombination compared with that of direct band gap semiconductors since electrons in indirect bands need phonons to conserve their momentum to be dropped to the valence band [16].

2.2.2 Optical energy losses

Optical loss is another form of loss that solar cells suffer. This loss degrades photovoltaic performance, particularly the short-circuit current. Reflection of the front silicon wafer, parasitic absorption, parasitic free carrier absorption and reflection of the back silicon wafers are examples of optical loss in Si solar cells [17].

- Reflection of the front silicon surface

About 30% of the loss of light from Si solar cells is due to the reflection of the silicon substrate. In this situation, the optical loss arises from the reflection of metals and silicon wafers. The reflection of metal decreases the process of photogeneration in the wavelength range of 500-1000 nm. The reflection of the Si substrate comes from the reality of the high reflection index (n>3.5) of substrates. It has been reported that the reflection at the surface is about 40% in the wavelength range of 300nm-1000 nm related to air (n=1) as observed in Fig. 2.6 [18]. This is decreased by antireflection coatings. To achieve the coatings, a single layer (SLAR) such as SiO_2 and double layers (DLAR) such as SiO_2/TiO_2 are created onto wafers. The thickness of SiO_2 layers for SLAR is equal to one-quarter of the wavelength of the incident light wave ($d_{SiO2} = \lambda_o/4n_{SiO2}$, where λ_o is the mid-range of the wavelength of 500 nm, n_{SiO2} and d_{SiO2} refer to the refractive index and

$$\frac{n_1 d_1}{\lambda_0} = \frac{1}{2\pi}\tan^{-1}\left\{\pm\left[\frac{\left(n_s - n_0\right)\left(n_0 n_s - n_2^2\right)n_1^2}{\left(n_1^2 n_s - n_0 n_2^2\right)\left(n_1^2 - n_0 n_s\right)}\right]^{1/2}\right\} \qquad (2.18)$$

$$\frac{n_2 d_2}{\lambda_0} = \frac{1}{2\pi}\tan^{-1}\left\{\pm\left[\frac{\left(n_s - n_0\right)\left(n_0 n_s - n_1^2\right)n_2^2}{\left(n_1^2 n_s - n_0 n_2^2\right)\left(n_2^2 - n_0 n_s\right)}\right]^{1/2}\right\} \qquad (2.19)$$

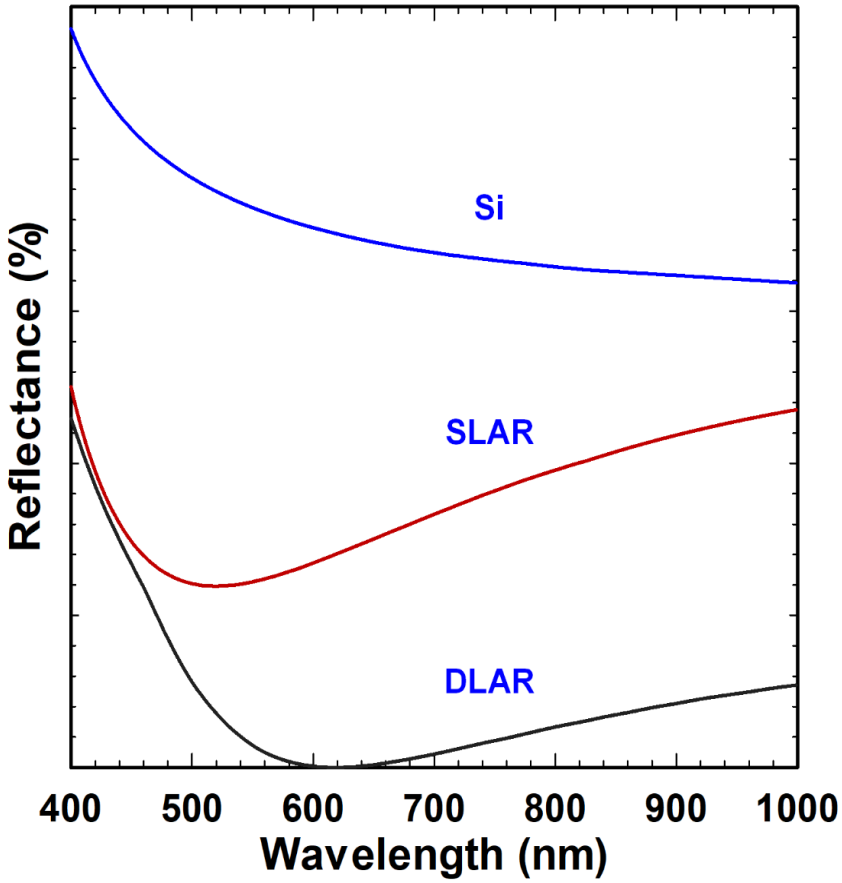

Figure 2- 6 Comparison of reflectance spectra achieved by anti-reflective coating versus uncoated Si wafers' reflectance, referring to SLAR as a mono-layer anti-reflection and DLAR as a double-layer anti-reflection.

thickness of SiO_2 layer) [19]. It was found that the reflectance could be zero when DLAR coatings are used. The thicknesses of SiO_2 and SiO_2/TiO_2 layers should meet the calculations 2,18 and 2.19 [18]. Where d_2 and d_1 are the width of the SiO_2 and TiO_2 layers, respectively. Factors of n_0, n_1, n_2 and n_s present the refractive index of air, TiO_2, SiO_2 and the substrate of Si, respectively. A texturing procedure similarly used to decrease the reflectance from substrates of silicon to below 15% [20-22]. In this case, more light could be absorbed by substrates owing to various interfaces as indicated in Fig. 2.7 [17].

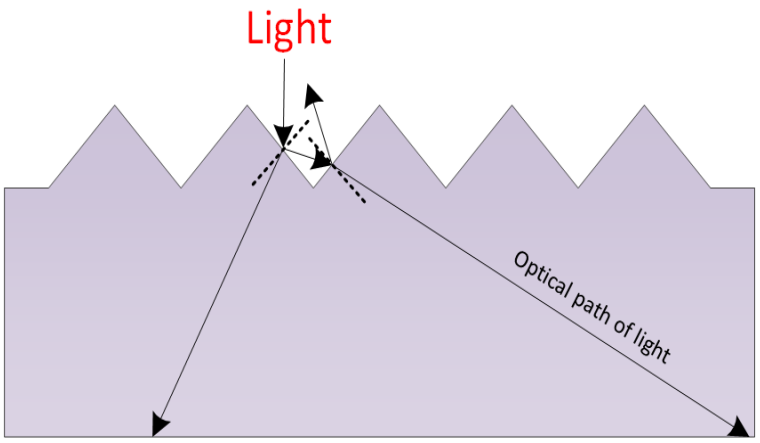

Figure 2- 7 Diagram illustrating the light paths on a textured Si.

- Anti-reflection coatings for parasitic absorption

This factor is due to the absorption of some anti-reflection coatings. It was mentioned by the Beer-Lambert law that the absorption of light via materials is presented by:

$$I_{(X)} = I_o\, e^{-\alpha.x} \qquad (2.20)$$

In this equation, I_o refers to the intensity of the light, *I(x)* presents the intensity of light that is absorbed by the material at depth (x) and α is the coefficient of absorption that is a function of the extinction coefficient (k) for the material and wavelength (λ). The absorption coefficient is taken as [23] :

$$\alpha = \frac{4\pi K}{\lambda} \qquad (2.21)$$

The ARC is made of materials that absorb a apart of the light, which is placed in a wavelength range of 300-500 nm [24], leading to the optical loss. This recommends that layers of antireflections should be selected to have negligible absorption for that range. It was recommended that the usage of SiO_2 and SiN_X are the best-coated layers in Si solar cells to decrease his loss [23].

- Parasitic absorption of free carriers

Free carrier absorption (FCA) is a phenomenon observed in semiconductors where electrons (or holes) in the conduction (or valence) band are excited to higher (or lower) energy levels within the same band. However, these carriers do not contribute to the output current of devices as their energy is dissipated as heat. This matter is neglected in silicon substrates if the wavelength of the light is less than 1000 nm. This also means that it becomes a significant issue if the wavelength of the light is higher than 1000 nm [25].

- Reflection of the back silicon wafers

This loss is due to the small thickness of Si substrates. This results in the weak absorption of wavelengths that are less than 1 μm. Where the wavelength range of incident light is placed between 850 and 1200 nm, and this range holds about 25% of the optical energy of the spectrum of AM 1.5 as displayed in Figure. 2.11. It can be observed that the thickness of Si wafer should efficiently absorb the light of 1100 nm since it has a 1.12 eV band gap. To also solve this issue, a half thickness of wafers is employed after coating the backside of it with metals that have high reflection. This is why Silver or Aluminium are applied as rear contacts. As a result of this process, the absorption of light will be enhanced (see Fig. 2.8) [17]. This issue has been solved by the specific back surface reflector (BSR) known as a Lambertian back reflector as shown in Fig. 2.9.

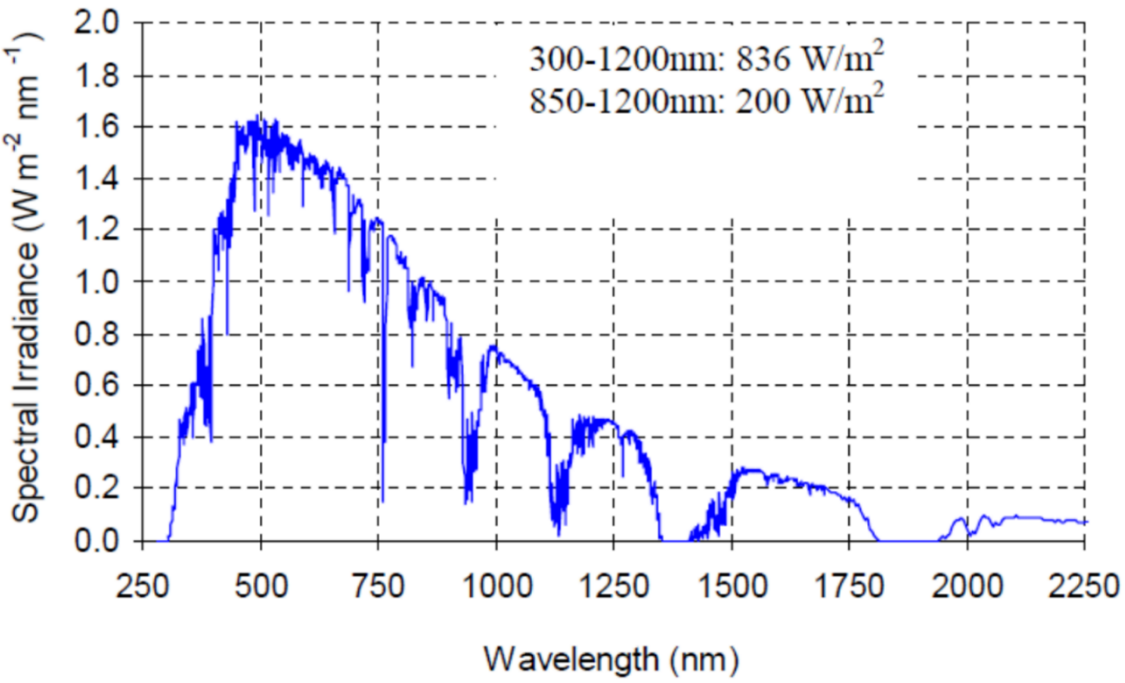

Figure 2- 8 Spectrum of AM 1.5G [26].

This BSR randomizes the direction of the light inside substrates. This means the light reaching the back side of wafers will reflect several times inside substrates. Besides, the light will reflect at the surface of substrates if the light angle at the top surface is higher than the critical angle (θ_c) [27, 28]. The information above suggests that the path length of light is amplified by a factor of $4n^2$, where n is the refractive index of silicon substrates [29]. There is another benefit of using the BSR which is the reduction of the preparation cost of devices since a thin silicon substrate can be used to achieve the full absorption of the light, compared with that achieved with thick silicon substrates.

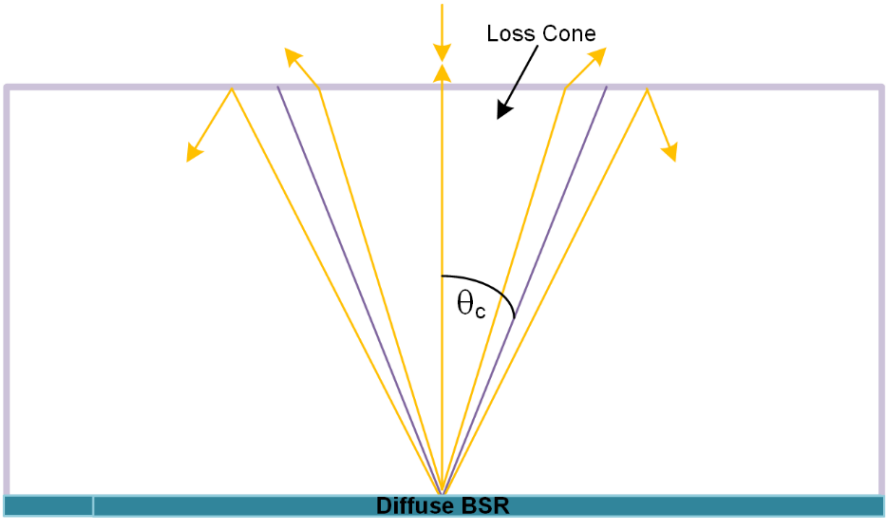

Figure 2- 9 A diagram of Lambertian back reflector.

2.3 Types of Solar cells

The photovoltaic effect is the primary mechanism by which solar cells accomplish their goal of converting the sun's radiant energy into direct current (DC). Solar cells are made from various materials, including silicon, compounds based on silicon, and other materials [30-32]. Copper indium selenide, cadmium telluride (CdTe), copper indium and gallium selenide (CIGS) are some of the components that are used in the construction process of solar cell devices in the commercial sector. Other types of solar cells are still in development. These types are quantum wells, perovskites, organic solar cells and quantum dots [33]. The growth of solar cell technologies has been reported and recorded in terms of the value of *PCE*. It has also been shown that perovskite solar cells provide poor stability compared with other types. Figure 2.10 depicts the power conversion efficacy of various solar cells over the past four decades. As shown, silicon solar cells provide the highest efficiency with great stability compared with those of other types.

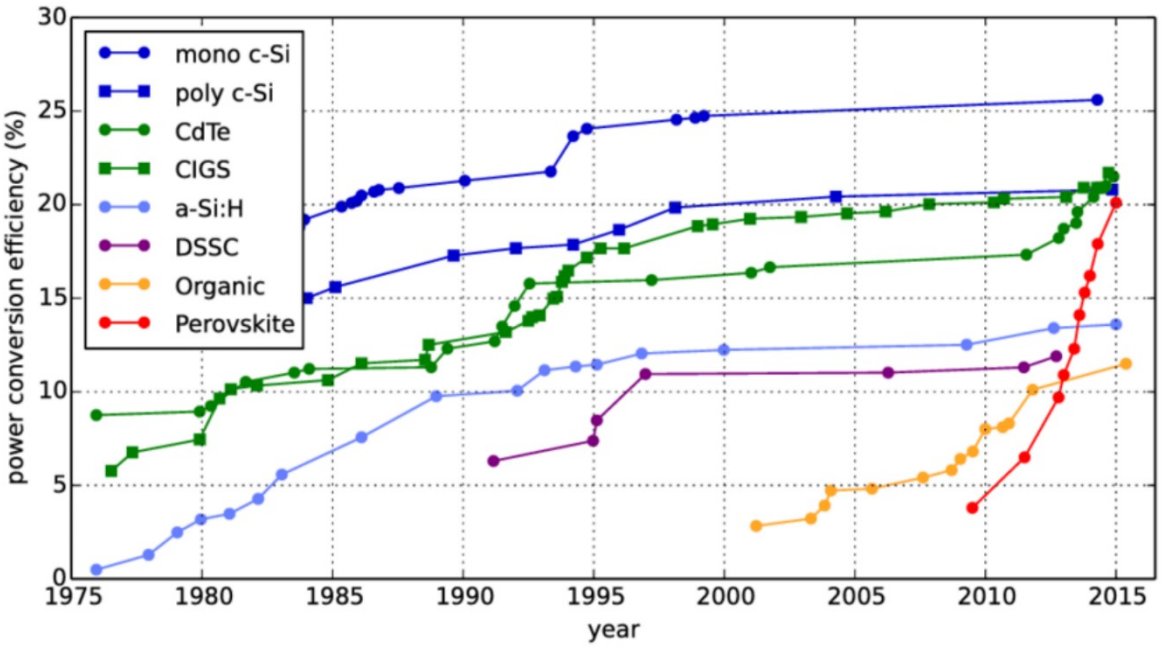

Figure 2- 10 Growth of the power conversion efficiency of solar cells [34].

2.3.1 Solar cells based on p-n junction Silicon solar Cells

As mentioned, Si solar cells convert the light into electricity. Where pairs of electron-hole are generated. Then, they are separated by the electric field junction and followed by movements of electrons and holes in the opposite direction toward electrodes, leading to the photocurrent [35, 36].

2.3.1.1 Single crystalline Si solar cells

Because of the indirect band gap energy of crystalline silicon, it has been used in the preparation of devices. The usage of this silicon leads to lower optical absorption coefficient ($\alpha \approx 100$ cm^{-1}). Silicon wafers with thickness about a hundred microns should be used to enable devices to absorb the most incident light. To achieve the generated photocurrent, pairs of electron-hole should reach the electric field at the depletion region of solar cells. This can be obtained by the diffusion process of carriers to the region of the junction, and the length of diffused minority carriers that move before the recombination process is given by L. In

solar cell technology, a long diffusion length is required as pairs of carriers are generated in the whole of substrates, which is based on the wavelength range of the light. Where the number of carriers that attain the junction is high if they have long diffusion lengths. Under this condition, solar cells will have high performance. Elementary semiconductor theory defines a diffusion length (L) as follows:

$$L \alpha \sqrt{T\mu} \qquad (2.15)$$

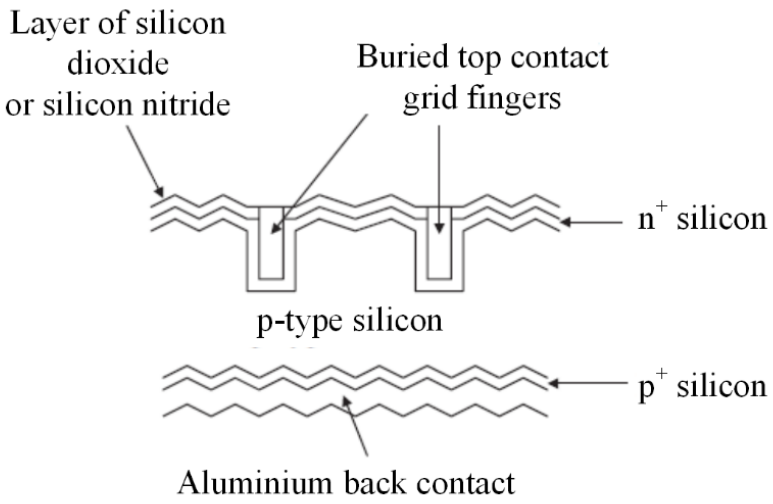

Figure 2- 11 Screen-printed contacts for a Si solar cell [40].

The μ is the mobility and T is the minority carrier-lifetime in the absorbed light [37]. Since μ and T depend on the quality of materials, devices should be fabricated by using high-quality materials such as crystalline silicon, leading to high solar cell performance. Fig. 2.11 shows a view of the cross-section for the conventional Si solar cell [38]. The monocrystalline silicon wafer has been doped by boron to achieve the p-type Si substrate. To obtain the p-n junction, impurities of phosphor were diffused. Then, silver fingers of contacts were applied by a screen-printed method. As shown, these fingers are placed onto the n-type area

rather than metals. This lets light reach the region of the junction, minimizing the optical losses. To reduce the optical loss that comes from the reflectance of substrates, the surface was textured. This develops the length of the light path in the whole substrate. Besides, the layer of titanium dioxide antireflection coating was coated onto the top of the contact fingers. This procedure further decreases the reflection of Si wafers. The recorded efficiency of this solar cell is around 13% [39].

2.3.1.2 Polycrystalline Si

Polycrystalline silicon is utilized in the device fabrication process to establish a junction, aiming to achieve a reduced overall cost compared to prior solar cell technologies, as depicted in Fig. 2.12. The Plasma Enhanced Chemical Vapour Deposition (PECVD) method ensures the deposition of a high-quality polycrystalline silicon layer on substrates. In the PECVD process, hydrogen gas is a pivotal factor. This will also achieve the passivating process

Figure 2- 12 Optical image of a polycrystalline Si solar cell with screen-printed contacts [40].

of the dangling bonds and reduce the boundaries of the grain. There are other advantages of polycrystalline Si such as low sensitivity for the quality of materials,

which create a module of devices. An antireflection coating layer of Si nitride was also coated by PECVD onto devices to reduce the optical loss. The efficiency of this type of device is about 12.6%, which is about the same value as that was recorded by single crystalline silicon cells [38].

2.3.1.3 Amorphous Si (a-Si:H)

The process involves depositing a hydrogenated amorphous silicon (a-Si: H) film onto a silicon wafer to establish the junction of solar cells, as depicted in Figure 2.13. Hydrogen gas is also an important factor in the pa The process involves depositing a hydrogenated amorphous silicon (a-Si: H) film onto a silicon wafer to establish the junction of solar cells, as depicted in Fig. 2.13.ssivating of unwanted bonds located onto substrates. It has been documented that hydrogenated amorphous silicon possesses a direct energy band gap of 1.7 eV and exhibits a noteworthy absorption coefficient conducive to photogeneration. These characteristics necessitate only a few microns of the material to absorb most incident light. Moreover, this approach contributes to cost reduction in the fabrication process. The efficiency of prepared solar cells was 12%. However, there is an issue with the achievement of the doping procedure in hydrogenated amorphous Si since this doping results in the reduction of the mobility and lifetime of minority carriers. The current was solved by the introduction of the intrinsic (i) Si that was formed between the p and parts. The structure of solar cells in this case known as a p-i-n. Fig. 2.13 presents the cross-section of a typical p-i-n structure of devices. The recorded efficiency of the initial solar cell made is about 12%. However, the value of this efficiency degrades to 5% with time, especially after exposing devices to the light for few months [41].

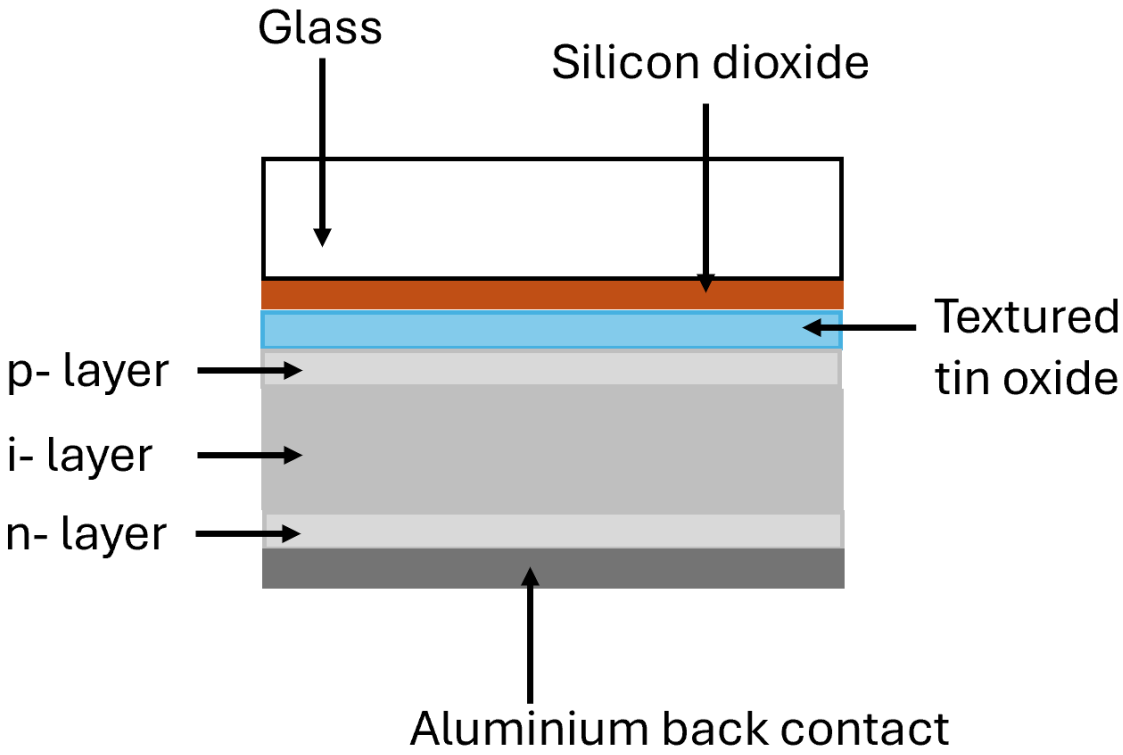

Figure 2- 13 an amorphous silicon solar cell viewed in cross-sectional

2.3.1.4 Heterojunction intrinsic thin-layer solar cell

Solar cells employing heterojunction intrinsic thin-layer (HIT) technology are structured with either p-i-n single or p-i-n multiple configurations. These cells feature thin layers of intrinsic amorphous silicon deposited on both sides of crystalline silicon substrates, as illustrated in Fig. 2.14. Following this, n-type and p-type silicon layers are deposited onto the intrinsic layers. This structure has shown several advantages in the solar cell technology. For example, the absorbing process of the light is competent since energy gaps of the substrate, n and p-type Si films are different. This results in an advancement in the efficiency of solar cells to be about 21%. This is obtained after the unwanted bonds on Si wafers are eased by the

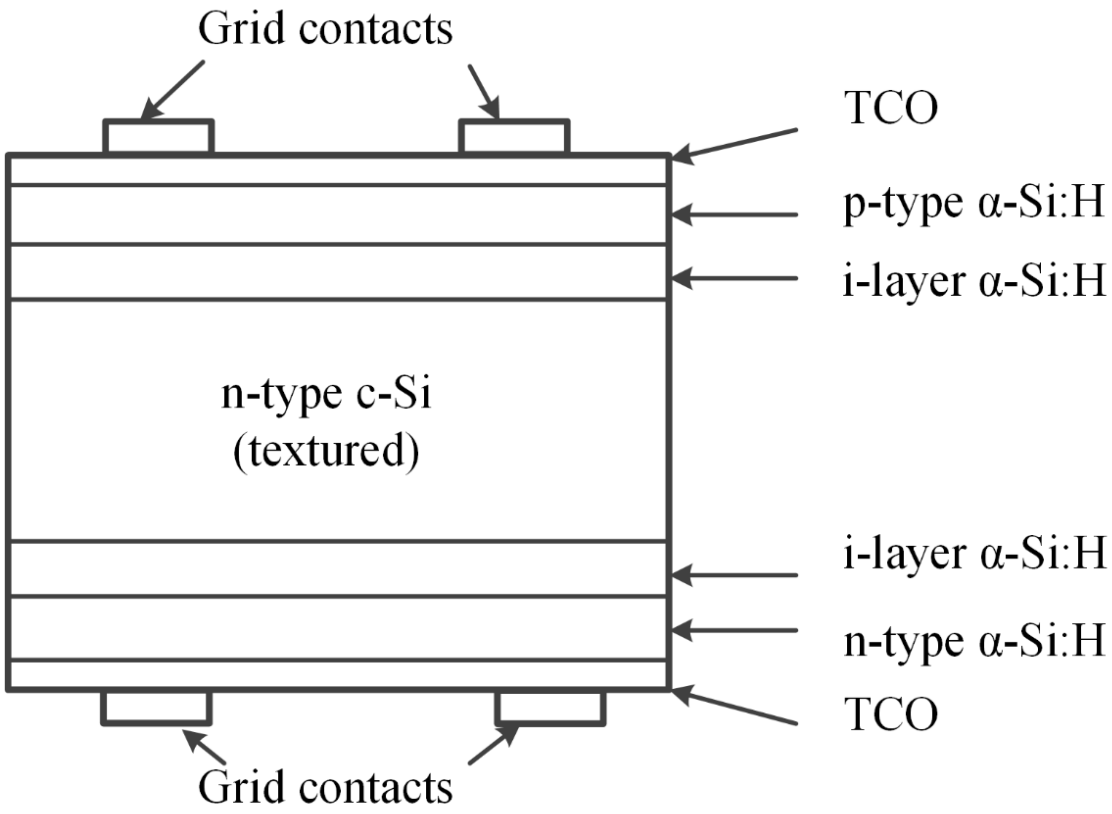

Figure 2- 14 Cross-section of the HIT solar cells. The thickness of the substrate was 200 □m, with thicknesses of 10 nm intrinsic + p-type amorphous and 20 nm intrinsic + n-type amorphous silicon [42].

layers of intrinsic amorphous silicon. This leads to obtaining the high value of higher open circuit voltage. Based on this discussion, this type of solar cell is more efficient compared with the values of the previous devices discussed in previous sessions. In addition, it is more stable at high-temperature conditions [43]. This shows that there are many advantages. Nevertheless, there are some issues with devices. There is loss owing to the absorption of metal films, and this has happened in the wavelength range between 500 nm and 1000 nm. Besides, there is a loss because the absorption of ITO film obtains in the wavelength range between 300 nm and 500 nm. There are defects in the lattice structure of the intrinsic Si if the temperature for forming layers

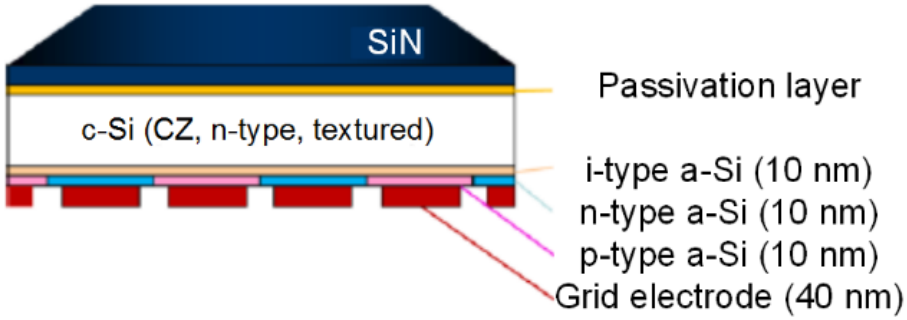

Figure 2- 15 Cross-section of the back-contact structure of HIT solar cell [24].

is higher than 200 °C. The fabrication process will be costly as devices require more layers compared with those discussed previously [44]. The issue of optical loss due to electrodes in HIT solar cells was solved by the back contact structure as displayed in Fig. 2.15. As observed, layers of coated films and metals are created on the backside of Silicon wafers. This enhanced the *PCE* of devices to higher than 25% [24].

2.3.2 Solar cells based on non-silicon materials

2.3.2.1 Cadmium sulfide/Cadmium telluride

Cadmium sulfide (CdS)/Cadmium telluride (CdTe) are materials with an ideal bandgap, and support to low-cost and a range of fabrication methods. Devices shown in Fig.2.16 are made by using various methods, including CVD, sputtering, screen printing and thermal evaporation. In addition, the energy gap can be regarded as having the best bandgap for converting light into electrical energy [45]. The most significant degree of efficiency is more than 10%. The features of CdTe described

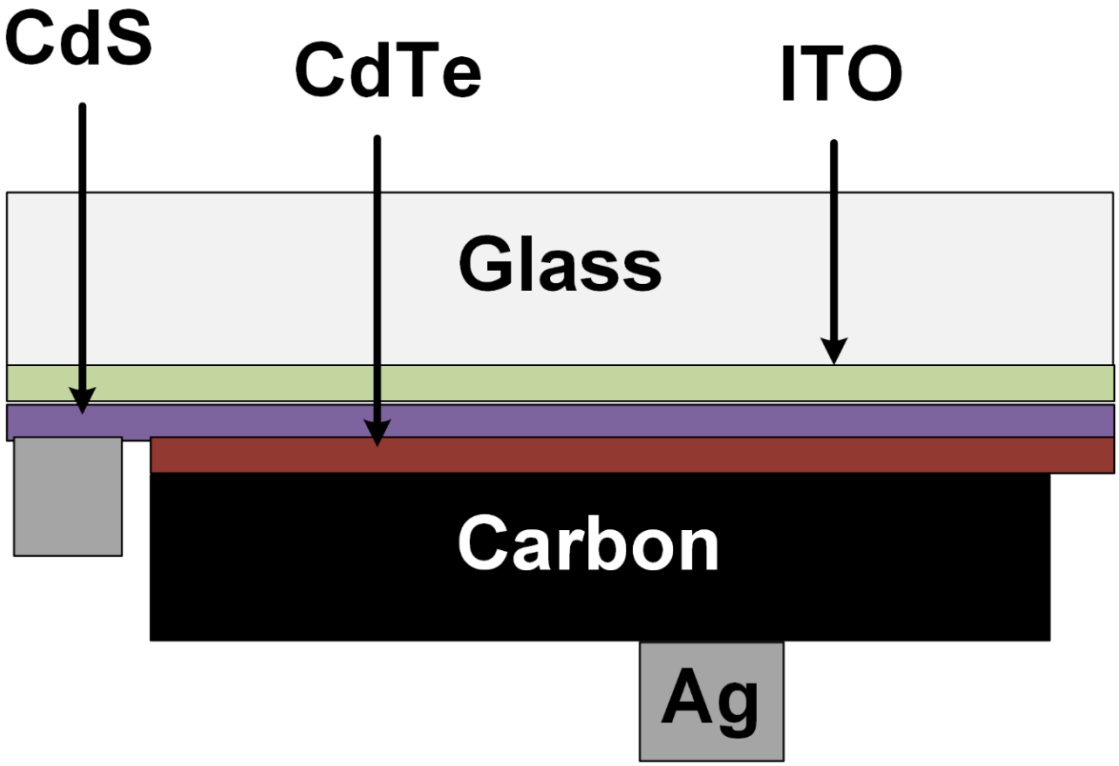

Figure 2- 16 Diagram of the CdS/CdTe solar cell.

above mean that it is a suitable material to produce solar cells. Despite its advantages, it has been found that the performance of CdS/CdTe solar cells can vary, even when two cells are identically fabricated [46]. The varying performance of these devices has not yet been explained. However, it could be due to the quality of CdTe materials, humidity, or poor contact conditions. Moreover, the toxicity of Cd and its effect on the surrounding environment could be matters of concern. In addition, the production of Te is deficient, which means it is a rare material. Therefore, this type is unsuitable for the mass manufacture of solar cells [46-48].

2.3.2.2 Solar cells made of copper indium gallium selenide

Copper indium gallium selenide (CIS) has a high optical coefficient of absorption owing to its bandgap of 1 eV. The indium has been replaced by an indium-gallium alloy, causing the bandgap of CIGS to reach 1.68 eV. Controlling the Ga/(In+Ga) ratio further improves the performance. A device of the solar-type consists of 6 films (see Fig. 2.17), from upper to lower sides, which is a transparent contact of doped zinc oxide (ZnO:Al), intrinsic zinc oxide (i-ZnO) as a high resistive layer, n-type cadmium sulfide (CdS), p-type CIGS as absorbing layer, a back contact of the metallic molybdenum (Mo) and a glass substrate [49]. The absorbed layer is made of a direct band gap p-type polycrystalline semiconductor with a high coefficient of absorption. Processes of absorption and generation for light and carriers, respectively, are achieved in this layer. The energy gap of this layer relays on compositions of the gallium and indium. It was reported that the E_g can be varied from 1.04 to 1.67 eV [50]. Wagner prepared the first CIGS device with a *PCE* of 12%. Repins from the National Renewable Energy

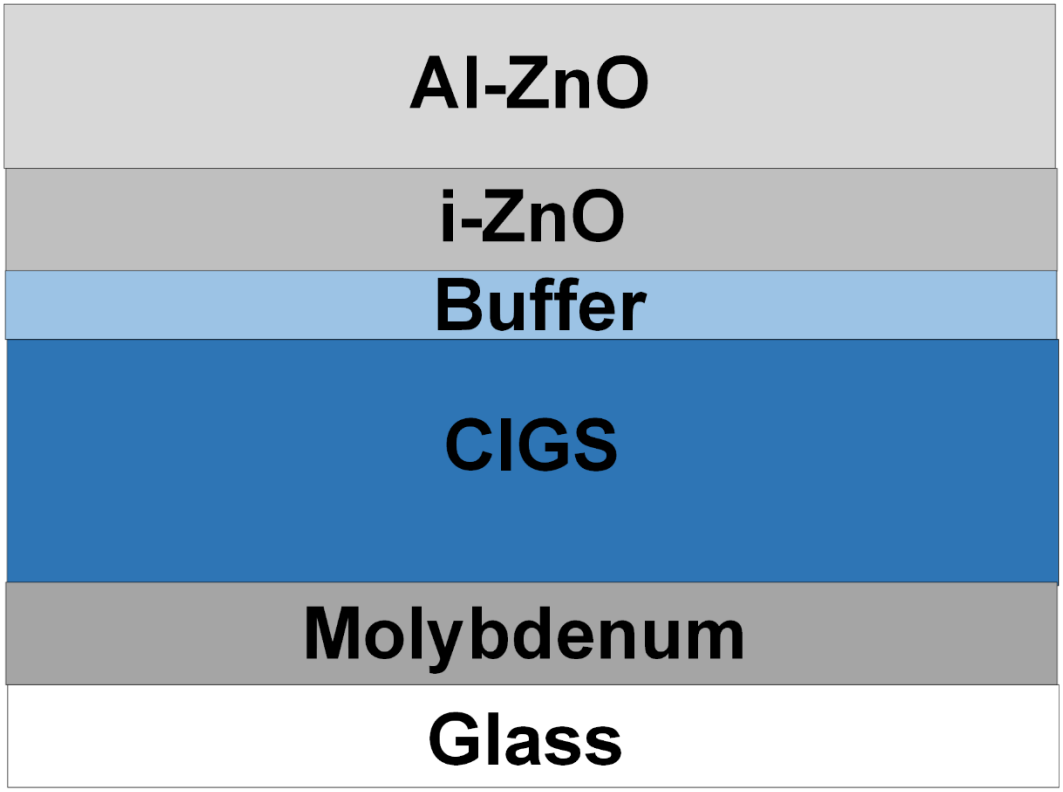

Figure 2- 17 Diagram of a CIGS solar cell.

Lab (NREL) reported 19.9% conversion efficiency in their publication [51]. A more recent improvement in this technology has been introduced to provide an efficiency of 20.5%. This was achieved by Solibro [52]. The drawback for both CIS and CIGS is the limited source of Indium. Likewise, it is difficult to fabricate the absorber layer of CIS, and the production process for CIS and CIGS is complex. These difficulties make the mass fabrication of devices unachievable likened with that of p-n Si devices [53-56].

2.3.2.3 Thin film solar cells

In the industry application during the last four decades, a thin film has been used as another way to prepare crystalline Si solar cells, competing with conventional energy sources. The thickness of prepared thin film ranges from nanometres and

micrometres [57]. In 1975, the first coated silicon with hydrogenated amorphous composites (a-Si:H) was reported by Spear and LeComber [58], followed by Carlson and Wronski in 1976 [59], who demonstrated the principle of p-i-n structures, where, the factor of i refers to intrinsic Si. Then, during the 1990s, nanocrystalline silicon (nc-Si:H) started to be used as another light absorption material, and it has 1.1 eV bandgap [60]. Therefore, it improves absorption due to emerging bandgaps of thin films made of Si support to integrate double, tipple and quadruple solar cell junctions [61, 62]. It was found that devices based on this have several characteristics. For example, it could be manufactured on a glass or stainless steel substrate, eliminating the need for silicon wafers [63, 64]. To trap the light inside the cells, transparent conductive oxides (TCOs) are applied to the front contact. Highly efficient reflective materials, such as silver, are used on the back contact, along with (TCOs), leading to important enhancement in the performance of devices. However, the efficiency of samples was smaller than that *PCEs* of p-n Si devices [65].

2.3.2.4 Hybrid solar cells

Hybrid solar cells are formed from organic and inorganic materials. The usage of both materials produces the exclusive possessions of inorganic semiconductor and materials of organic/polymeric [66]. Besides, it results in the low-cost of preparation of solar cells [67, 68]. In addition, inorganic semiconductors based on nanoparticles have high absorption of coefficient and particle size-persuaded tunability of the bandgap. Therefore, the usage of organic/inorganic in hybrid solar cells have been shown noteworthy for researchers in recent years. Solar cells in this concept are prepared in several ways such as solid-state dye-sensitized devices [69-71] and the bulk heterojunction including varied

nanoparticles such as TiOx [11], ZnO [72], CdSe [73, 74], CdS [75], PbS [76], and CuInS2 [77, 78]. Materials such as inorganic or organic dyes and TiO2 electrodes [78, 79] are employed to prepare dye-sensitized devices. When photons are absorbed, electrons are excited in the sensitizer molecule and are jumped to the TiO_2 the higher band. Then, it spreads over the TiOx porous to the metal. The oxidized molecule moved back to the initial state by electrons in the liquid electrolyte redox couple within the pores as shown in Fig. 2.18 [80, 81]. This process is obtained from the garnering light by molecular absorbers that are formed onto the wide surface of semiconductor [79]. When a dye monolayer is used, an apart of incident light is harvested. This is why it is better to increase the interface area between the dye and semiconductor oxide.

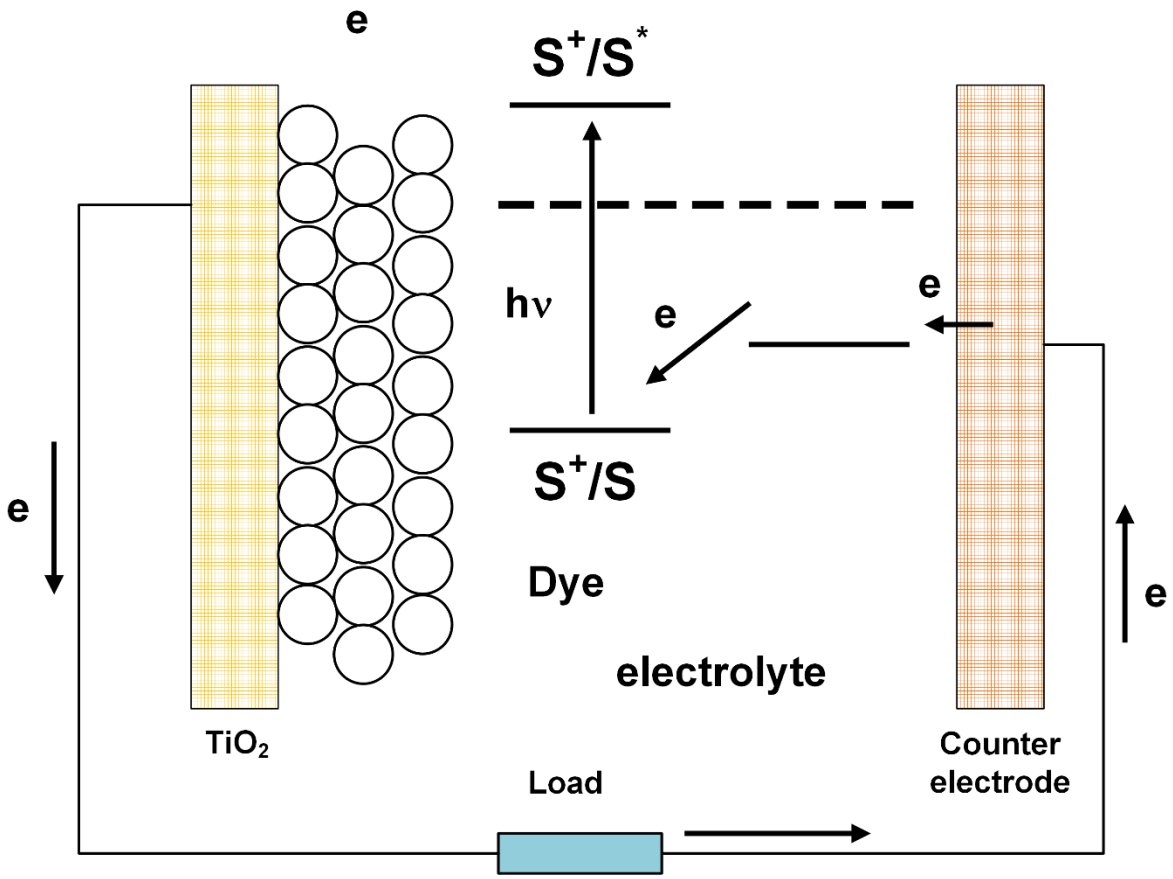

Figure 2- 18 Principle working of a dye-sensitized solar cell.

To achieve this, electrodes based on nanoparticles are employed to improve the interface. Electrodes of large band-gap semiconductors through dye sensitization are attained by coating surfaces of porous TiO_2 with special dye molecules that efficiently absorb the arriving photons [82]. This development is shown in Fig. 2.19. As presented, the incoming photon is shifted to current efficiency with higher wavelengths when the dye is layered. It has been reported that the recorded efficiency can be up to 11%. Nevertheless, this value is less than that obtained from devices based on Si [83]. Additionally, the manufacturing process of devices is complicated compared with that of Si solar cells.

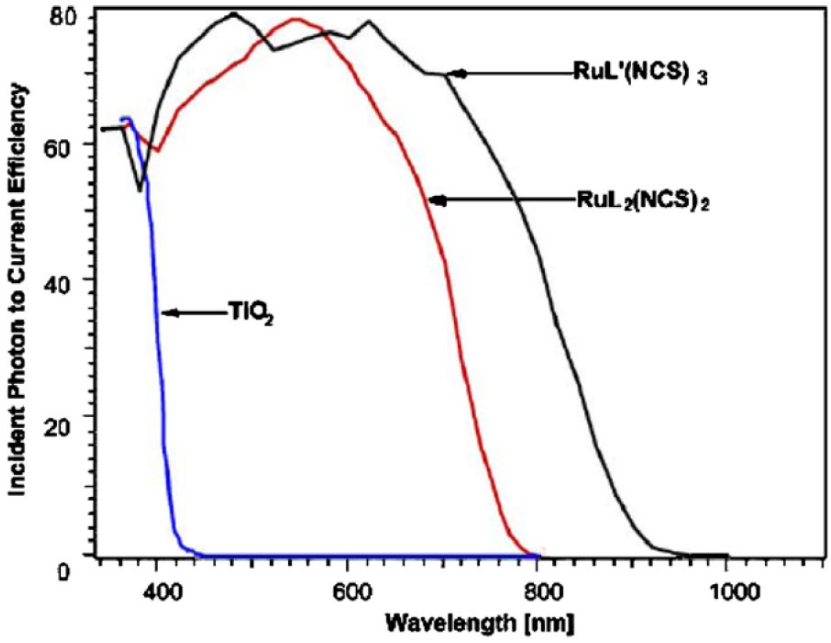

Figure 2- 19 The effect of Sensitization on the relation between efficiency wavelengths [83].

2.3.2.5 II-V compound Solar cells

III-V compound ingredients such as indium phosphide (InP), gallium Antimonide (GaSb) and gallium arsenide (GaAs) are utilized in the preparation process of

devices since such materials have some advantages such as a high coefficient of optical absorption that is a vital feature for obtaining ideal solar cells [84]. In addition, the InP and GaAs semiconductors have values of optimum bandgaps for a single-junction device, and this is why both materials are involved in the preparation process of devices [85, 86]. It was reported that the recorded efficiency is 21% for a GaAs/InP solar cell as a single p-n junction [87]. Even though solar cells made of III-V materials have higher efficiency compared with values obtained in solar cells based on Si, the fabrication cost of III-V solar cells is extremely high compared with those of p-n Si solar cells. Hence, this type of solar cell is not appropriate for the application of industrial.

2.3.2.6 Perovskite Solar cells

Materials based on organic-inorganic halide perovskite are used rather than those of solid-state used in Si solar cells. Materials of organic-inorganic halide are employed to fabricate a low cost and effective perovskite solar cell (PSC). The methylammonium lead trihalide ($CH_3NH_3PbX_3$) is commonly used as an absorber in these devices. The factor of X refers to a halogen atom such as chlorine, bromine and iodine. There is great benefit from the usage of this material since its optical bandgap is varied within the range of 1.5 and 2.3 eV. This is based on the concentration of the halide [88, 89]. In addition, the preparation method for this kind of device is simple. The schematic structure of the device is presented in Figure 2.20. The generation of carriers will be in the perovskite layer after absorbing the light. After that, holes and electrons move to the interface layers of electron and hole. Where polymers of the PTAA-class or PEDOT:PSS are used as layers of the hole interface. For layers of electron interface, TiO_2, C_{60}, PCBM and ZnO are employed. The efficiency of PSC

devices has been notably improved to 22 % [90, 91]. However, there are some disadvantages in these devices. Where it was reported that there is poor stability of prepared devices. Besides, the *J-V* curves of samples suffer from the hysteresis. In addition, the lead used in the preparation process is toxic.

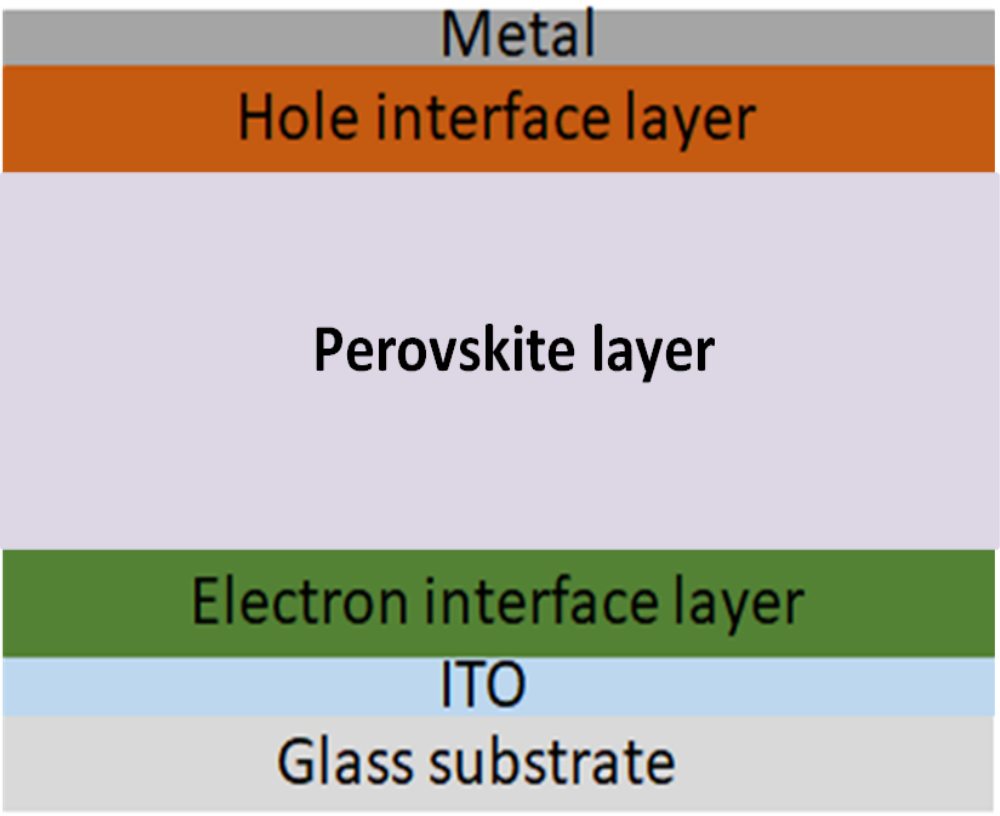

Figure 2- 20 Schematic of perovskite solar cell.

Unlike the application of p-n Si solar cells, the current issues result in the undesirable application of PSCs in the industry. At this time, there is an effort to solve the above challenges to obtain stable and low-cost devices [88].

2.3.3 Schottky solar cells

The p-n junction solar cell that is discussed in the previous sections shows high efficiency. Nevertheless, their preparation is complex and costly. Researchers

have worked on the reduction of that cost. A preparation method for Schottky junction solar cells is found to be simpler and lower cost than those used in the p-n junction solar cell. In the current device, one type of semiconductor such as n-type Si forms the

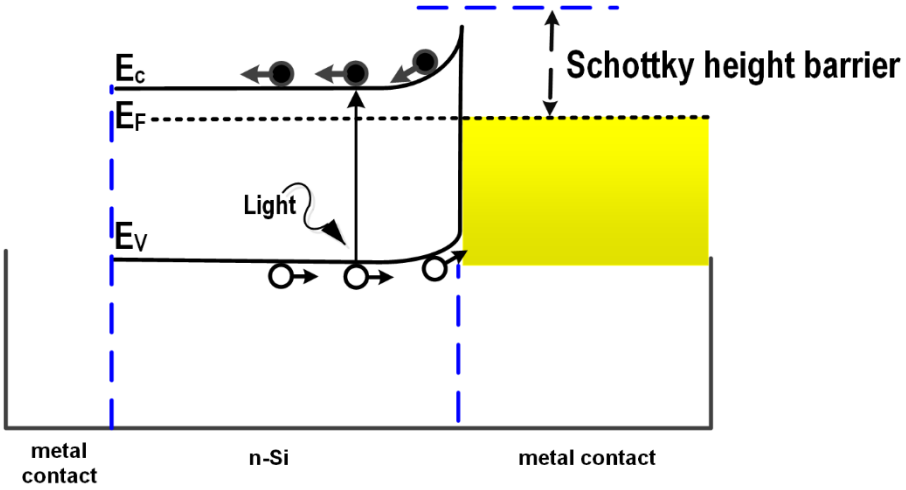

Figure 2- 21 Diagram of energy of a Schottky junction solar cell, showing the transfer of carriers.

junction with metal when their work functions are different enough as shown in Fig. 2.21 [92]. As observed, the process of generation for carriers is accomplished in the Si substrate. The rest of the photovoltaic processes are the same as those in the previous devices. One limitation of this device is the significant absorption by the metal layer, resulting in optical loss, as depicted. To mitigate this issue, a metal layer was replaced with indium-tin-oxide (ITO) film although it has a high production cost and is a limited resource [93, 94]. Besides, there is a decline in the efficiency due to the diffusion of indium ions. The third disadvantage of ITO is that it has a brittle nature. All these disadvantages of ITO cause its applicability within these cells to be limited [95, 96]. Hence, graphene has been utilized to circumvent problems of ITO.

2.4 Graphene features, properties, and application in Schottky junction solar cells

The exceptional properties of graphene have sparked significant research interest in its utilization [97]. One anticipated application for graphene lies in solar cells based on a Schottky junction. The characteristics and application of graphene in Si solar cells will be reviewed in the next sections.

2.4.1 Physical characteristics of graphene

Graphene has a two-dimensional (2D) sheet of atoms of carbon [96], as shown in Fig. 2.22. It displays the structure forms a triangular lattice, with 2 atoms, A and B, packed into each unit cell. Vectors of a_1 and a_2 represent the lattice per unit, and b_1 and b_2 are the vectors that represent the reciprocal-lattice, while the σ_i (i=1, 2, 3) are a nearest-neighbour vector. The attractive properties of graphene's structure are based on sp^2-hybridised carbon atoms. Carbon atoms contain six electrons, two in the inner shell and four in the outer shell, demonstrating the requirement for four electrons in chemical bond formation. Each carbon atom in graphene contributes three electrons to its bonds with its neighbours. Hence, the attractive electrical characteristics of graphene have contributed to the release of the fourth electron which is free. Graphene's adaptability is due to its carbon atom arrangement, which allows for various possible shapes [98]. Graphene is a two-dimensional substance that consists of a single sheet of atoms and has a thickness of around 0.4 nanometres. Graphene was discovered in 2004. Raman machine is used to measure the spectrum of graphene as presented in Fig. 2.23. The observed spectrum displays three prominent peaks: D, G, and 2D. The initial

peak corresponds to the D peak, signifying defects involved in double resonance for scattering at the

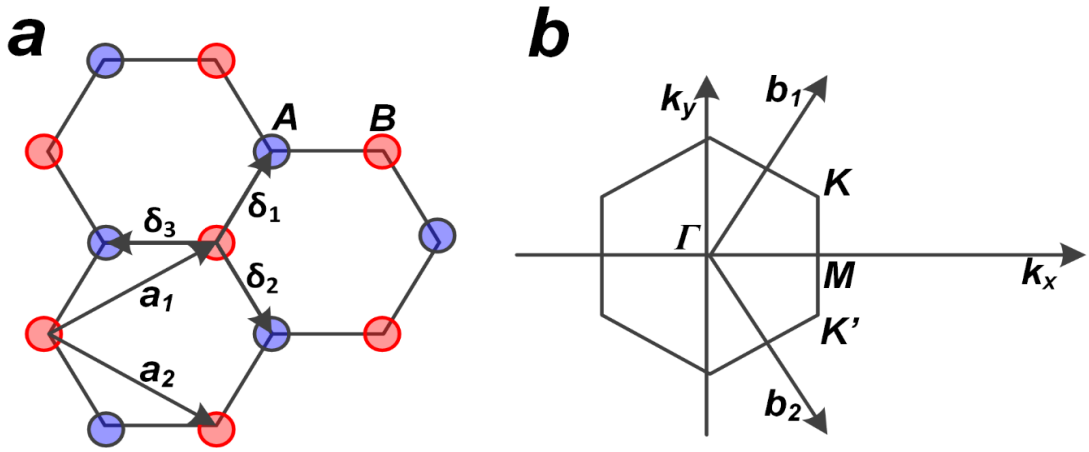

Figure 2- 22 (a) Lattice of a graphene sheet. (b) It's Brillouin zone.

K point of the Brillouin zone [99, 100]. It was reported that the laser frequency and defects affect the shape and position of the current peak. As shown, the D peak in the spectrum is usually weak and is located at about 1351 cm^{-1} [97]. The electron undergoes scattering by a phonon, leading to its transition into the second conduction band at the K' point. The electron subsequently scatters back to the K point to maintain energy conservation by absorbing another phonon. To preserve principles of momentum and energy, the electron scatters back to K which was its place before it recombines with a hole. Electrons in this process will scatter back to the first conduction band owing to defects [101-103]. Defects in graphene lattice come from the residue of PMMA or breaks in the symmetry, which could be grain boundaries [104], a vacancy [105, 106], sp^3-defects [107], and an edge [108-110]. The electron at the end of this process recombines with a hole, and a photon is emitted that forms the peak of D. The peak of G is the second peak in the spectrum, and it refers to the doubly degenerate in the plane of sp^2 for stretching mode [111]. It was also mentioned that materials such as

carbon nanotubes, amorphous carbon and graphite have the G peak [112]. The peak position

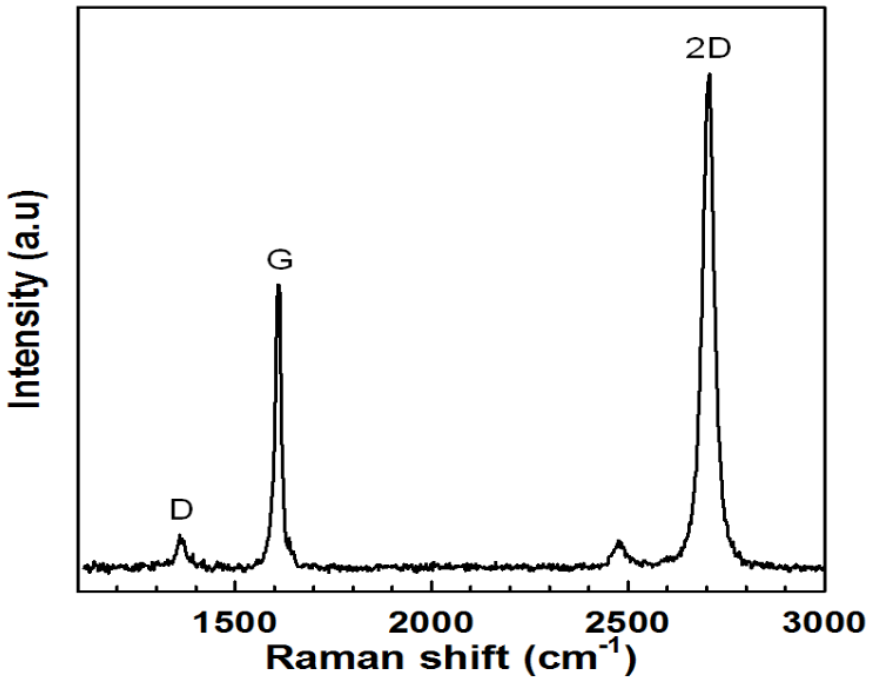

Figure 2- 23 Raman spectrum of graphene.

of G is affected by a doping stage in graphene. This occurs in a range of 1520 cm^{-1} to 1630 cm^{-1} [113, 114]. It was also presented that the position of this peak shifts to lower energies when the layer's number of graphene is increased [114, 115]. This means that the G peak in the spectrum gives details about the doping and number of graphene layers. A process of the single resonant gives the origin of this peak as observed in Fig. 2.24b. As detected, an electron resonantly is excited by the incident photon. After that, this electron recombines with a hole. This gives the emitting process of photons which gives the red shifted based on energy of phonons [116]. The final main peak is 2D which is the maximum peak in the spectrum of graphene. When layers of graphene are increased, the peak of 2D moves to higher energy. This position is

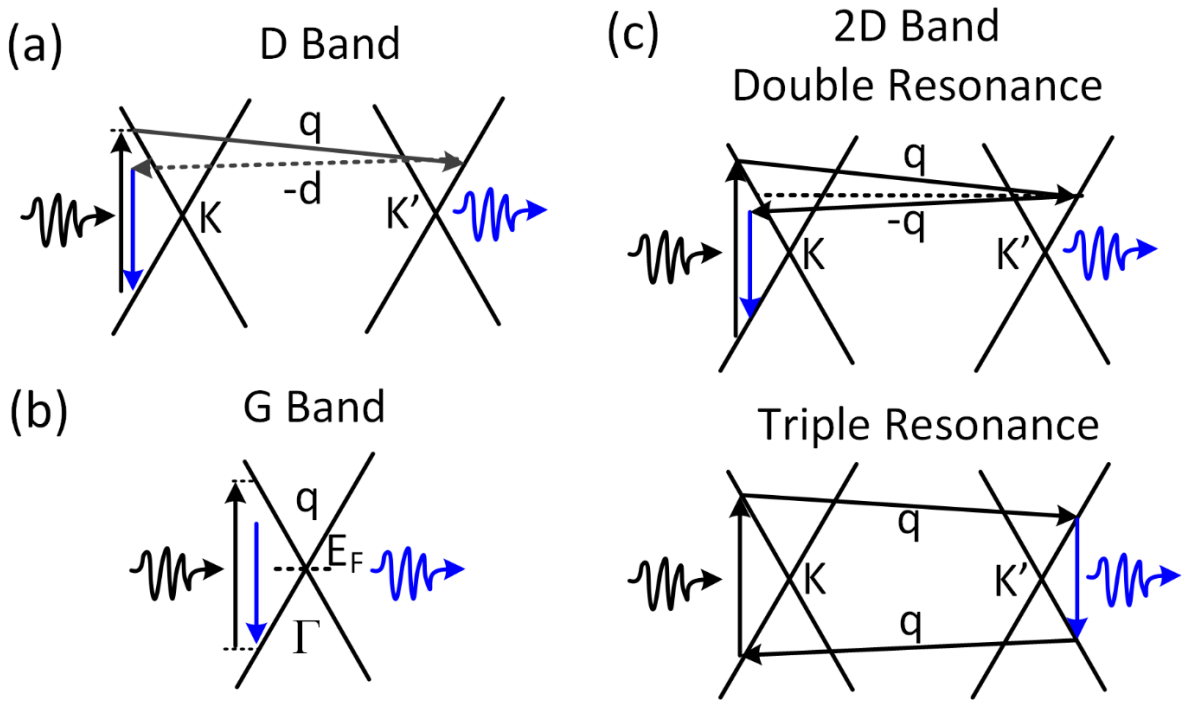

Figure 2- 24 Schematic of generation processes of Raman peaks in graphene spectrum. (a) D peak. (b) and (c) G and 2D peaks.

also affected by the level of doping in graphene. Where it was mentioned that the position of 2D is placed around 2700 cm^{-1}. The origin of the 2D is shown in Fig. 2.24c. As presented, the absorption of photons creates an electron-hole pair at the K in the FBZ. The electron undergoes scattering by a phonon, transitioning into the 2nd conduction band at the K' point. In order to conserve energy, the electron then scatters back to the K point by absorbing another phonon. This indicates that 2 phonons are needed for the generation process of this peak. After that, the electron combines with a hole in the band of valence. Due to that, a photon is emitted. The generation of the 2D is known as double resonant [97]. It was also reported that the 2D process could be generated through the triple resonant as displayed in Fig. 2.24c. As presented, the electron at the second Brillouin zone in the band of valence scatters to the 2^{nd} band of valence at K by absorbing a phonon [97, 117]. The nature and quality of graphene is depended

on the ratio of 2D to G (I_{2D}/I_G) peaks. The high-quality of graphene has a ratio of 2 [118]. The optical property is an additional unique factor for graphene since each layer of graphene transmits about 98% of the incident light. Graphene demonstrates a notable property in solar cell technology by reducing optical loss compared to metals. This characteristic enhances the potential of graphene in this application, presenting an intriguing prospect for further exploration. Where, a zero band gap of graphene enables the most of incident light to reach into the Si substrate in Schottky junction solar cells. It was described that the short current circuit is improved in solar cells created with graphene, and this is the reason for including graphene in solar cells [119].

2.4.2 Electronic characteristics of graphene

Another advantage of graphene is its zero-band gap, as shown in Fig. 2-25. This is a desirable property because the valence and conduction bands occupy the

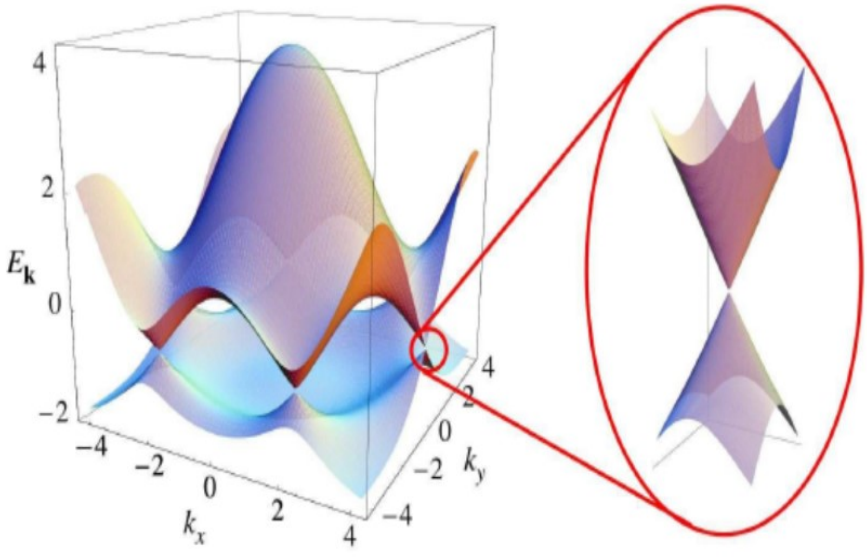

Figure 2- 25 Honeycomb electronic dispersion, energy spectrum (Left). Energy bands near a Dirac point zoomed in (Right) [120].

same space in the atom [119]. As stated in the earlier section, there are 6 electrons for each carbon atom, 2 and 4 electrons are at outer and inner shells.

Electron at outside shells contributes to the chemical bonding. Where 3 of them form 3 bonds of σ in a level of graphene lattice in the 2 dimensions. The 4th electron of the carbon atom forms bond of π in the 3rd dimension. These π bonds are located above and below the sheet of graphene [121, 122]. It has been reported that the 4th electrons of carbon atoms exhibit behaviour consistent with being massless at the Dirac points. Hence, these electrons provide the incredible electronic properties of graphene layers. The electrical features of graphene could be fund by sheet resistance, contact resistance and Dirac points [123]. Hence, these electrons provide the incredible electronic properties of graphene layers. The electrical features of graphene could be fund by sheet resistance, contact resistance and Dirac points [123].

2.4.3 Efficiency development of solar cells based on graphene and silicon Schottky junctions

Since 2010, graphene has been used to manufacture Si solar cells [124]. It has been reported that solar cells constructed with graphene and silicon as Schottky junctions can be prepared as three structures, which are top window [124], top grid [125] and back contact [126]. One of these structures is commonly demonstrated and made with a top window design, as shown in Figure 2.26. As displayed, the layer of SiO_2 with a thickness of around 300 nm is designed onto a Si wafer after a cleaning procedure. A top window of Metal/SiO_2 layers is formed via complex lithography and etching processes. Subsequently, using the wet transfer procedure, a chemical vapor deposition (CVD) graphene is transferred onto Si wafers to form the junction of this type of solar cells. Another metal, such as Al, is coated at the bottom of the Si wafer to produce the ohmic contacts that

complete the device [44, 127, 128]. The Schottky junction is formed at the interface between graphene and silicon substrate. The light absorption is occurring in the whole of Si substrate, and carries (electrons and holes) will be generated and separated by the built-in field at the graphene/Si junction. Then, the generated photocurrent will be obtained after reaching carries to graphene and ohmic contact. The efficiency of the first device prepared with an active area of 3.3mm×3.3mm was 1.34% [36]. The devices had a major drawback: a significant reduction in the open circuit voltage (Voc) due to leakage current.

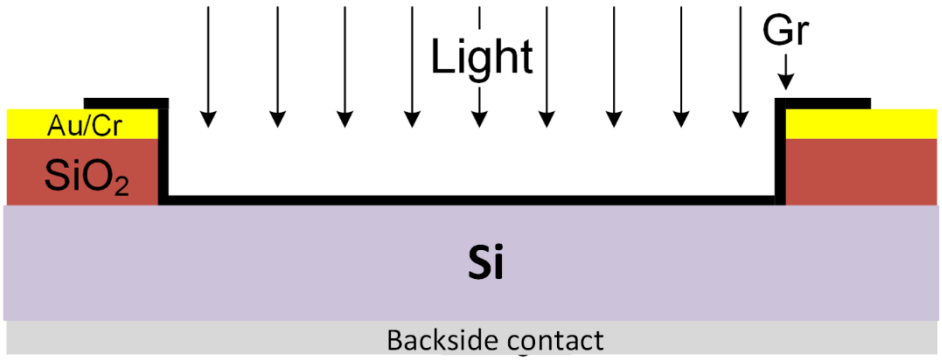

Figure 2- 26 A top-window design for a graphene/Si Schottky junction.

Several studies reported at low Schottky barrier behind the leakage current at the graphene/Si junction [92]. Later, the graphene work function was improved and managed via chemical doping [128]. The use of this doping raises the barrier height and increases the potential that is already built in.

To develop the performance further, researchers have constructed the junction of solar cells using multi-graphene layers, known as MGL. They achieved an efficiency of 2.1% without doping. It was hypothesized that the enhanced movement of carriers was responsible for the observed rise in solar cell efficiency when MGL was used. Likewise, it was discovered that the sheet resistance of graphene samples correspondingly decreases by introducing MGL [44].

Consequently, the photovoltaic characteristics were improved by doping, and an efficiency of about 9% was attained for the doped graphene/silicon solar cells [128]. However, a 2014 study revealed that chemical doping is ineffective for enhancing the Schottky barrier at the graphene/Si junction since the *J-V* characteristics have an s-shape after few days. In 2014, Si wafers were covered with a 2 nm GO layer and transferred with a monolayer graphene layer instead of the doping process to produce greater efficiency [129]. It was also reported that doping achieved by an external electric field is more suitable than chemical doping [130]. Nevertheless, the fabrication process of those devices is still more complicated than that of previous devices. The performance of a graphene/n-Si Schottky junction solar cell was improved by other researchers who were able to reduce the reflectance of silicon to less than 40%. High reflectivity causes optical loss, which reduces the efficiency of solar cells. Texturing was utilized in this case to lower the reflectance of Si. However, it was discovered that carriers are recombined at the graphene/textured Si interfaces, resulting in low solar cell efficiency [129, 131]. Antireflection coating layers, such as a layer of TiO_2, were employed on the silicon substrates to gain a reduction in the reflectivity of the substrates, which was brought down to 30%. This procedure potentially enhanced efficiency by about 10% [132].

Additionally, it has extensively been documented that an s-shaped pattern in the *J-V* graphs is a significant problem for the deterioration of graphene/n-Si Schottky junction solar cells, which results in a significant drop in efficiency. This means there is an important drop with time in the amount of energy that can be generated by the solar cell [36, 129, 132-137]. At that point, the problem was fixed by placing an extremely thin covering of SiO_2 on Si wafers before transferring graphene, and it proved to be successful features of devices [133]. As a result, doping

methodologies, such as chemical and electrostatic gating, have been developed to eliminate the s-shape [132, 135, 136, 138, 139]. On the other hand, after some time, an s-shaped line was again seen in the *J-V* graphs of graphene/Si devices [140]. It was recently proven that the PMMA residue that is obtained after the wet transfer process is the major source of the s-shape [126, 141]. As illustrated in Figure 2.27, a research study was conducted and showed that the fabrication of solar cells with the help of the top-grid structure increases the active area of the devices. The active area of prepared devices is larger

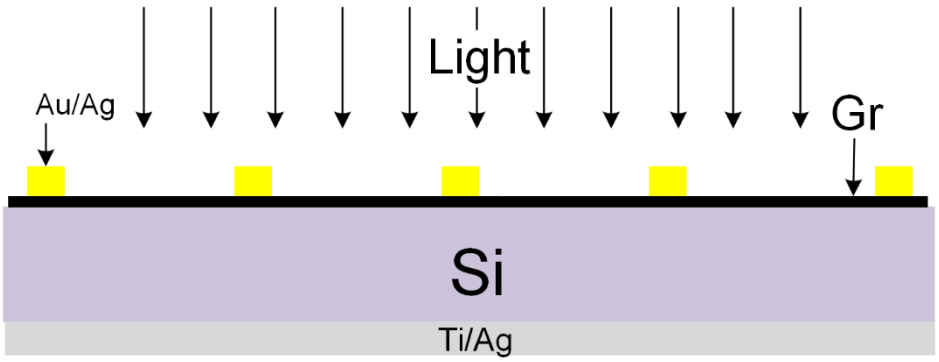

Figure 2- 27 Top grid structure of the graphene solar cell.

than 0.1 cm^2 [125]. There was hope at the time that increasing the area of a graphene/n-Si Schottky junction solar cell would boost its efficiency. Nevertheless, the study indicated that devices made with an area more than 0.1 cm^2 are less efficient than those made with a 0.1 cm^2 area. It has been reported that the quality of a Schottky junction is poor when the graphene area, which forms the junction, is greater than 0.1 cm^2 [125, 133]. This means that the graphene area plays an important role in this type of solar cells. The active area of solar cells was successfully improved after using the back contact construction (observed in Fig. 2.28). In this structure, the active area extended to 0.19 cm^2, while graphene with an equivalent area of 0.1 cm^2 was utilized as junctions. [126,

141]. There is a disadvantage of the back contact construction when MGL is applied to form the junction, which needs the etching process of graphene. This marks in increased complexity of the fabrication process. In conclusion, graphene has demonstrated great developments after being it in Si solar cells as displayed in Table 2.1. The recorded efficiency was 15.6% after introducing native oxide, doping and ARC techniques as presented in this table. This means the manufacturing of silicon solar cells utilizing graphene was an easier procedure compared to the techniques utilized to make other types of silicon solar

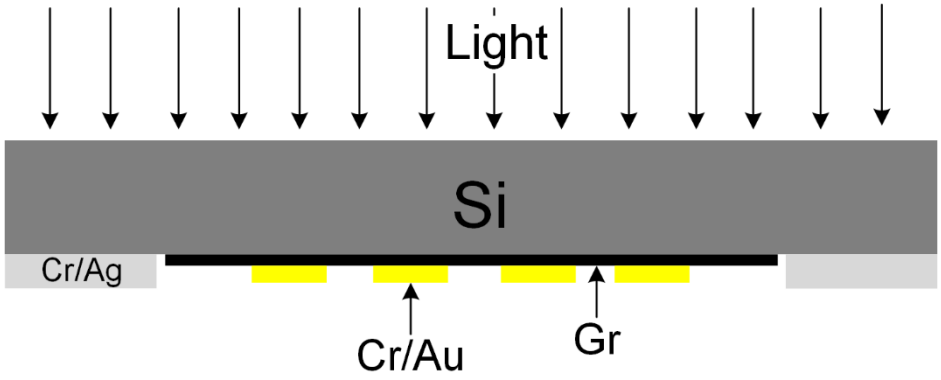

Figure 2- 28 Back-contact structure fabrication method for graphene/Si Schottky junction solar cells.

Table 2- 1 Comparative analysis of reported solar cells that have the highest *PCE*s.

Applied procedures	*PCE (%)*	References
Top grid after doping	5.9	[125]
Top window after doping	9.18	[128]
Texture and doping process for back contact	14.1	[126]
Interfacial oxide, doping and ARC for top window	15.6	[133]

cells that were ported in Chapter 2. However, the development of graphene/n-Si Schottky junction solar cells still needs extra effort to achieve higher efficiency

and more stable doped devices. Additionally, the creation of devices that make use of the top window structure requires more research to simplify the process. To attain the goal of further enhancement of the ideal device, the elimination process of PMMA must be researched and simplified since residue is the major factor in the reduction of the performance. Moreover, research is needed on the evaporation of chemical doping over time since the s-shape will eventually reappear, leading to an unstable doped device with poor efficiency. In chapters 4 and 5, the above issues will be solved by using novel techniques.

3 Classification and experimental methods

3.1 Classification Methods

3.1.1 Optical Microscope

To exam the quality of patterns during the lithography process, an optical microscope (see Figure 3.1a) was used for an inspection process. It was also used to examine the quality of graphene layers after a transferring procedure. This examination aimed to assess how clean and uniform the graphene deposits are, as seen in Figure 3.1b. Fig 3.2a illustrates a diagram of the optical reflection and transmission of the white light source. Fresnel's principle is the physics principle of this technique [94]. It is clear from this diagram that there are three different interfaces, one for each of the graphene, SiO_2, and Si layers. at each interface nearly a part of the light beam that reaches the interface will be reflected, while the remaining light will be transmitted. This occurs regardless of whether or not there is a gap between the contacts and denotes the existence of a multiplicity of feasible optical routes. Hence,

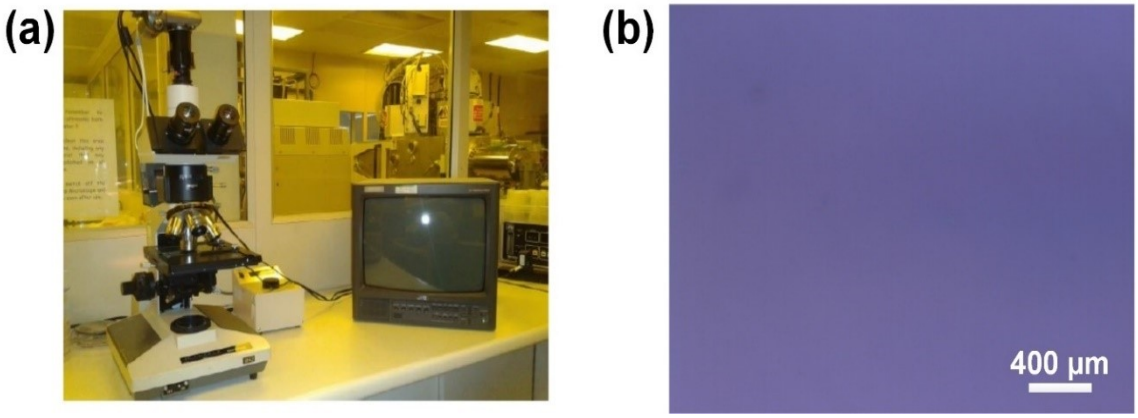

Figure 3- 1 (a) An image of Optical Microscope. (b) An optical picture of transferred graphene.

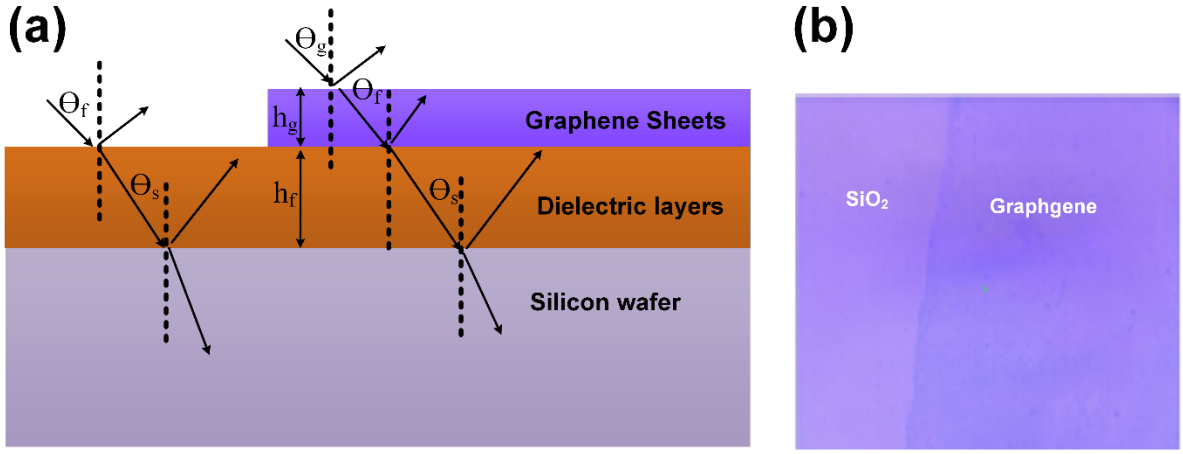

Figure 3- 2 (a) Schematic of an optical process of reflected and transmitted rays. (b) An optical picture of graphene that has been coated on SiO_2 substrates.

the intensity of the reflected light that enables graphene layers to be visible on the SiO_2/Si substrate is due to interference between all the optical paths, as illustrated in Figure 3.2b. This interference is depicted in the image [142], which is viewed. The contrast spectra of the reflected light from the sample are in good agreement with the optical pictures that were acquired (see Fig.3.2b).

3.1.2 Raman Spectroscopy

To review the naturality of a transferred graphene film, doping process and shifts regarding the minimization of PMMA residue, Raman spectroscopy was utilized, as seen in Fig.3.3a. The notion that inelastic scattering of monochromatic light is central to Raman spectroscopy is graphically represented in Figure 3.3b, and it is the core concept behind the field. During the inelastic scattering process, the photon's frequency will shift due to the interaction of an incoming photon with the molecules in

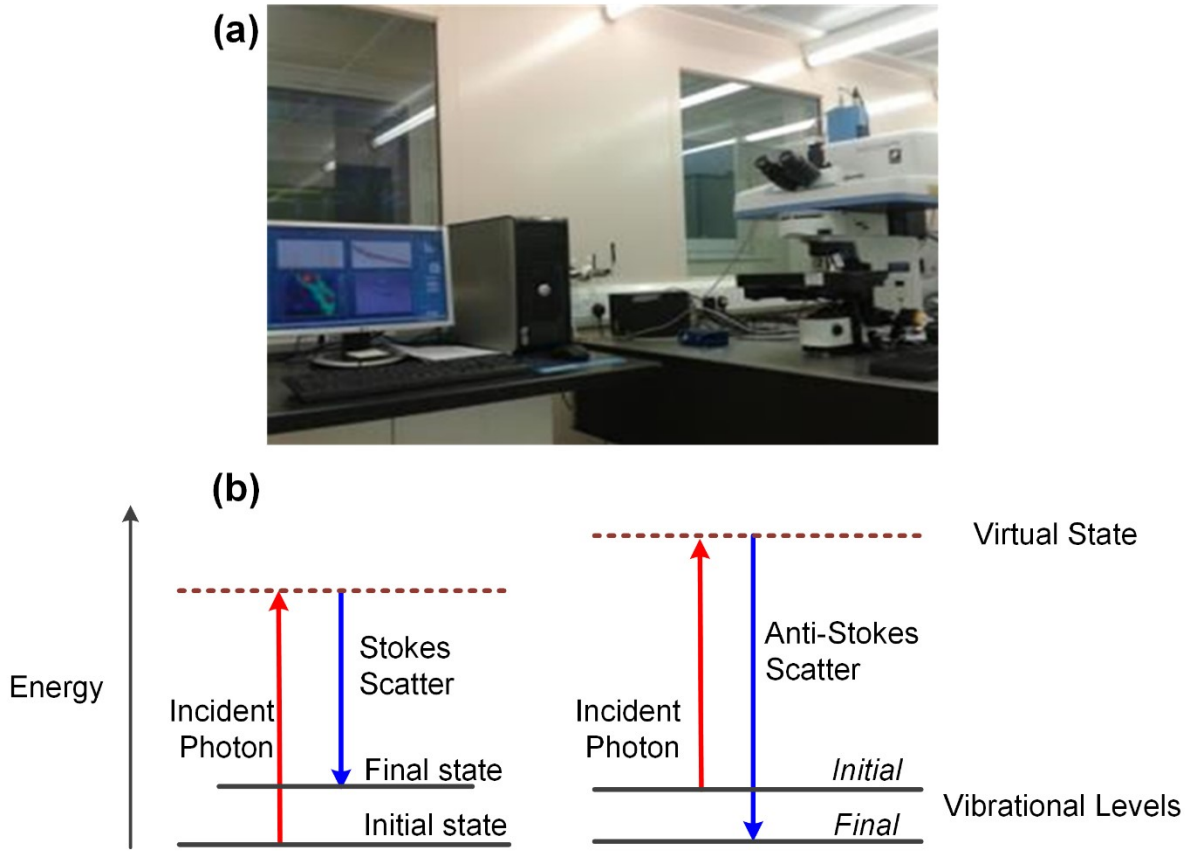

Figure 3- 3 (a) An image of Raman Spectroscopy. (b) A schematic of Stokes and anti-Stokes scattering processes.

graphene, which will cause the photon to scatter more or less efficiently. When molecules get a photon with frequency (ν_0) at the ground state, the proton will be stimulated to a virtual state (ν_m), resulting in the virtual state having that frequency. Different scattering processes are distinguished by their names, which are Stokes and anti-Stokes Scatterings. When the excited molecule returns to an energy state lower than its initial state, this is known as anti-Stokes scattering, and when it returns to an energy state higher than its initial state, this is known as Stokes Scattering. A material's molecular structure and defect density may be deduced from variations in wavelengths. The dispersed light may be examined to determine this [143]. Typically, graphene that has been put onto SiO_2/Si substrates exhibits Raman spectra with three primary bands. The D band is seen at a frequency of about 1350 cm^{-1} and visual representations of the irregularities

within the graphene lattice. The strength of this band is proportional to the amount of disorder. The band of G is positioned at around 1580 cm^{-1}, and it reflects the material's crystallinity and symmetry. This is generated by the E_{2g} mode in the centre of the doubly degenerate zone. Lastly, the 2D band, commonly known as the band of G', is placed at approximately 2700 cm^{-1}. This band is created through the second-order zone-boundary phonons. It was reported that Raman Spectroscopy is the key tool for gaining the key factors of transferred CVD-graphene. Based on the Raman spectrum of graphene samples, it can be noticed that there are peaks of D, G, and 2D. These peaks give details about the quality and doping level in graphene. The intensity of the peak of D presents the number of defects in the graphene lattice. It was reported that high-quality graphene should have a small D peak. Besides, it was mentioned that the great intensity of the peak of D refers to PMMA residue on transferred graphene [141]. This indicates that the decrease in PMMA residue on the surface of graphene results in a reduction in the intensity of the D peak. Additionally, it has been established that the intensity ratios of the 2D to G peaks (I_{2D}/I_G) can offer insights into the quality of the graphene. For example, graphene has excellent quality if the ratio is greater than 1.5. Additionally, it was shown that the intensity of the peak of 2D in the spectrum of a monolayer of graphene is more extreme than that of the G peak. Furthermore, the intensity of the peak of 2D will be reduced when the number of layers of graphene is increased. It was also displayed that details about doping levels in graphene are recognized by the shifting of 2D and G peaks before and after doping [144, 145]. Based on this, there are blue and red shifts in the Raman spectrum. The red shift refers to an expansion in the level of n-doping in graphene. In this case, the position of peaks (2D and G) for treated graphene with dopants moves towards the lower wavenumber compared with those before

the treatment. The redshift phenomenon is observed when the PMMA residue on graphene samples undergoes reduction, while the blue-shift denotes an elevation in the level of p-doping in graphene. Consequently, the peak positions of 2D and G for doped graphene shift towards higher wavenumbers compared to their pre-doping levels. [126, 141, 146, 147]. It can be observed that the Raman spectrum acts a vital part in transferred CVD-graphene. This is what is going to be noticed in Chapters 4 and 5.

3.1.3 Key-sight B1500A semiconductor Analyser

As shown in Fig.3.4a, a performance analyser called a key-sight B1500A semiconductor analyser was used to determine the *J-V* curves of manufactured solar cells. Solar cells in this equipment are measured at specific parameters: temperature 25 ^{o}C (as seen in Fig. 3.4b), 1.5 Air mass and 100 mW cm^{2} illumination intensity of a halogen lamp. A typical Si commercial solar cell is utilized as a point of reference for calibrating the device. A typical four-probe measurement shown in Fig. 3.4d is provided by this machine and applied to explore the electrical features of graphene-constructed on Dirac point and sheet resistance after the fabrication of graphene-based back-gated field effect transistors (FETs) displayed in Fig. 3.4c. Where, the four-probe is a technique for measuring the material's resistivity. By applying a current through outside probes and determining the voltage through the inside probes, leading to a assess of the resistivity.

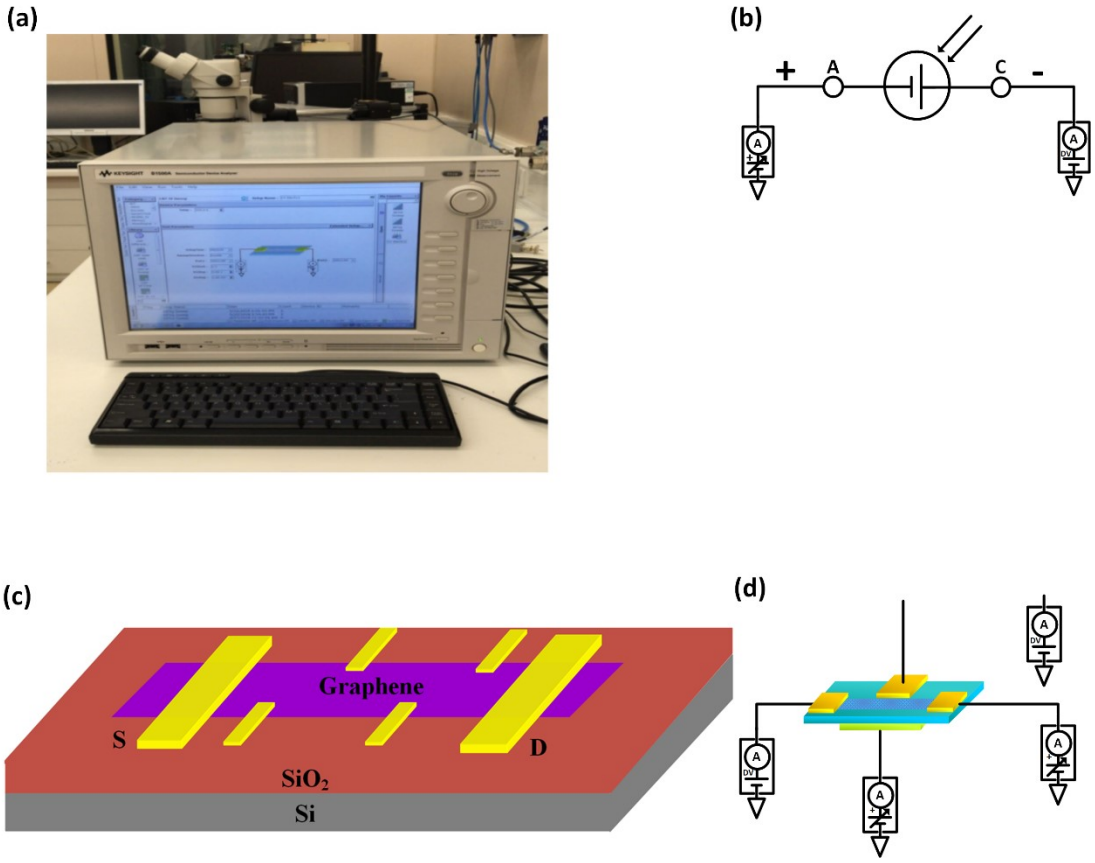

Figure 3- 4 (a) a photo shows the optical display of a Keysight B1500A semiconductor Analyser. (b) Performance and measurement of *J-V* for solar cells. (c) A back-gated FET . (d) A diagram of four-prop measurements.

3.1.4 X-Ray Photoelectron Spectroscopy (XPS)

To further examine the residue of PMMA remaining on the plane of graphene once the wet transfer process, X-ray photoelectron Spectroscopy (XPS) was conducted. The chemical and elemental makeup of a surface is verified by using this machine. The experiments were conducted at the Harwell XPS facility at the Rutherford Appleton Laboratory using a monochromatic Al Kα emission at 1486.6 eV. The Kratos AXIS Ultra DLD spectrometer requires 150W to operate. Samples are measured using the fixed analyser transmission (FAT) mode, which operates at 80 eV for broad scans and 20 eV for fine-resolution measurements. It is possible to determine the elemental data of the chemical states, and the

elemental compositions of the material based on the electrons released from a few nanometres of the material.

3.1.5 Nkd-7000 spectrophotometer system

The spectrophotometer depicted in Figure 3.5 is the instrument employed in determining the reflectance of graphene/Si samples before and after the application of anti-reflected PMMA layers. Light from a source with a spectral range of 200 to 1100 nanometres is combined with a concave and collimating mirror, a diffraction grating, a photodetector, and a slit to form this apparatus. The area beside the entrance is bathed in natural light since that is where the door is situated. A concave mirror focuses the light from all the sources to be projected onto a grating. The grating diffuses the light's spectral components out in all directions. A second concave mirror then focuses the light before it is projected onto the detector. The detector's output signal is sent to a digital processor after being photographed by light. After that, the software of this technique inserts signals and shows the result as an operation of wavelengths.

Figure 3- 5 A picture of Nkd-7000 spectrophotometer.

3.1.6 External quantum efficiency system

To measure External Quantum efficiency (EQE), the PVE300 system was used. This system evaluates the efficiency of prepared graphene/Si Schottky solar cells. The task of making this measurement lies with Bentham Instruments Ltd. The structure consists of monochromators, a chopper, collimating lens filters, digital conversion software, and an Xe lamp that emits light ranging from 300 to 1800 nm. The system's underlying principle is based on the correlation between the number of photons that hit a solar cell, and several carriers produced in the cell. In equation 3.1, it can be seen that an EQE represents this proportion. The cell must be exposed to the light coming from the source in order to take this

measurement. The light is then modulated at a frequency of 30 Hz by a monochromatic, which causes the wavelength of the light to change. When the silicon samples have absorbed the incoming light, electron-hole pairs are formed for each wavelength. Hence, the system's software presents the EQE's spectral distribution regarding the wavelength of the light falling onto it, based on the equation below [148]:

$$EQE\ (\lambda) = \frac{number\ of\ collected\ carriers}{number\ of\ incident\ photons} \qquad (3.1)$$

3.1.7 Atomic Force Microscopy (AFM) system

Using atomic force microscopy (AFM), Pacific Nanotechnology, is to determine the coatings' thickness on coated metals (Au, Cr, and Ag). Fig. 3.6a depicts an optical image of the system that was utilized. The system consists of a mechanical measuring unit, an electronic controller, and matching software. This image was created using the system that was employed. The atomic force microscope (AFM) block diagram in Figure 3.6b includes a cantilever with a pointed tip. When the cantilever's tip moves closer to a sample, the force acting between the sample and tip causes the cantilever

to bend under Hooke's law, which states as follows:

$$F = -kx \qquad (3.2)$$

K is the cantilever's spring constant, and x is the distance between the sample and the probe's tip [149]. At this point, the cantilever will no longer be in the lighting path of the laser beam, and it will instead go toward a photodiode. The amount of cantilever deflection triggers an electrical signal to be sent to the photodiode's reaction. The signal varies depending on the cantilever's position in the equilibrium sample. The final

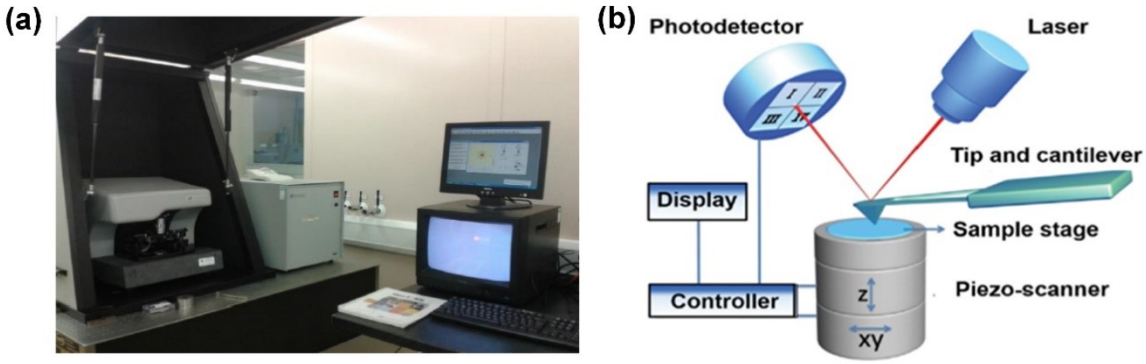

Figure 3- 6 (a) An image of the AFM instrument. (b) AFM Functional Block Diagram [149].

step involves translating those electrical impulses into two-dimensional and three-dimensional pictures of the sample's surface [150].

3.2 Experimental techniques

3.2.1 Photolithography and Lift-off

Fig. 3.7 illustrates the standard photolithography technique commonly used for device fabrication in the semiconductor industry. The Optical Associates INC (OAI) instrument shown in this figure was used for lithography. This technique was introduced to create the top window structure to avoid the complex etching process of SiO_2 thermally forming onto Si substrates. The lithography procedure began with a spin-coating of photoresist that lasted 30 seconds and was performed at 3000 revolutions per minute. Then, the photoresist was solidified by prebaked substrates using a plate at 100 °C for one minute, as S1813 photoresist resist was used, and substrates exposure under UV with the specific mask for 35 seconds. Next, substrates were submerged in the photoresist developer for 15 seconds and soaked with DI water for around 30 seconds. After applying the nitrogen (N_2) gun to the dry substrates, they were put through the post-baking process at 110 degrees Celsius for twenty minutes. For GFETs, the post baking

was achieved under DUV of 254 nm at 180 degrees Celsius for 2 min to avoid burning the photoresist through the sputtering. The post-baking process was required to remove water completely from the surface. After this step, the substrates were prepared for the fabrication procedure. After that, the sputtering part was applied to calibrate the deposition rate of metals. Next, with the aid of 1165 photoresist remover and ultrasonic bath, the photoresist was removed. However, this step is omitted in the process of fabricating GFETs as the surface of the graphene would badly be affected.

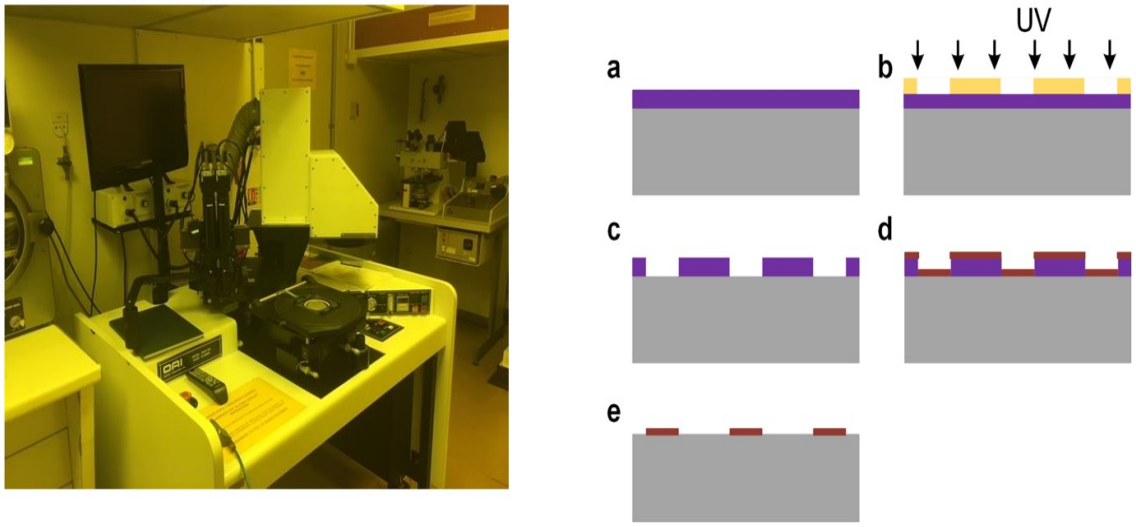

Figure 3- 7 An optical view of the mask aligner in the cleanroom (left). An illustration showing the photolithography and lift-off processes (right), (a) A spin coating is used to apply a layer of photoresist to a substrate. (b) Subjecting the area to UV light for a predetermined amount of time while wearing a mask with a predetermined pattern. (c) Eliminating the positive photoresist that has been exposed by applying developer. (d) The process of sputtering a layer (e) Processing the lift-off operation with the help of the remover.

Finally, the substrates were washed with DI water and dried using an N_2 gun. For creating patterns of GFETs, samples were left in the remover overnight to achieve the lift-off step.

3.2.2 Sputtering process

Sputtering equipment, manufactured by Nordiko Ltd, shown in Figure 3.8a, was applied to form films of varying thicknesses to a substrate. The top-window section, which consists of Au/Cr/SiO_2, and the rear side contact, which is Ag/Cr, were fabricated using this machine and placed onto Si substrates, as seen in Fig. 3.10c. Au/Cr contacts of GFETs shown in Fog.3.4c were also formed using the sputtering method. The hour leading up to the beginning of the event was spent warming up the equipment that would be utilized. The vacuum chamber was subsequently loaded with clean substrates, and the machine was forced down to a pressure of around $6x10^{-7}$ Torr. Before the coating process could begin, all of the chamber's targets needed to be cleaned. As a result, an argon plasma was used to clean each target for twenty minutes at a power setting of two hundred watts. Over the entirety of the manufacturing process, the pressure of the argon and the power supply was held constant at four mTorr and 200 W, respectively. In addition, the substrate was cooled using water to prevent damage from thermal stress. The sputtering process involves the expulsion of atoms at the target's surface due to the action of powerful argon atoms that bombard the target. This is the fundamental idea behind the procedure. After this, atoms at the target's surface are ejected towards the direction of the substrate because the hitting energy is significantly larger than the binding energy, as illustrated in Figure 3.8b. This process is guided by the electric field that develops between the target and the substrate. The atoms of certain metals, such as gold and silver, will be

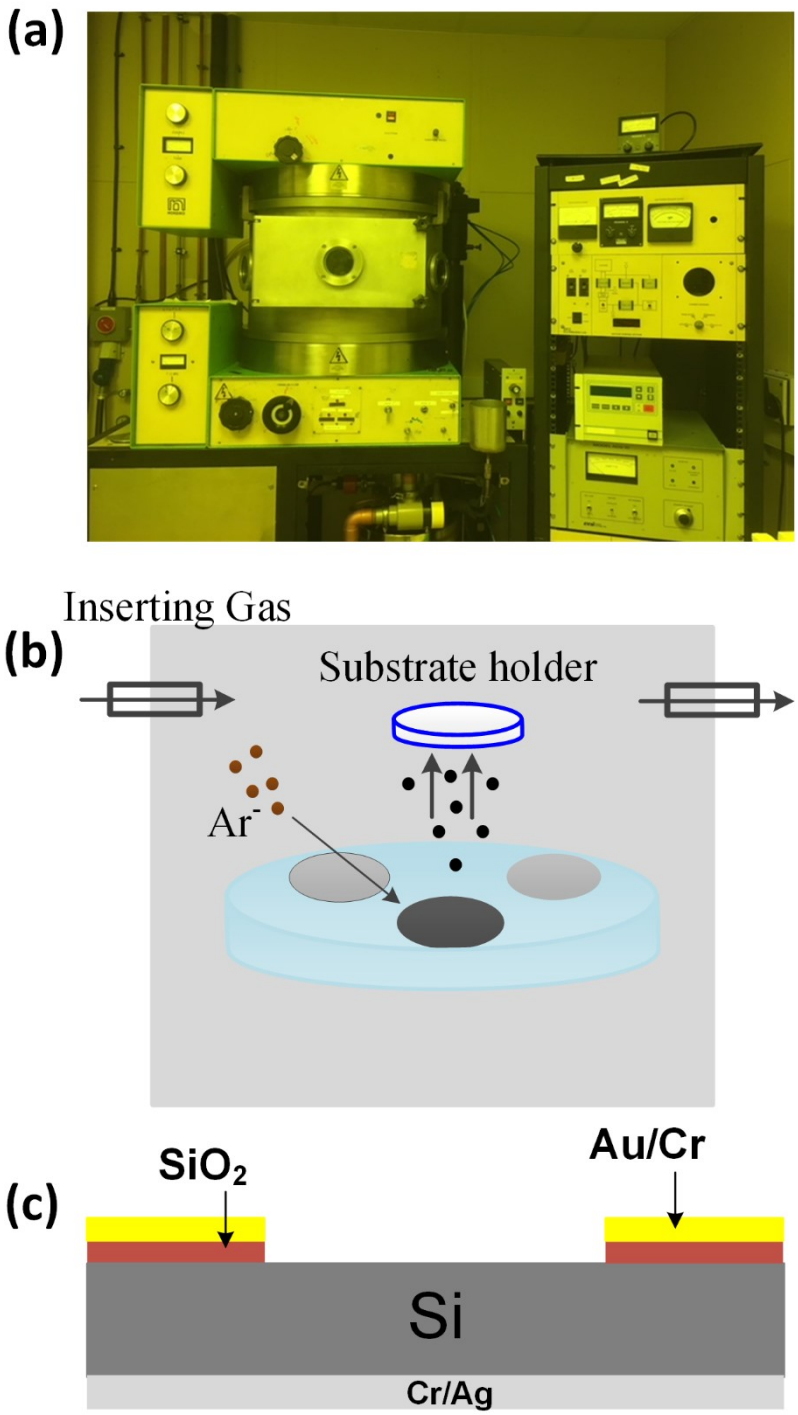

Figure 3- 8 (a) An optical image of a sputtering machine. (b) Schematic of the conventional sputtering process. (c) Schematic Si substrate with the top window and back side contact.

sputtered toward the substrate through regular trajectories as they go closer to the surface.

3.2.3 Chemical vapor deposition method

To successfully build solar cells using graphene, it should be of high quality and have a large area. While several techniques exist for preparing graphene, including scotch tape [151], sputtering, reduction of graphene oxide, exfoliation in a liquid phase and epitaxial growth on a SiC substrate [124, 152, 153], the prepared graphene using those methods has poor quality. Consequently, a chemical vapor deposition (CVD) technique was employed. It proved to be the most effective technique for creating graphene that possessed both excellent quality and a large area [124]. The catalytic impact of metals was utilized in this method to encourage the formation of graphene [154, 155]. Layers of graphene-coated on both sides of metals like copper and nickel have a greater carbon solubility when heated to high temperatures. This technique involves a pre-annealing procedure of the surface of the metal, which is done in a vacuum under a range from 800 to 1000 ^{o}C, as shown in Fig. 3.9. Following that, the chamber of the furnace is loaded with the molecules comprising the short chain of hydrocarbons [156, 157]. Adsorption of carbon atoms onto the metal surface leads to the growth of graphene on the metal's surface [124, 152, 153]. Other aspects need to be considered, including concentration and gas flow rate [158], the annealing procedure [159], the grain size of the metal [160, 161] and the cooling time [159]. These factors play vital roles in the performance of graphene formed by this method.

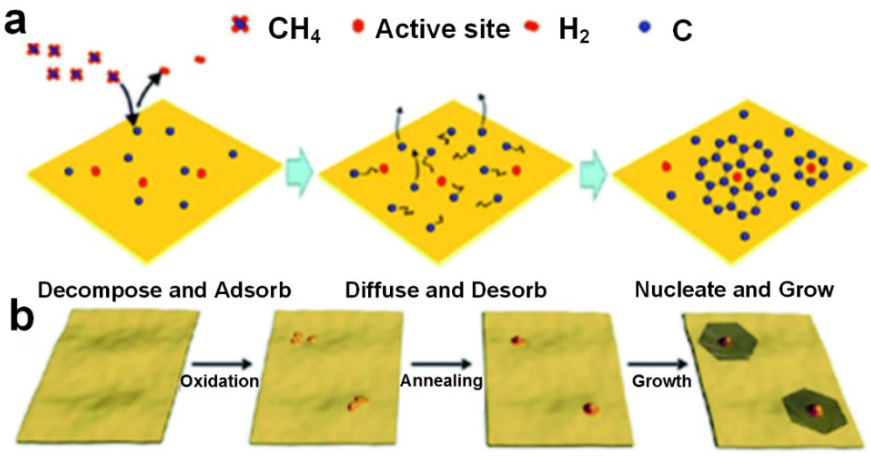

Figure 3- 9 An illustration in the form of a schematic illustrating the growth involved in the CVD method of growing graphene. (a) Chemical Vapor Deposition is used as a growth procedure. (b) Schematic representation of the pre-CVD process, which involves a low-level oxidation step followed by a reductive heat treatment [162].

3.2.4 Wet transfer process

As can be seen in Figure 3.10, a procedure of wet transfer was utilized in order to accomplish the relocated graphene of solar cells and GFETs. Poly(methyl methacrylate) (PMMA) was achieved based on the reported works [126, 147, 163]. The PMMA first dissolved in chlorobenzene at a concentration of 46 mg/mL before being spin-coated onto the graphene layer at 3000 rpm for 30 seconds, leading to a PMMA layer thickness that was close to 100 nm. Next, samples were taken to be dried on a hot plate at a temperature of 180 ^{o}C for one minute in the air that was present in the laboratory. To remove the copper substrate, the samples were submerged in a mixture of 3:1 DIW to HNO_3 for three minutes. The samples were then moved to 0.1M ammonium persulfate for three hours so that the copper substrate could be etched. The etching process was completely considered when the copper was no longer visible. In addition, trials were etched for a further three hours in an ammonium persulfate bath to guarantee that copper

had been detached entirely. The PMMA and graphene layers were then placed onto samples after being submerged in a bath of DI water for twenty minutes. The samples produced were then sealed and put into a

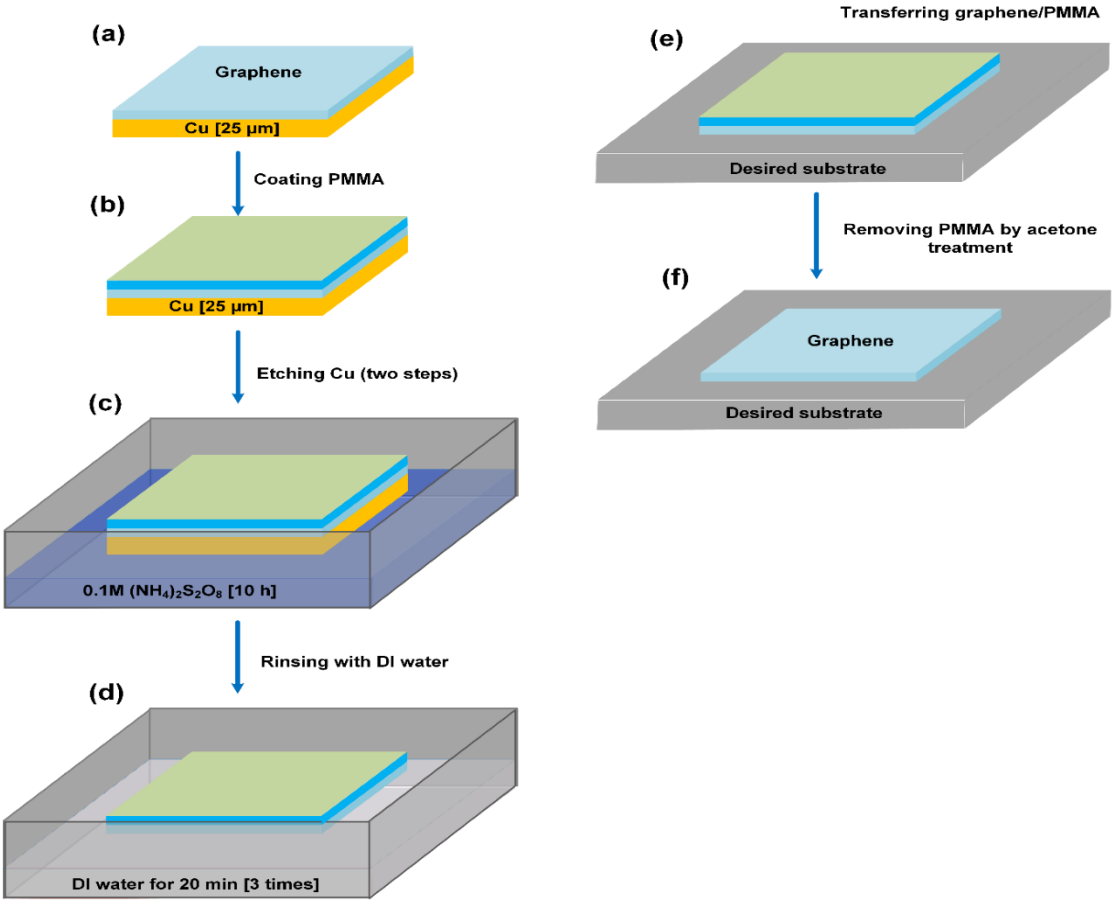

Figure 3- 10 Steps involved in the wet transfer procedure. (a) Forming graphene layers on both sides of Cu. (b) Spinning PMMA layer onto graphene. (c) Removing the second graphene layer and Cu by HNO_3 and ammonium persulfate. (d) Transferring PMMA/graphene layers into a bath of DI water. (e) Shifting layers of PMMA/graphene. (f) Removing PMMA by acetone, IPA and DI water.

vacuum at 10^{-3} Torr pressure for five hours. After this procedure, samples were roasted in the air at a temperature of 220 degrees Celsius for five minutes, allowing the PMMA to re-flow. To get rid of the layer of PMMA on top of the graphene, the samples were submerged in acetone at a temperature of 50 degrees Celsius for half an hour. Finally, samples were washed by being submerged in IPA and DI water.

3.2.5 Substrate Cleaning

Two cleaning methods were used following the cutting of silicon substrates with an area of 1 cm^2. The first step in the procedure is preliminary cleaning, and it consists of submerging substrates in a solution containing 98% H_2SO_4 and 30% H_2O_2 in 2:1 to 4:1 volume ratio at around 110 ^oC for 15 minutes. Wet-chemical oxidation successfully destroyed and removed organic pollutants, but it had little effect on inorganic contaminants such as metals. Samples were then submerged in DI water for two minutes. The native oxide was removed by using a novel technique that involved soaking samples in 40% KOH for three minutes at 60 ^oC, followed by a two-minute rinse in DI water. Following this, the Radio Corporation of America's clean-up was completed. During this stage, any trace metals and alkali residues that were still present on the surface of the silicon were dissolved and removed by a mixture of 5:1:1 to 7:2:1 (volume-wise) H_2O, 30% H_2O_2 and 29% NH_4OH for ten minutes under heating at 70 ^oC. The process ended with a two-minute quench and overflow rinse in DI water. After that, the samples were heated to 75 ^oC for five minutes while submerged in a mixture of 6 parts H_2O, 1-part HCl, and 1-part HCl by weight. In the last phase, the substrates were washed in DI water for two minutes. Samples then underwent a drying procedure in which N_2 gas was used.

3.2.6 Device Fabrication

Solar cells with a structure of the top window were simply manufactured in this work by a sputtered SiO_2 layer and standard photolithography techniques. Other strategies for removing PMMA residue are now being developed. Chapters 4 and 5 will cover the developments mentioned earlier. In order to get substrates made of Si ready for use in devices, they were cleaned. Then, samples remained in ambient conditions for 2 hrs to form the native oxide [164]. Once the substrates

had been through the normal photolithography process, a layer of SiO_2 was sputtered on them to function as a window. The SiO_2 layer was sputtered under a vacuum of 10^{-7} torr with 4 m Torr Argon gas and 400 Watt. These factors of the sputtering process were chosen based on the reported work [165] to ensure the high quality of SiO_2 layers. On top of the SiO_2 layer, gold (80 nm) and chromium (5 nm) coatings were sputtered to create the front contact. After that, Cr (5 nm) and Ag (150 nm) films were deposited on the silicon substrates' reverse side to create ohmic connections. On the Au/Cr/SiO_2 substrate, a graphene layer was deposited. For samples prepared with several graphene layers, the wet transfer layer was employed to transfer each layer. For example, the process was repeated 4 times for transferring 4 graphene layers. This process is reliable and easier to achieve since the alignment was done through the area of the top widow part of samples. Novel techniques include annealing, chemical treatments and DUV are used to lessen the leftover residue. In order to increase the overall fill factor of devices, several graphene layers were used. 65% HNO_3 doping was used to further boost the devices capability. Where, graphene samples were exposed to the vapor of HNO_3. Lastly, PMMA was formed onto graphene, preventing dopants from evaporating and increasing device stability. This coated layer further improves the efficiency of devices. Graphene-based field effect transistors (GFETs) were also prepared to study the electrical properties of graphene layers transferred onto a 300nm SiO_2/Si substrate. Then, channels with a 720 □m length and an 80 □m width were formed. The channels were formed after the lithography and shaping procedures. To achieve this, a mask shown in Fig. A-1a (in appendix) is used within the lithograph. After that, a shaping procedure was applied by using the sputtering machine. The vacuum was set up to be under vacuum of 10-7 torr with 4 m Torr Argon gas and 50 Watt. The

sputtering procedure removes the unwanted graphene which was uncovered with the photoresist. After the lift-off procedure, graphene channels were created. Electrodes of 5 nm Cr/50 nm Au were created by sputtering.

4. A new method for producing graphene/silicon Schottky junction solar cells using sputtering

4.1 Introduction

An extensive review of graphene/Si solar cells was provided in Chapter 2. As presented, the preparation process requires complex photolithography and etching of SiO_2 to form a top window on silicon wafers. In this chapter, a novel method using a sputtering process is introduced to simplify the preparation process of devices. By using this method, an SiO_2 top window and contacts are created, in place of a complex procedure that was used in previous works. Additionally, the sputtered thickness of SiO_2 needed should be investigated to obtain high efficiency for devices. Additionally, 2 nm of native oxide is formed onto Si substrates when they were left in ambient conditions for 2 h [164]. This led to the removal of dangling bonds and eliminated recombination at the graphene/Si interface. To reduce the PMMA residue, annealing and DUV techniques were incorporated in this chapter. The results of the tests on the prepared devices showed major improvement when annealing and DUV techniques were used. An extra doping process was also done to further enhance the solar cell efficiency. In order to acquire doped devices with lasting stability, a PMMA layer was formed onto doped graphene to help impede the dissipation of dopants over a period of time.

4.2 An innovative method for synthesizing graphene/Si Schottky junction solar cells through sputtering

A sputtering procedure was used to create a SiO_2 layer/Si substrate of top-window structured devices. This reduces the complexity of device fabrication reported in previous works. This coating was achieved after the necessary cleaning and lithography processing were carried as shown in Figs. 4.1a and 4.1b. Next, 80nm Au/5nm Cr layers were sputtered to form a contact on SiO_2, as presented in Figure 4.1c. After the coating process, samples were immersed in the Microposit remover 1165. Then, the ultrasonication was applied for 10 minutes to let the remover come into contact with the photoresist. This leads to removing the unwanted layers with their photoresist. Then, a layer of graphene was transferred to cover the area of the window

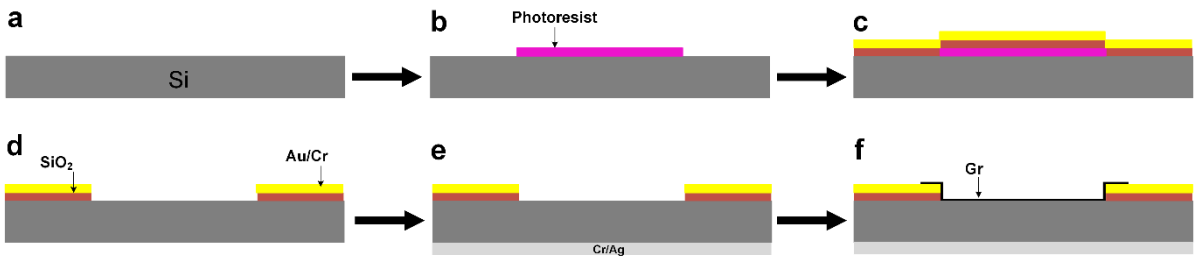

Figure 4- 1 Novel preparation of top-window structure. (a) and (b) After cleaning and applying conventional lithography to coat SI substrates with a 3.3 × 3.3 mm^2 area of photoresist. (c), (d), (e) and (f) Sputtering SiO_2 with contacts and transferring graphene.

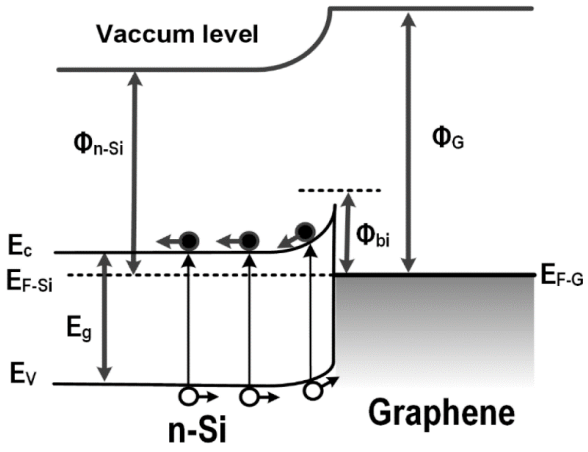

Figure 4- 2 A producer diagram of a graphene/Si Schottky junction solar cell shows how a photogeneration process works.

(about 9 mm^2), see Figure 4.1e. Where the optimal length and width of the graphene layer that was used in solar cells were the same (3 mm). After that, 150 nm Ag/5nm Cr layers were sputtered onto the backside of Si samples, forming the Ohmic contact, as displayed in Figure 4.1f. Figure A-3 (in the appendix) shows an SEM image of the topography of graphene/Si Schottky solar cells and EDS spectra of Au/ SiO2/Si and graphene/native oxide/Si layers for prepared devices. As observed, devices were successfully prepared by the novel fabrication process. According to Fig. 4.2, the graphene-silicon contact is where the Schottky junction forms in this arrangement. The incident light causes carriers to be produced everywhere along the thickness of the Si wafer. After that, the photocurrent is produced as carriers flow in opposing directions by the built-in field [35, 36]. Raman and optical techniques were employed to examine the prepared graphene layers' monolayer nature and quality.

4.2.1 Advanced graphene/Si Schottky junction solar cells based on the sputtering process

Graphene placed onto the SiO_2/Si substrate exhibits 3 bands primarily in its Raman spectra, as seen in Fig. 4.3. The strength of the 2D band, which is the highest peak at 2697 cm^{-1}, is about double that of the G band, which is the second peak at 1602 cm^{-1} in the spectrum. This data shows the graphene layer is a high-quality monolayer. Moreover, it can be seen that there is a small band of D in the spectrum, which suggests that defects are in the graphene [99, 100]. Figure 4.4 illustrates the (*J-V*) features of fabricated graphene/n-Si Schottky junction solar cells. Fig. 4.4a shows *J-V* features of samples prepared with a 250 nm SiO_2

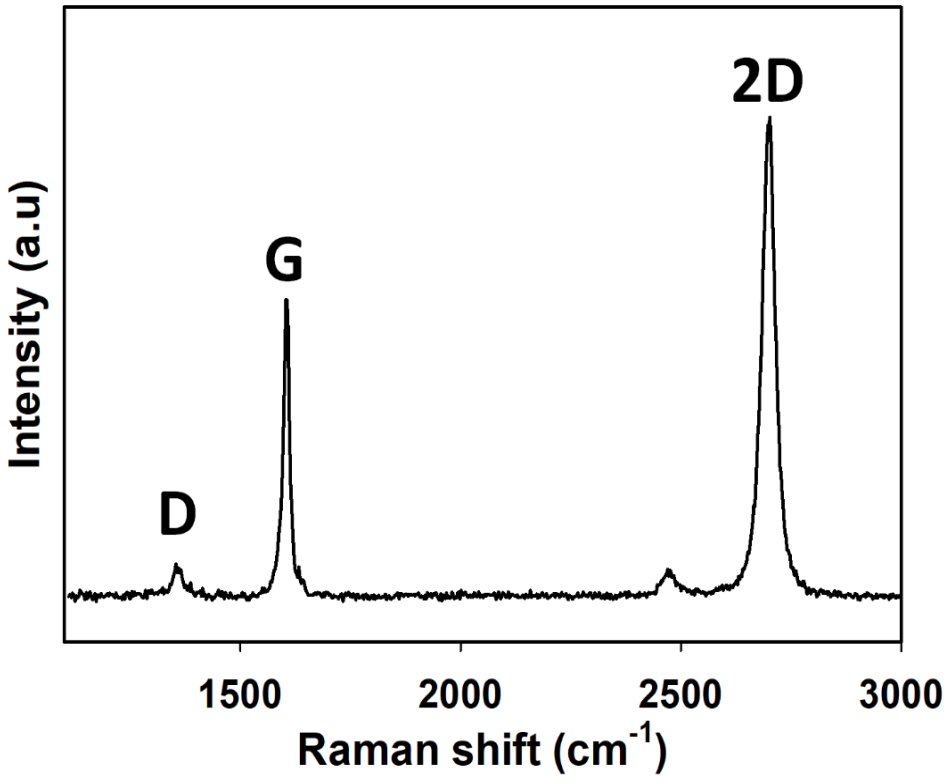

Figure 4- 3 Spectrum of transferred-CVD graphene.

window and 200 □m thickness of Si substrates. The (J_{SC}), (V_{OC}), (*FF*), and power (*PCE*) of this device were respectively 8.12 mA/cm^2, 0.307 V, 21%, and 0.52%

before it was stored (blue curve). The effect of storage was investigated for 11 days for devices. After being left for 11 days, the corresponding factors of this device were 9.7 mA/cm^2, 0.315 V, 21.3%, and 0.65%, respectively. The graph for this stored device is shown in red. The natural doping acquired from the air was responsible for the rise in factors after storage [126, 141]. Furthermore, devices were prepared by using different thicknesses of Si substrates as illustrated in Figure 4.4b. It can be observed that a device with a thinner substrate displayed better performance than one with a thicker substrate. The device's parameters with the thicker substrate were 6.6 mA/cm^2, 0.275

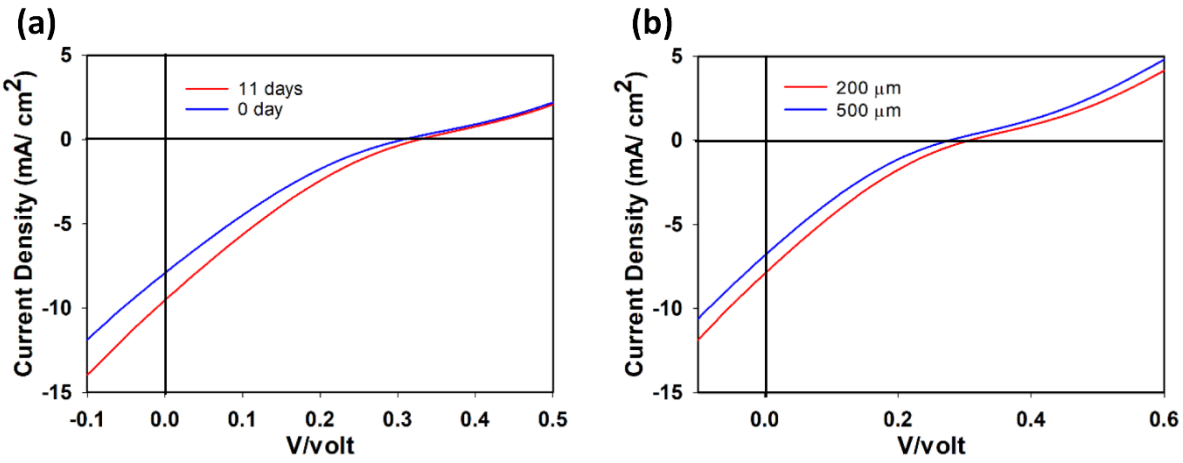

Figure 4- 4 (a) *J-V* features of graphene/Si Schottky devices made utilizing top-window created by sputtering before and after storage in air for 11 days. (b) *J-V* features of graphene/Si Schottky devices constructed with varied Si wafer thicknesses.

V, 20 % and 0.35%, respectively. The reason behind this decrease in factors of devices prepared with thick substrates is that the carriers will follow a longer path toward the cathode, which creates a great possibility for the recombining process. Hence, for achieving high-performance devices, Si substrates with 200 □m thickness is used for preparation. The thickness of a sputtered SiO_2 layer as a top window was scientifically explored for graphene/Si Schottky junction solar cells. The progression of photovoltaic variables is shown in Figures 4.5 and A-4

(in the appendix) for devices that have been built with varying thicknesses of the SiO_2. Figure 4.5a demonstrates that when the thickness of the SiO_2 layer was raised from 50 to 250 nm, both the V_{OC} and the J_{SC} rose noticeably. As indicated in Fig. A-4, there are unideal curves for samples coated with SiO_2 layers with a thickness less than 250 nm. The V_{OC} climbed from 0.2 to 0.307 V, and the J_{SC} increased from 4 to 8.12 mA/cm^2, respectively. In addition, the *FF* and *PCE* increased their performance, moving from 18.7 to 21% and from 0.15 to 0.52%, respectively. It is also clear from this figure that variables of samples prepared with thicker SiO_2 than 250 nm were saturated. Based on these findings, the photovoltaic capabilities of the devices were greatly enhanced when a layer of SiO_2 with a thickness of 250 nm was formed.

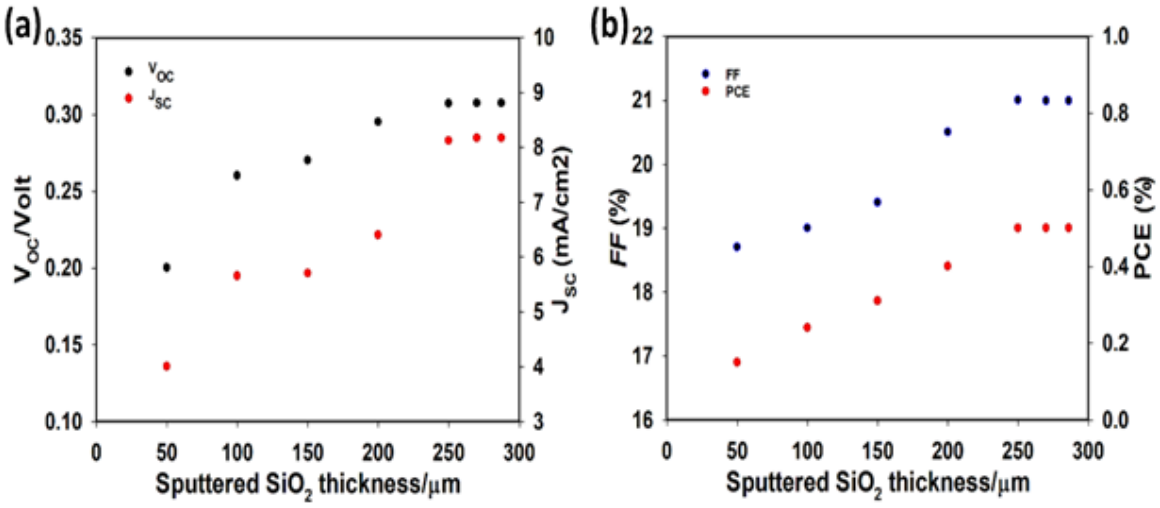

Figure 4- 5 (a) and (b) Advances of photovoltaic features of devices designed with different SiO_2 thicknesses.

Furthermore, it is conceivable to postulate that the flow of current that escapes via the interface of graphene and silicon diminished after applying 250 nm of SiO_2. Therefore, it can be indicated that this thickness is the optimal layer for creating the top-window structure.

4.2.2 Improved graphene/Si Schottky junction solar cells based on the sputtering and annealing processes

The annealing procedure in vacuum and forming gas is the next development for devices. Fig.4.6 presents data of solar cells annealed at 200 °C for 2h. The *J-V* characteristic (black curve) of a sample annealed in vacuum is shown in this figure, demonstrating that the thermal annealing method enhances the J_{SC} to 18.7 mA/cm^2. The V_{OC} of devices was the same of that in the previous process. The enhancement in the J_{SC} develops the *PCE* and *FF* to 1.2 and 21 %, respectively. This increase is attributed to the reduction of contaminants such as H_2O and O_2 caused by the wet

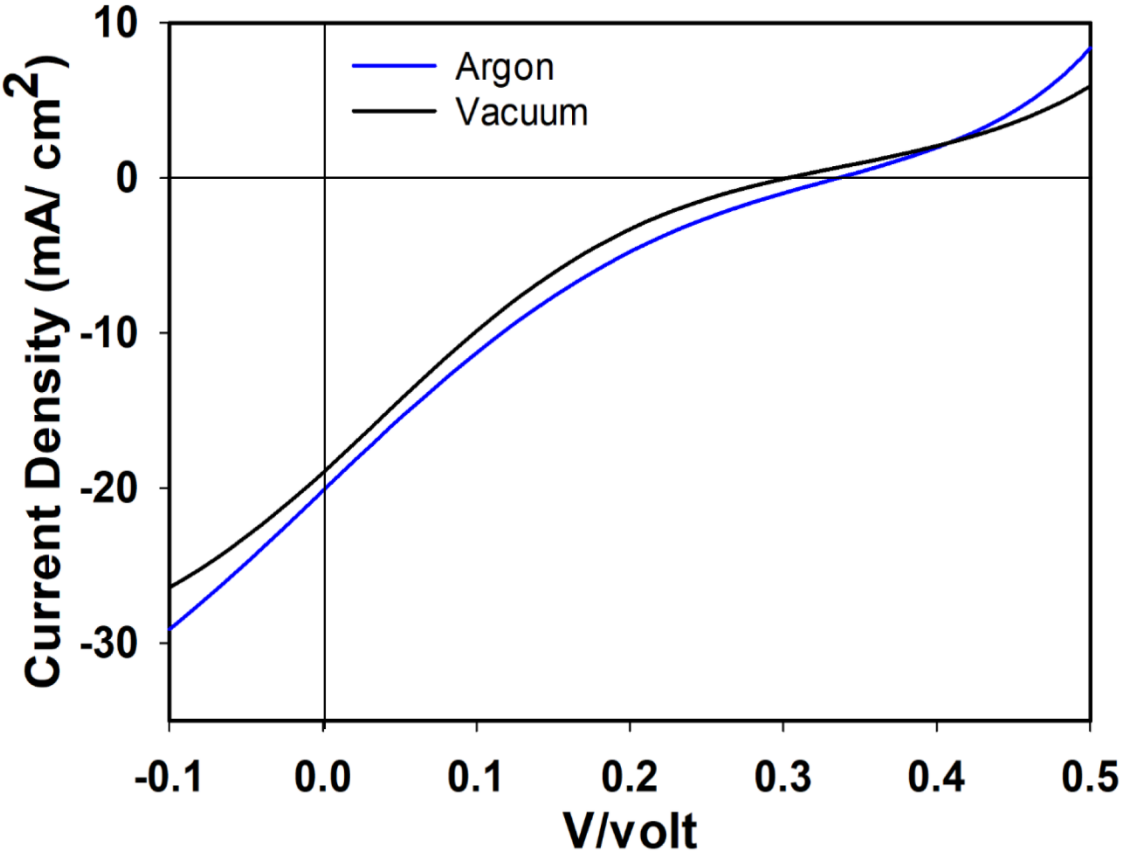

Figure 4- 6 J-V properties of devices annealed in a vacuum and forming gas for 2 hours at 200 °C.

transfer process at the graphene/silicon interface [166]. After annealing in forming gas, the *J-V* feature of samples was measured (see Fig. 4.6, the blue curve). It is clear that V_{OC} and J_{SC} were significantly enhanced, reaching 0.333 V and 19.9 mA/cm^2, respectively. Additionally, a discernible improvement was seen in the *FF*, which rose to 24%, and in the *PCE*, which rose to 1.6%. It can be noticed that the annealing process in both cases results in considerable improvements to parameters. It can also be observed that there is a significant improvement after using the forming gas.

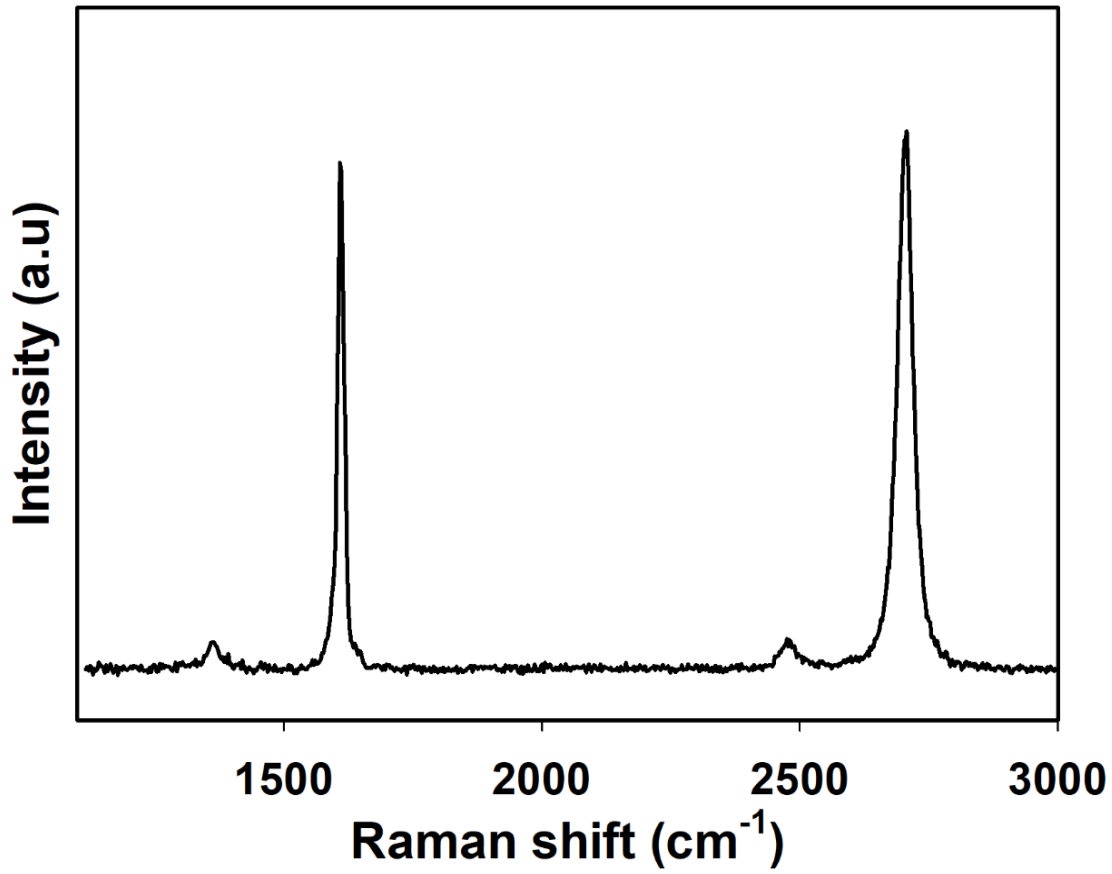

Figure 4- 7 Raman spectrum of graphene annealed in forming gas at 200 °C for 2 hours.

Raman tool was applied to get knowledge of the effect of annealing in forming gas on solar cells. Figure 4.7 illustrates the Raman spectrum of graphene that was transferred after the annealing. The findings of a Raman study reveal that

the locations of the G band are at 1607 cm^{-1}, and the 2D band is at 2699 cm^{-1} for annealed samples, whereas the peaks are placed at 1602 and 2697 cm^{-1} for unannealed samples. This indicates that there is a difference in the positions of peaks of Raman spectra before and after annealing in forming gas. After annealing in forming gas, the Raman spectrum shifts toward the blue, which is evidence of the p-doping in graphene. Because of this p-doping, the performance of the device significantly improved. Although annealing led to an important improvement in the *PCE*, the *J-V* lines of samples that were prepared still have the s-shaped. Therefore, one conclusion that can be reached is that the s-shape is a consequence of the PMMA residue acquired during the wet transfer procedure. This residue might be one of the possible outcomes and is a conclusion that is supported in other studies [126, 141]. Hence, the DUV of 254 nm at 180 ^{o}C was applied to break the chemical bonds of PMMA. Acetone was then applied to strip off the

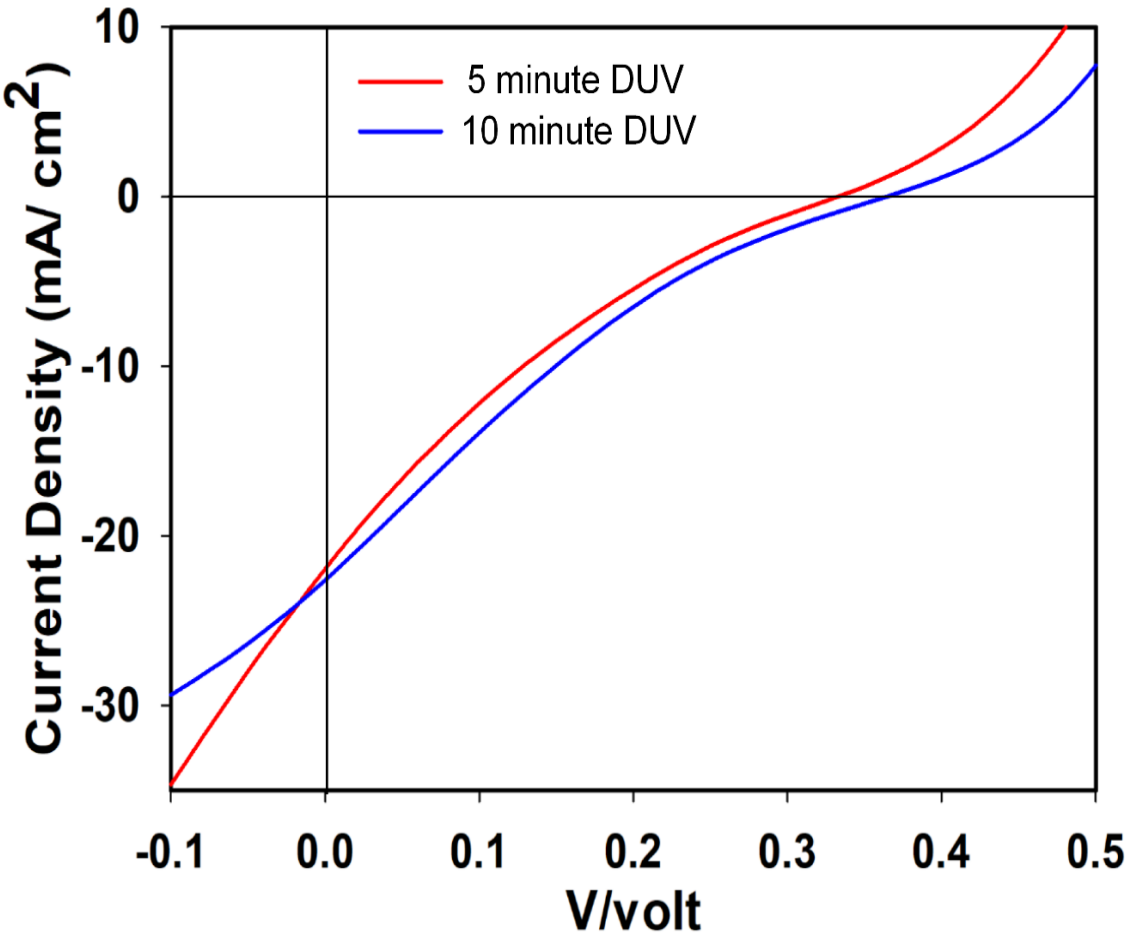

Figure 4- 8 J-V features of solar cells exposed to DUV light before being heated in forming gas at 200 ^{o}C for 2 hours.

PMMA layer. Following this, annealing in forming gas was applied to samples at 200 ^{o}C for 2 hours. Samples were first subjected to the DUV for 5 and 10 minutes before annealing. The *J-V* features of solar cells in these cases are illustrated in Figure 4.8. It can be shown that the sample that was subjected to 5 minutes DUV had the V_{OC} of 0.34 V and J_{SC} of 21.7 mA/cm^2. The *FF* and the *PCE* were refined to 26% and 1.9%, respectively. The V_{OC} and J_{SC} of the sample, which were exposed for 10 min, reached 0.35 V and 22.3 mA/cm^2, respectively, and the *FF* and *PCE* values increased to 27 and 2.1%, respectively. This demonstrates that samples exposed to the (DUV) for a longer duration exhibited significantly more improvement than those exposed to a shorter duration. It was also found that

exposing samples for longer than 10 min results in negligible improvement. Hence, 10 min exposure time is optimum for reducing the residue in the

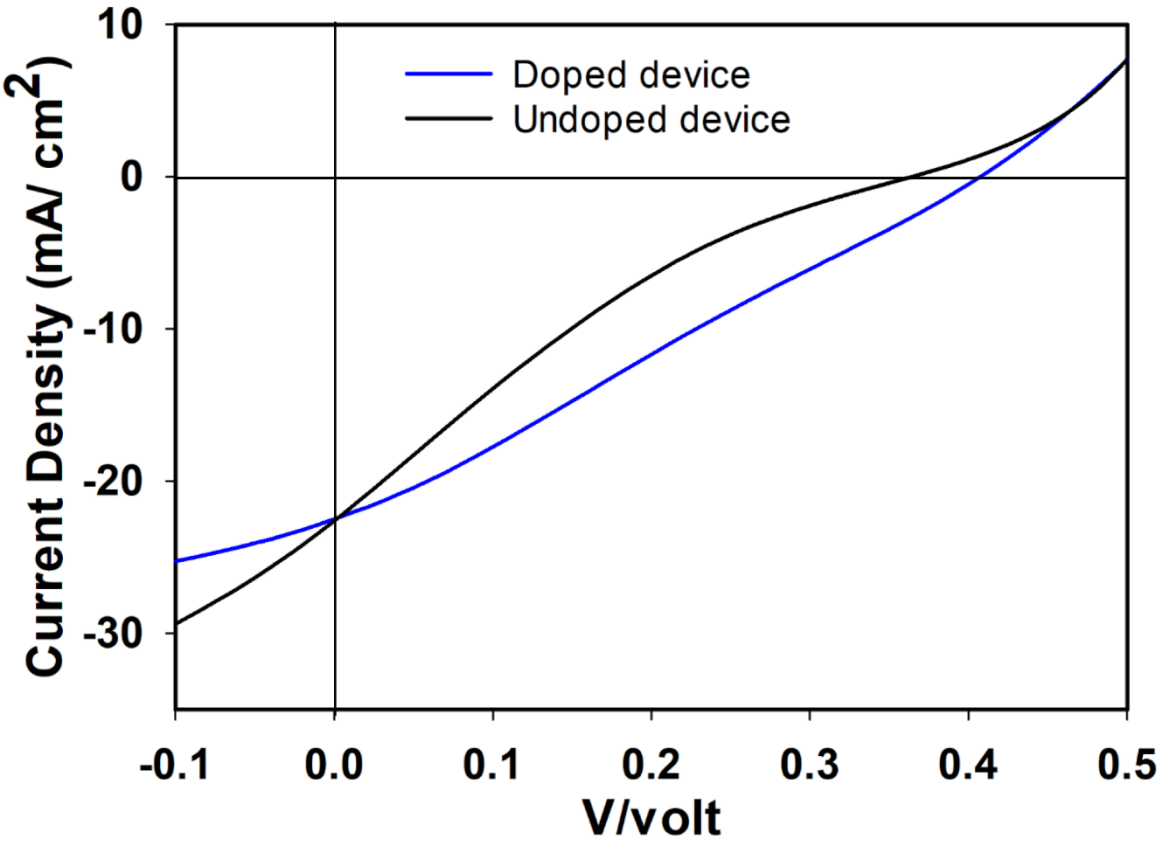

Figure 4- 9 J-V features of doped and undoped solar cells.

case of usage 46 mg/ml PMMA concentration. The vapour of HNO_3 was also applied for 90 seconds to boost the performance of the previous device, leading to further p-doping in graphene. Figure 4.9 illustrates the *J-V* curves of doped graphene/Si Schottky junction solar cells (blue curve). The doped device has demonstrated improvements in its (V_{OC}), (J_{SC}), (FF), and (PCE), reaching 0.4 V, 22.5 mA/cm^2, 39, and 3.5% respectively. This discovery indicates a direct positive impact of HNO_3 on the photovoltaic parameters. Moreover, the *J-V* curve of doped samples exhibits a reduced S-shape compared to undoped samples. Hence, the preparation process of samples requires additional improvement to completely disregard the s-shape, ensuing better performance of devices.

4.3 An innovative method for fabricating graphene/Si Schottky junction solar cells using a combination technique

In this section, the natural native oxide was applied to the Si samples by exposing them for two hours in ambient conditions. This eliminates the recombination process due to dangling bonds onto Si substrates. In addition, the combination method (annealing and DUV) was further improved by efficiently eliminating the residue. In the improved method, coated PMMA/graphene samples were put through the DUV treatment for 10 minutes. After that, acetone was managed to withdraw the PMMA layer. Then, devices were annealed in forming gas for 3 hours. Graphene samples that had been prepared for this section were evaluated using the Raman and XPS techniques to assess their quality and to detect any PMMA that was left behind. Fig. 4.10 shows Raman data from graphene samples before and after the combination process. The 2D and G bands in the red spectrum are at 2697 cm^{-1} and 1602 cm^{-1}, respectively, for samples treated only with acetone. This spectrum has an intensity ratio of around 1.7, acetone. In this

case, the ratio of the intensity was about 1. measured as I_{2D}/I_G. This figure also shows a tiny band of D at 1356 cm^{-1}. A shift in the spectrum (the blue line)

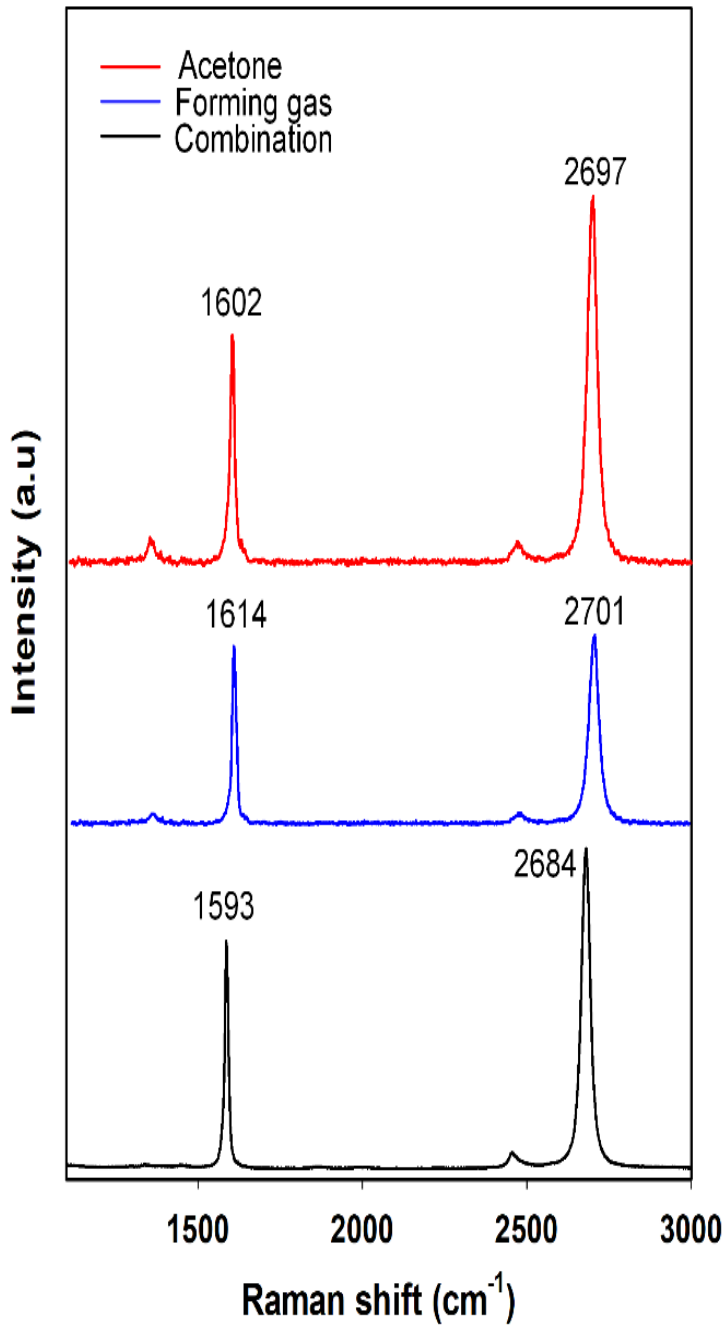

Figure 4- 10 Raman spectra of graphene transferred with several techniques.

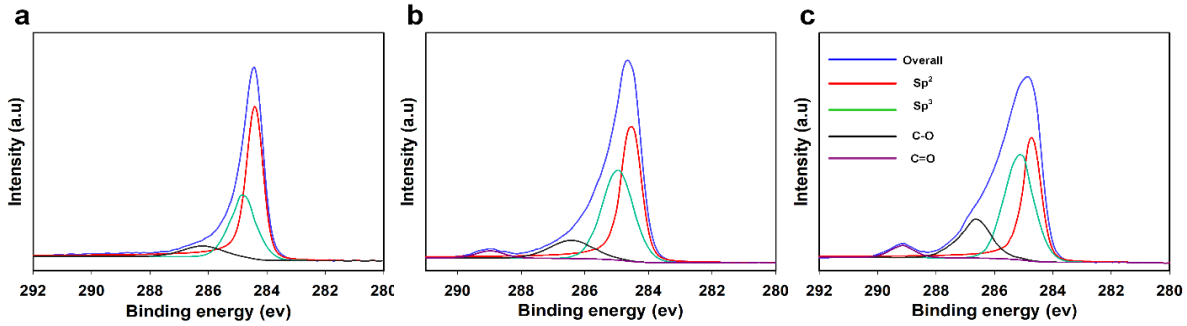

Figure 4- 11 XPS data of transferred graphene sheet using (a) a combination technique, (b) forming gas and (c) acetone treatment. The blue curve shows the overall spectra, the red spectra exhibit graphene, and the other spectra show the PMMA residue.

was achieved after applying the annealing in forming gas for three hours, compared to the samples controlled using without annealing. The black spectrum is for samples processed with the combination process. Proof that the quantity of PMMA residue has been reduced is provided in the form of a red shift in this spectrum compared with previous spectra. In addition, the intensity ratio rises after the combination operation compared to those of the samples that were annealed earlier, thus demonstrating that the quality of the graphene samples has increased. The XPS analysis, which can be shown in Figure 4.11, shows that there was a significant decrease in the amount of residue. After reducing the residue using the combination approach, the graphene-specific sp^2 component, shown by the red curve, is seen to rise, in contrast to the behaviour of other components belonging to the residue of PMMA. The *J-V* features of samples processed with and without the combination procedure are depicted in Figure 4.12. The *FF*, *PCE*, V_{OC}, and J_{SC} values for the device treated with acetone are as follows: 23%, 1.4%, 0.41 V, and 14.7 mA/cm^2. The data of the V_{OC}, J_{SC}, *FF*, and *PCE* of a device formed using forming gas were as follows: 25 mA/cm^2, 0.413 V, 28%, and 2.9%, respectively. Compared to other devices, those treated using the combination technique exhibit a noteworthy improvement. The findings from

the final device were as follows: the J_{SC} registered 26.9 mA/cm^2, the V_{OC} registered 0.4 V, the *FF* registered 37%, and the *PCE* registered 4%. The development achieved by reducing the residue can be stated to have been acquired. It should also be pointed out that the ideal *J-V* curve that was generated by treating samples using the combination approach shows a significant improvement in the performance of samples, comparing to those obtained by processing samples without the combination procedure. The data that were obtained provide more evidence that the s-shaped defect is brought on by PMMA residue, which in turn brings about a decline in the

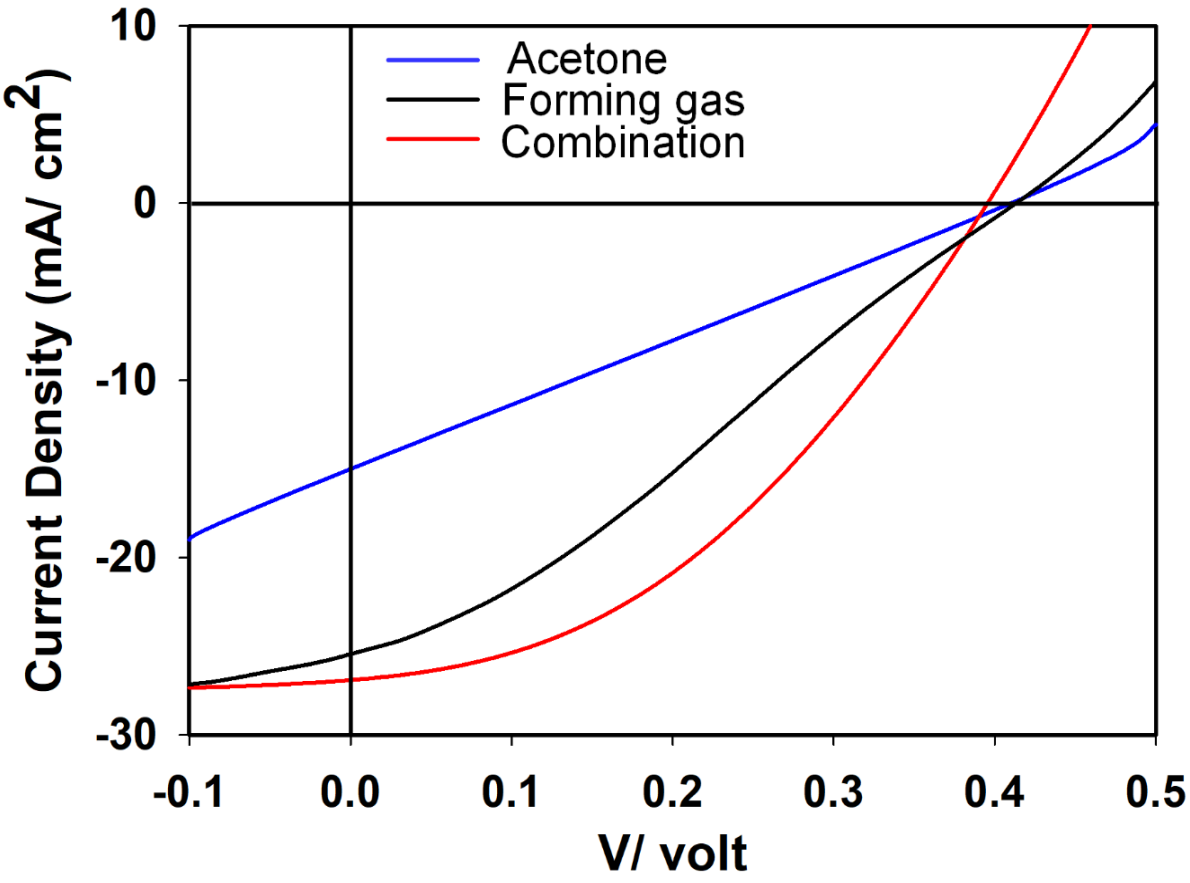

Figure 4- 12 J-V properties of photovoltaic cells produced with and without a combining method.

efficiency of solar cell devices. It has also been shown that forming gas that includes 90% argon and 10% hydrogen without using the DUV is not adequate to remove the residue. This conclusion aligns with observations from past works [44, 128, 167-169]. Similarly, it has been established that the residue of PMMA causes an increase in the recombination process of carriers at an interface of graphene/Si samples, which results in an unfavourable s-shape in the *J-V* graph and poor performance of devices [170, 171]. For extra deployments, multi-graphene layers (MGL) were included in devices to enhance their fill factors. During this preparation process, the combination technique was achieved after the transfer of each graphene layer. This was done to ensure that the graphene layers would be completely devoid of residue.

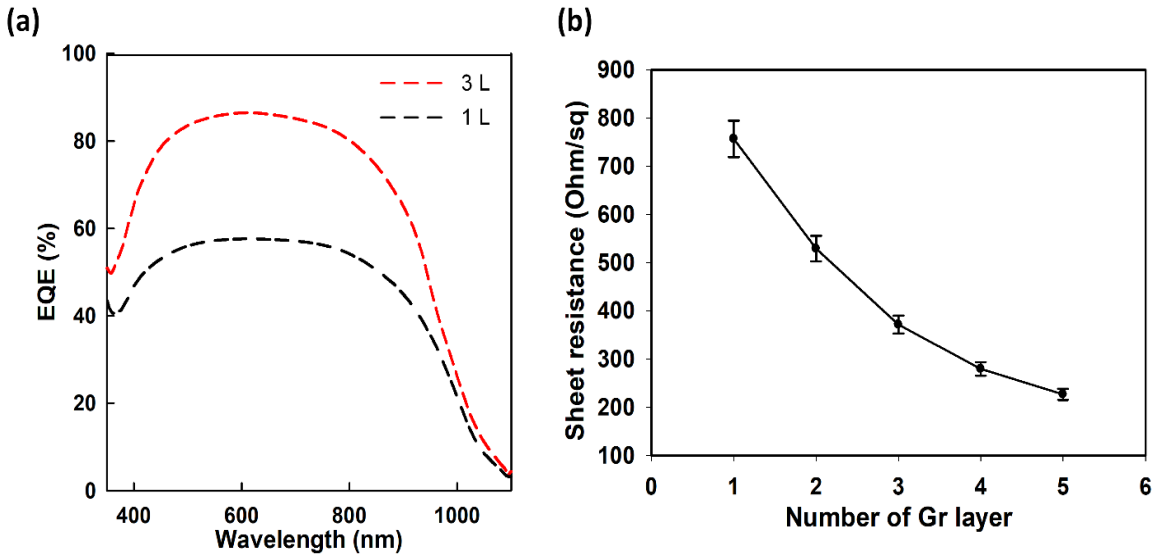

Figure 4- 13 (a) Curves showing EQE of solar cells constructed using a single layer and three layers. (b) Established sheet resistivity of multi-graphene layers.

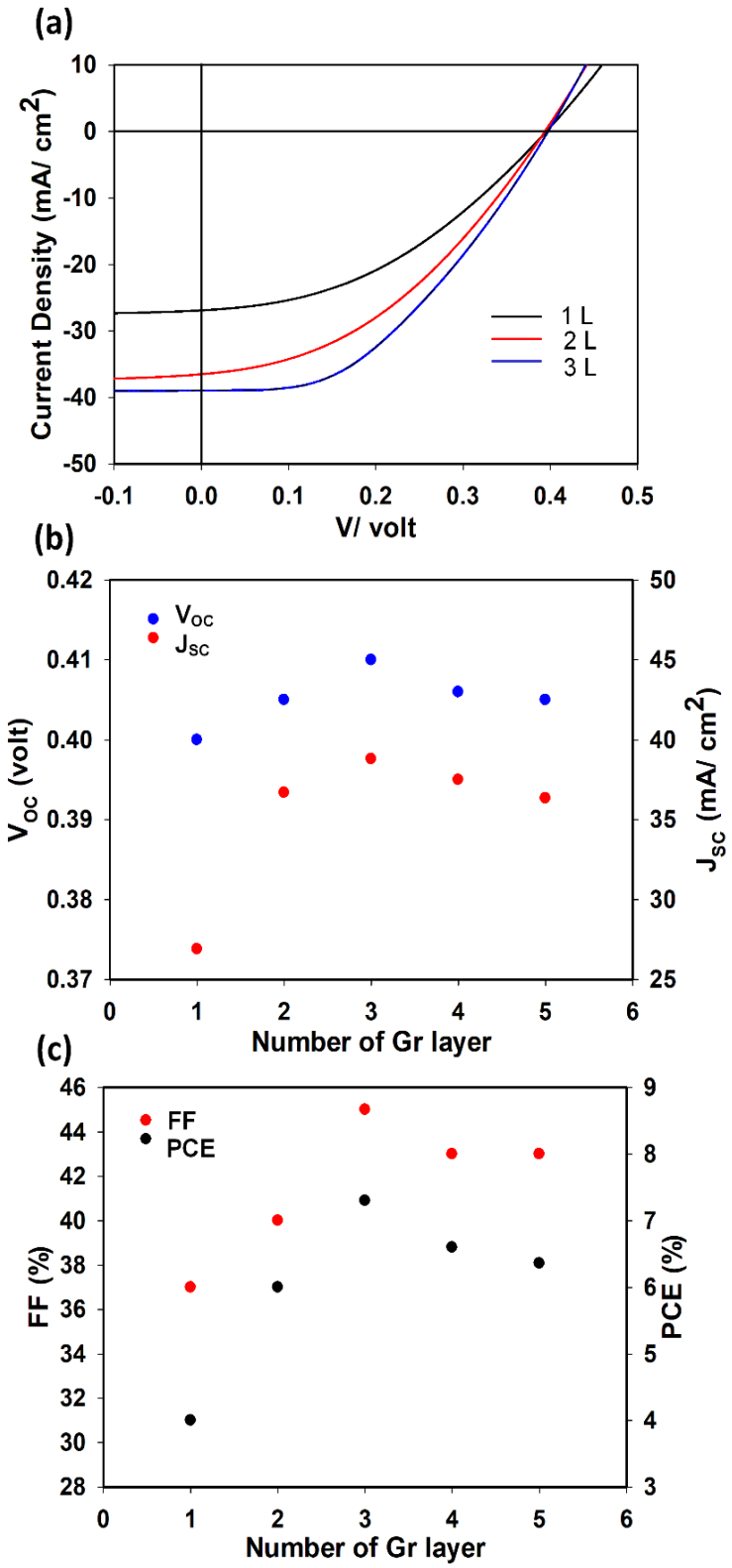

Figure 4- 14 (a), (b) and (c) and *J-V* graphs and development features of solar cells constructed with graphene layers.

The *J-V* features of the MGL/Si solar devices are displayed in Fig. 4.13a and A-5 (in the appendix). It has been shown that samples made with three graphene

layers display a substantial advance compared to those produced by other types of devices. This device's photovoltaic factors grew to 0.415 V, 38.8 mA/cm^2, 7.3%, and 45 % accordingly. From this, it can be deduced that the *FF* and *PCE* developed by approximately 30% and 85%, respectively after introducing 3 graphene layers. The *PCE* of 7.3% is a pristine record for samples made without the anti-reflection coating, doping, and texturing method that has been reported to date as a fact [125, 129, 133, 172]. Moreover, it emphasizes the significant reduction of the residue results in an important improvement in the efficiency of MGL/Si cells. Figures 4.13b, 4.13c and A-5show improved parameters for MG-samples processed with higher than three graphene layers. Nevertheless, the parameters were reduced for samples prepared with 4 and 5 graphene layers. This is because the optical transparency lessening with the encouraging number of layers, as seen by a decline in the photovoltaic factors for samples treated with more than three layers of graphene [173]. It seems from this that the optimal number of layers for increasing the efficiency of devices is three. The EQE measurements show that the performance of the device drastically improves once three layers of graphene are introduced, in contrast to prior samples that were produced with just one layer of graphene (see Fig. 4.14a). The EQE findings corroborate those from the *J-V* features, which is encouraging. Values of sheet resistivity of graphene are shown in Fig. 4.14b. These results demonstrate that the sheet resistivity of samples declines as the number of transferred layers grows to a minimum. As observed, the maximum feasible efficiency for the samples was achieved when the sheet resistivity of three layers was decreased to approximately half that of a single transferred layer. In addition, the doping strategy using HNO_3 was executed for 90 seconds to further

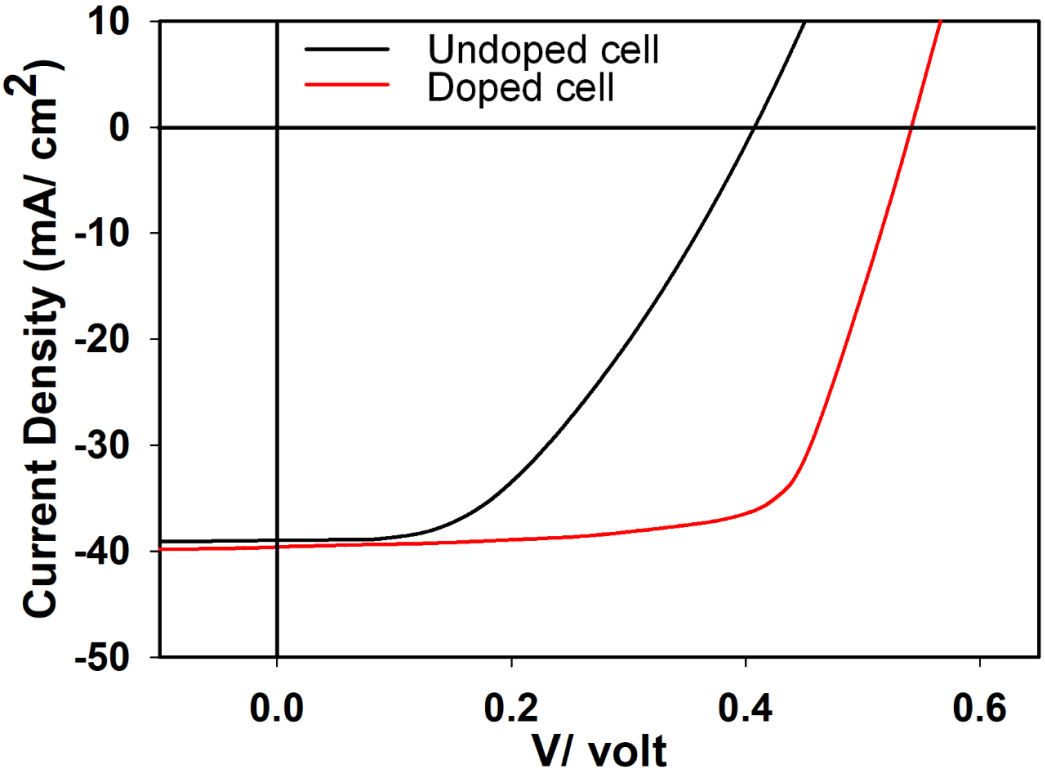

Figure 4- 15 Before and after the doping procedure, characteristics of *J-V* were produced using three graphene layers.

advance device performance, as Figure 4.15 shows the doped device's *J-V* line. In contrast to the curves obtained from undoped samples, the performance of doped samples was greatly superior. After the doping, the V_{OC} and J_{SC} evolved to the values of 0.54 V and 39.6 mA/cm^2, respectively. Moreover, the *FF* and *PCE* increased, reaching 69% and 14.4%, respectively. The increase in graphene's conductivity due to doping is responsible for this development [145, 174]. Even though the high *PCE* was produced following the doping method, it decreased with time because the used dopants evaporated [140, 175]. In order to mitigate and develop cell stability, doped devices were given a coating of PMMA, as illustrated in Figure 4.16a. Due to this, the evaporation of dopants will be prevented during the period.

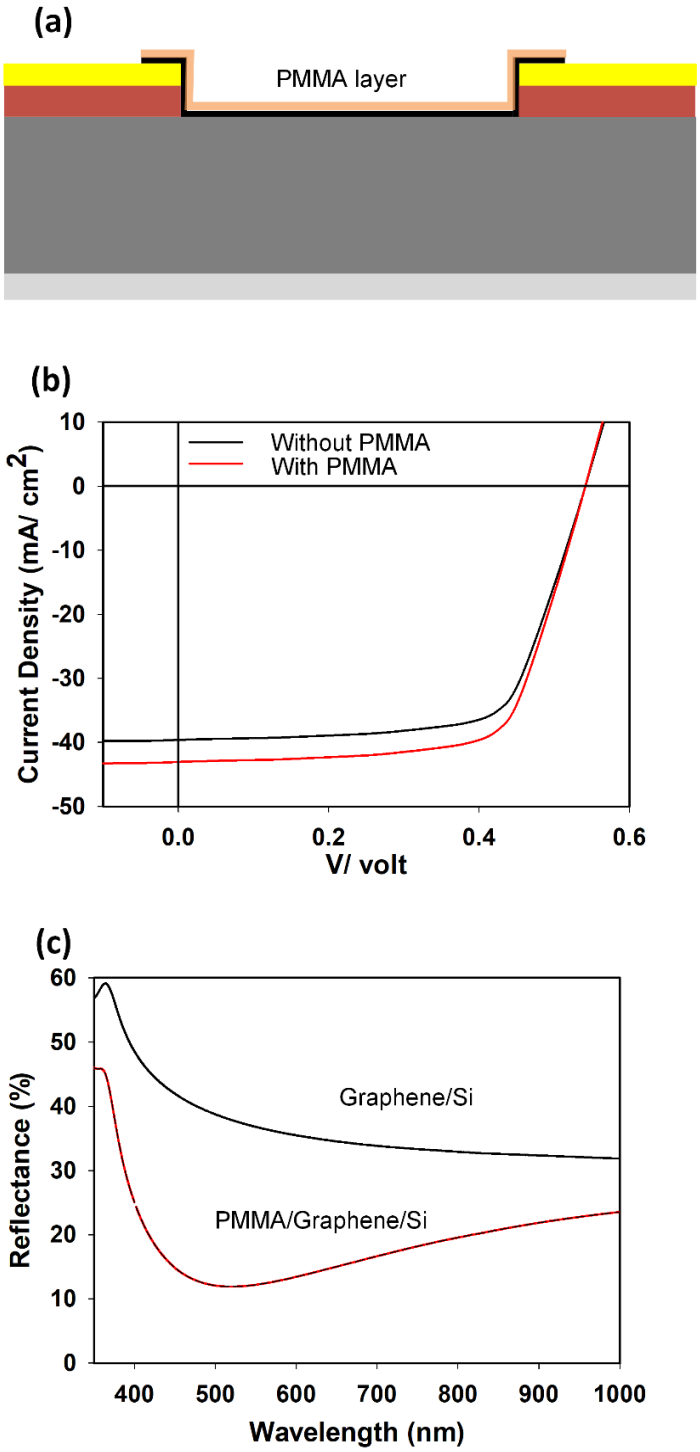

Figure 4- 16 (a) Diagram of a PMMA-coated MGL/Si Schottky junction solar cell. (b) *J-V* curves for MGL/Si Schottky junction solar cells with and without a PMMA layer. (c) Reflection spectra of graphene/Si and PMMA/graphene/Si substrates, demonstrating that after covering devices with the PMMA layer, indicating the reflection on the substrate is reduced.

Additionally, the coated PMMA layer reduces the amount of light that is reflected off (see Fig. 4.16c). The *J-V* features of coated samples following doping are displayed in Fig. 4.16b. The parameters of PMMA coated samples were as

follows: 42.8 mA/cm^2, 0.53 V, 75%, and 17%, respectively. This indicates that the J_{SC} had improved, rising from 39.6 to 42.7 mA/cm^2 as associated with the device's performance before coating. It can be seen that the gained *PCE* of 17% represents the greatest practicable degree of efficiency, and this shows that the coated-PMMA layer illustrated in Figure 4.16c can minimize the reflection that is induced by Si wafers. In comparison to the stated works [125, 126, 129, 133, 164, 172, 176], the current *PCE* and *FF* in this work are the highest values reported so far. Table 4-1 also shows the highest *PCE* in previous works. As observed, devices based on the top window produced 8.6% after applying doping and antireflection coating [128]. The *PCE* obtained from devices formed with a larger active area was 10% as the larger area produces higher efficiency [125]. Furthermore, back-contacted devices were utilized to expand the active area. The same area of graphene was employed to form the junction of devices, resulting in an efficiency of approximately 14%. [126]. Additionally, top window devices were treated with native oxide, doping and ARC procedures and showed 15.6%. It can also be noticed from this table that devices prepared in this work show the highest efficiency compared with others. This development is owing to multigraphene layers that were applied after the effective effecting cleaning procedure of the graphene surface. Consequently, coated and un-coated samples were exposed to air for 14 days. After storage, 15.9% was the *PCE* for the covered devices, which shows that the device kept 95% of its promotion effort being coated. In contrast, the *PCE* of uncoated devices was 10%, which indicates samples reserved 70% of their original functionality. This reveals that doped devices in this work demonstrated the highest degree of stability when compared with devices doped with HNO_3 in the previous works [76, 92]. Therefore, adding the layer of PMMA is one of the most critical phases in constructing stable and

efficient doped graphene/Si Schottky junction solar cells. Besides, the reflection of Si samples is decreased by this layer.

Table 4- 1 Comparative analysis of reported solar cells that have the highest *PCE*s.

Applied procedures	*PCE* (%)	Year	References
doping and antireflection coating (ARC) for top window	8.6	2012	[128]
Directly grown graphene and doping for top grid with	10	2015	[125]
the texturing process and doping for back contact	14.1	2018	[126]
native oxide, doping and ARC for top window	15.6	2015	[164]
Top window with MGL, doping and ARC	17		This work

4.4 Conclusion

This chapter presents a sputtering process that is a straightforward and economical method of fabricating graphene/n-Si Schottky junction solar cells. This method, coupled with the more traditional lithography, is used to circumvent the difficult etching procedure that SiO_2 requires. Additionally, the fill factor was efficiently improved by introducing native oxide onto Si samples and multi-graphene layers rather than monolayer graphene to obtain the Schottky junction for devices after reducing the PMMA residue, which significantly increased efficiency. After incorporating the doping procedure that HNO_3 performed, the performance of the devices grew even higher, which resulted in an increase of 14.4% in the *PCE*. After adding an encapsulated PMMA layer, the doped devices

similarly demonstrated remarkable performance, with a *PCE* of 17% and stability for two weeks.

5. Newly developed graphene/n-Si Schottky junction solar cells through chemical treatments

5.1 Introduction

Chapter 4 introduced the novel production process of graphene/Si Schottky junction solar cells using a sputtering process. In addition, the removal process of PMMA residue was achieved by the combination process of annealing and DUV steps. However, the vacuum is required for a few hours when the annealing step is applied. This step also requires crucial deliberations to evade an explosion due to H_2 in the gas mixture. To overcome this issue, this chapter presents two novel chemical treatments to eliminate the residue, in place of the combination method. The natural native oxide was also applied to Si wafers in order to achieve their process of passivation. Raman and X-ray photoelectron spectroscopies were conducted to evaluate the quality of transferred graphene layers. The *J-V* and EQE curves of prepared graphene/Si junction solar cells were measured before and after chemical treatments to explore the improvement in devices. In addition, the doping process and coated PMMA were employed to boost the performance of devices, ensuring great stability for a few months.

5.2 Formamide-treated novel graphene/n-Si Schottky junction solar cells

The steps involved in producing prepared graphene/Si solar cells are depicted in Fig. 5.1. In this section, solar cells made of graphene/silicon were dipped in a formamide solution. After the immersion process is completed, molecules of NH_2 derived from formamide are loaded onto the surface of the graphene. Analyses using Raman spectroscopy were done to examine the influence of the reduction on the unaltered graphene. The spectra in Figure 5.2a were obtained by

measuring them with a laser with a wavelength of 514 nm. In its purest form, the graphene has a typical Raman spectrum, which confirms its nature (see black line). For samples processed with acetone, the placements of the G band can be found at 1602 cm^{-1}, and the 2D band can be found at 2697 cm^{-1}. The obtained ratio (I_{2D}/I_G) is about 1.7. A small D band is associated with defects at 1356 cm^{-1} in the spectra. For samples processed with formamide, the G band was placed at 1597 cm^{-1}, while the 2D band was at 2693 cm^{-1}. This indicates there was a shift to the red in the spectra of graphene samples after samples have been dipped in formamide. The shift provided evidence that the amount of PMMA residue had decreased. The I_{2D}/I_G ratio was about 2 for proceeded samples in this case, indicating an improved quality of samples. Studies using X-ray photoelectron spectroscopy (XPS) were employed to further investigate the decrease

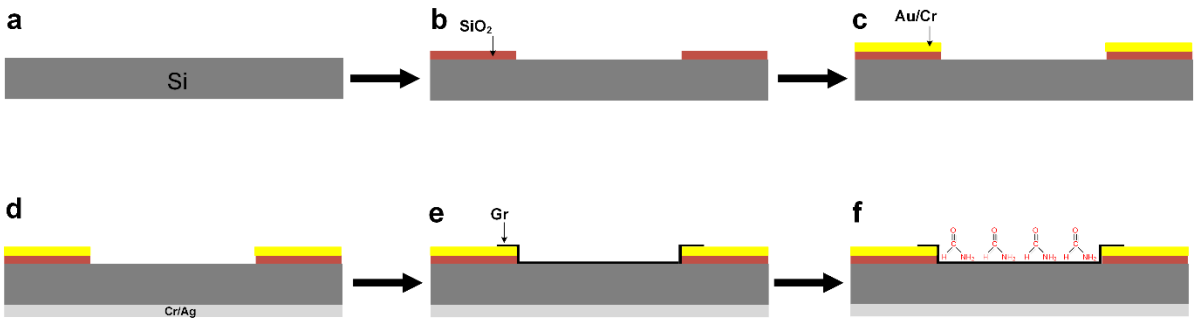

Figure 5- 1 An enhanced method for fabricating of graphene/Si Schottky junction solar cells with a top-window shape. (a), (b), (c), and (d) Cleaning the Si substrate, Forming SiO_2 and contacts. (e) Transferring a layer of graphene onto substrates. (f) Immersing sample in Formamide.

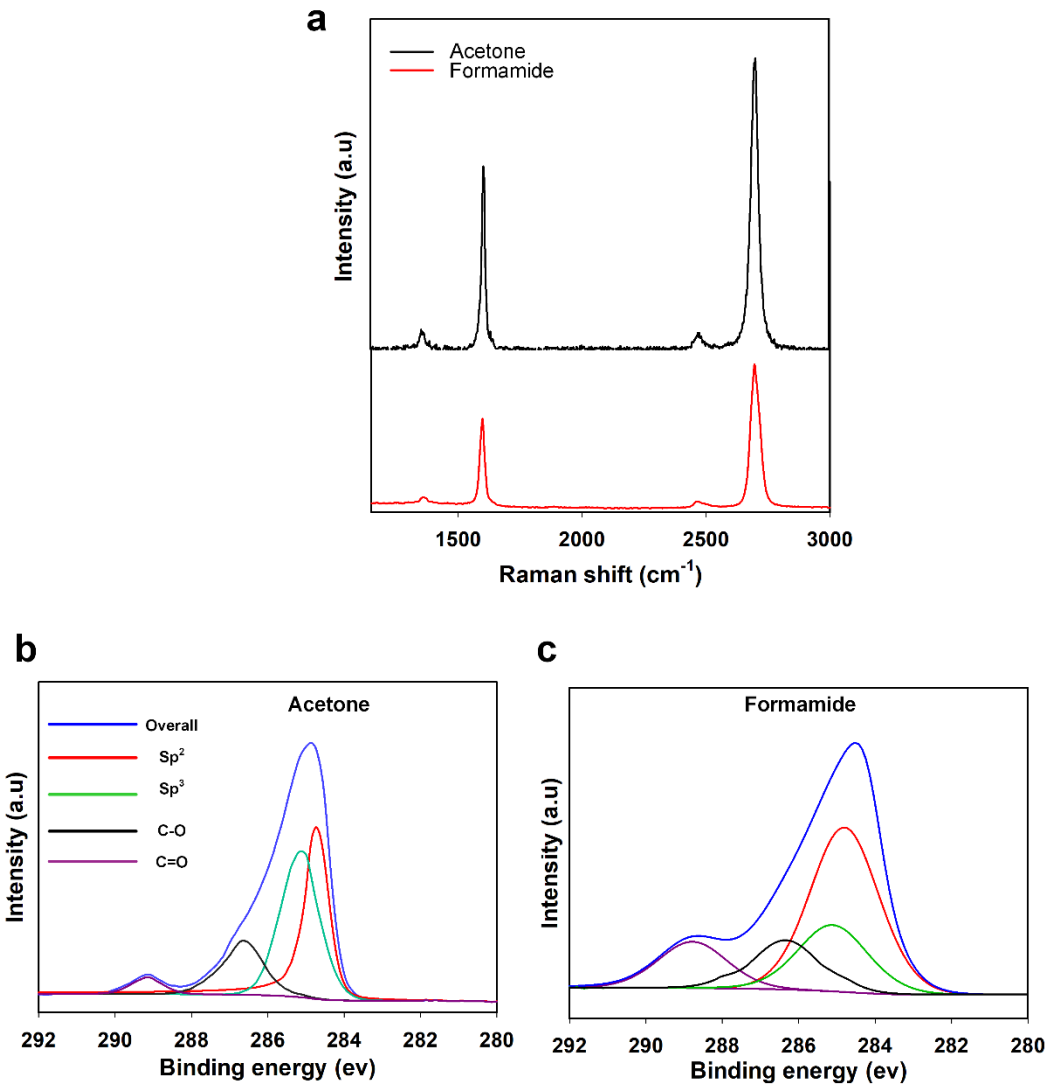

Figure 5- 2 Raman spectra (a) and XPS data (b and c) of graphene processed with acetone and formamide.

of the PMMA residue. Figures 5.2b and 5.2c present the XPS data of graphene before and after formamide. As can be seen in the illustration, the sp^2 part of graphene was enhanced after being submerged in formamide, associated to its natural state. In addition, the other components of the residue of PMMA, specifically sp^3, C-O, and C=O, exhibited a clear decrease following the treatments when these factors were compared with those of the natural state, which suggests that the chemical treatment effectively reduces the amount of

PMMA residue. Figure A-6 (in the Appendix) shows the optical images of graphene samples before and after minimizing the residue. As observed, chemical treatments provide a clean graphene surface compared with that before the treatment, dark spots refer to the residue on the graphene surface before the treatment. Measurements of solar cells' current density versus voltage (*J-V*) relationships are depicted in Fig. 5.3a before and after the dipping operation. For samples treated with acetone, the samples' power conversion efficiency (*PCE*), fill factor (*FF*), short-circuit current density (J_{SC}), and open circuit voltage (V_{OC}) are as follows: 1.41%, 23%, 14.72 mA/cm^2, and 0.415 V, respectively. A *PCE* of 3.13%, an *FF* of 43%, a J_{SC} of 21.23 mA/cm^2, and a V_{OC} of 0.342 V were found in the samples treated for 5.5 hours with formamide. This improvement demonstrates that removing the residue is the most important step in getting ideal *J-V* curves with exceptional factors in graphene/Si Schottky junction solar cells as described in the previous chapter. In addition, it demonstrates that the approach described, in which formamide is utilised,

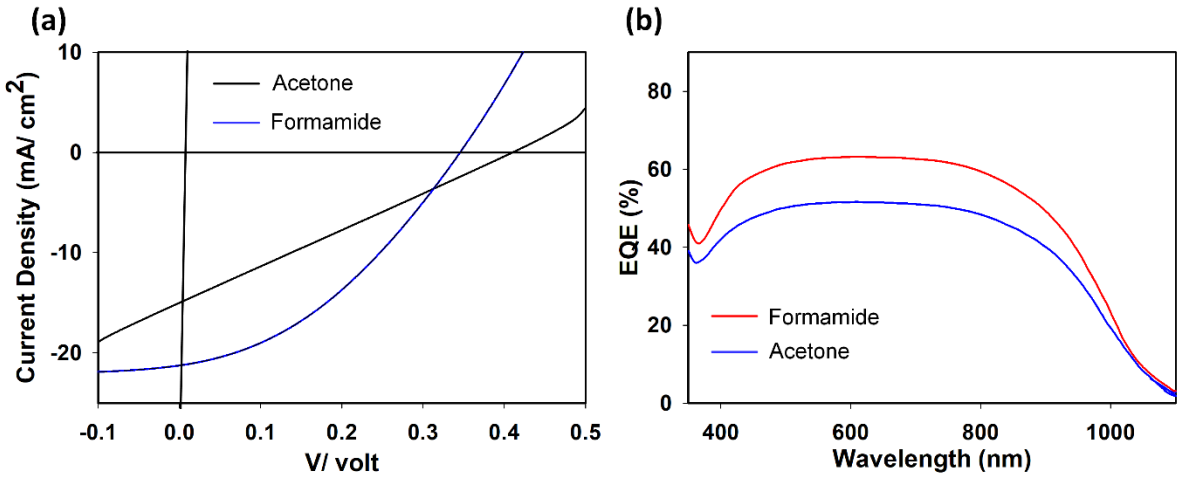

Figure 5- 3 (a) and (b) present the J-V characteristics and EQE spectra of graphene/Si Schottky solar cells before and after treatment with formamide, respectively.

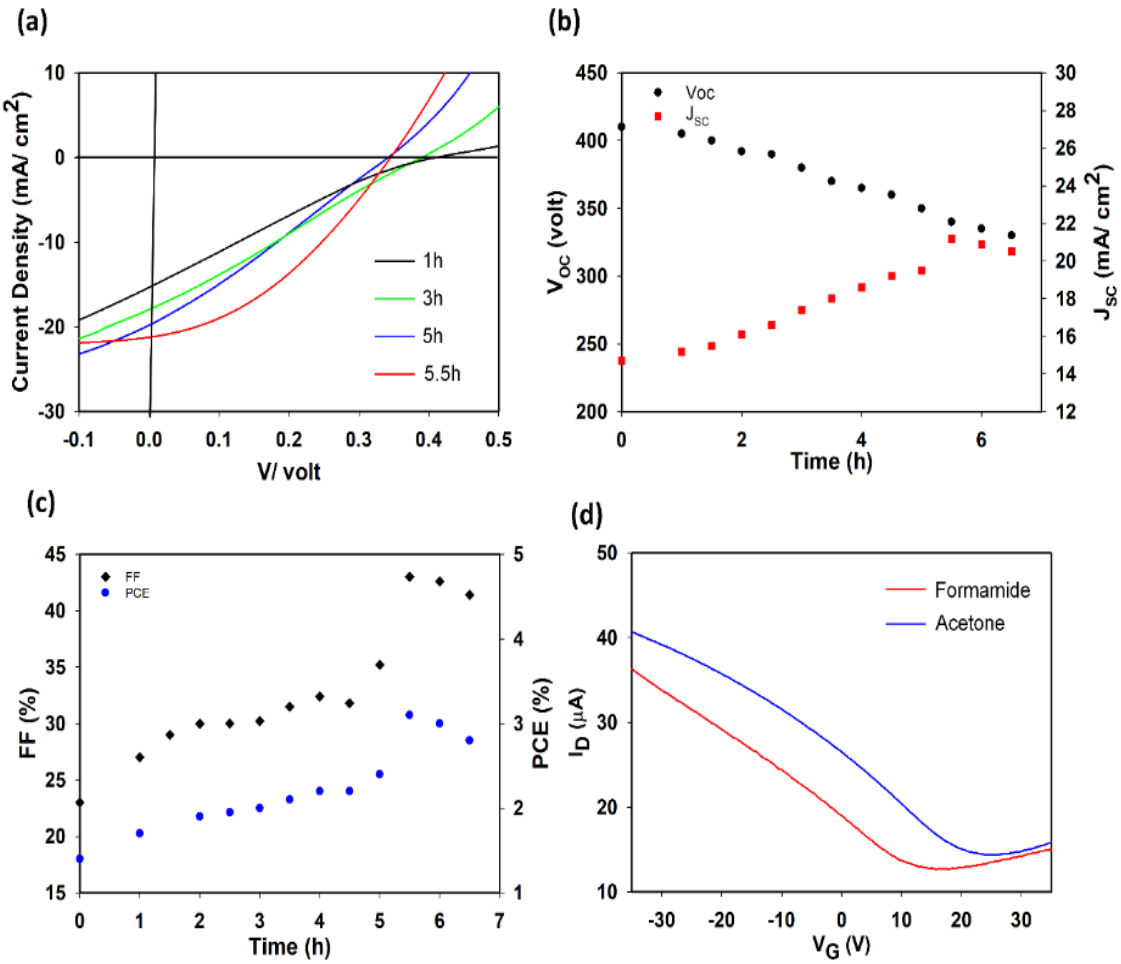

Figure 5- 4 (a), (b) and (c): *J-V* curves and improved factors of graphene/n-Si Schottky junction solar cells dipped in Formamide for different amounts of time. (d) (I_D-V_G) curves of GFETs in the air at room temperature and V_D = 0.1 V before and after chemical treatment.

is a less complicated and more productive method of eliminating the residue compared to the procedure that was utilized forming gas. The evaluation of samples using the EQE also confirms that applying the formamide method to the devices results in greater efficiency than that of devices processed without a formamide step (see Fig. 5.3b), which holds when compared to the results obtained from the *J-V* curves. In order to investigate how the formamide treatment affected the functioning

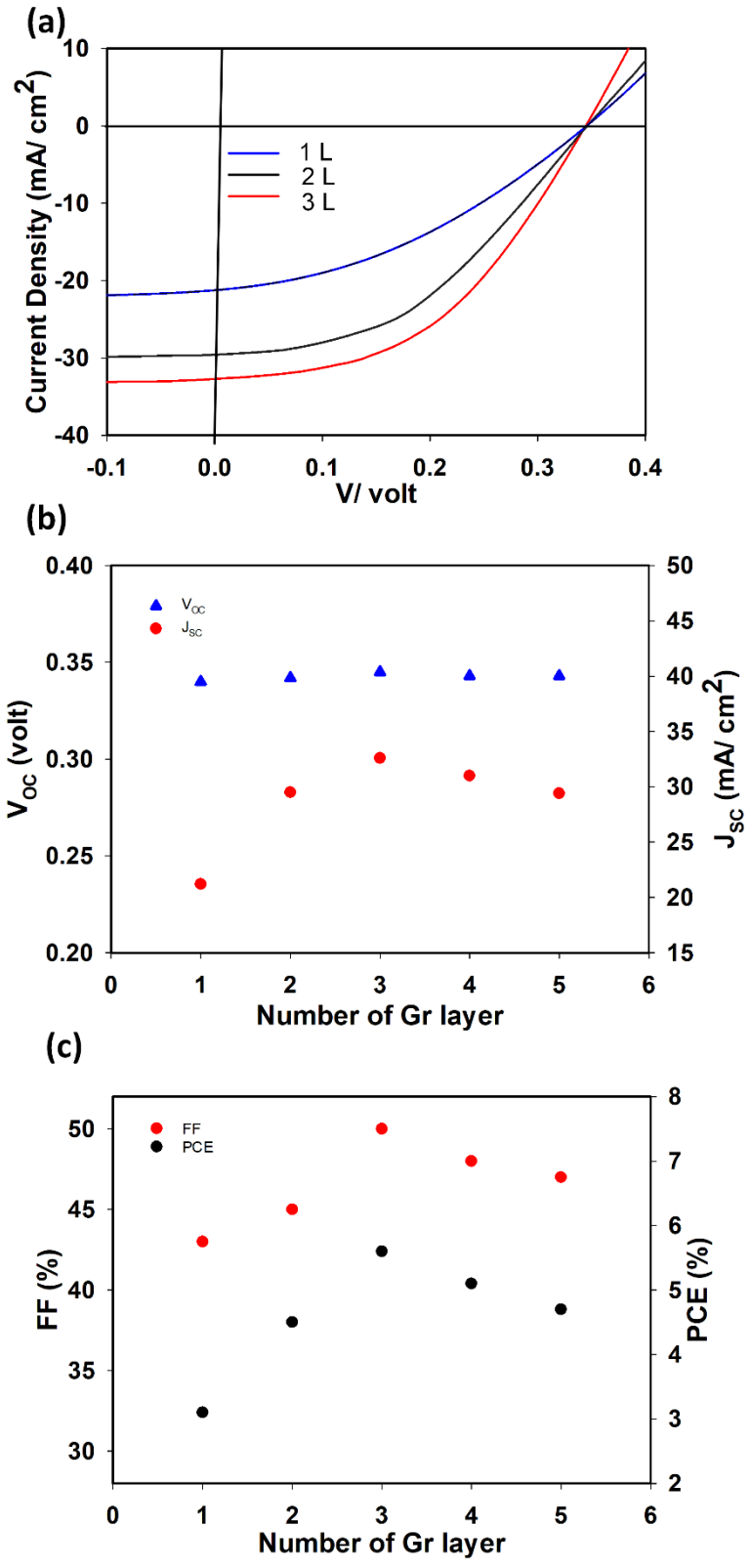

Figure 5- 5 (a, b, and c) *J-V* curves and developed parameters of devices made of a varied number of layers.

of devices, the treatment was methodically applied throughout a range of periods. Figures 5.4a, 5.4b and 5.4c show how the photovoltaic properties of different devices improved after being submerged in formamide for varying amounts of time. The results showed that after being submerged for 5.5 hours, the J_{SC} considerably increased, rising from 14.71 to 21.23 mA/cm^2. It resulted in an increase in the *FF* from 23.2 to 43.3% and a rise in the *PCE* from 1.42 to 3.143%, as shown. Besides, it can be noticed that the dipping treatment period of 5.5 hours developed the *PCE* by more than twofold compared to that of the samples before the dipping process.

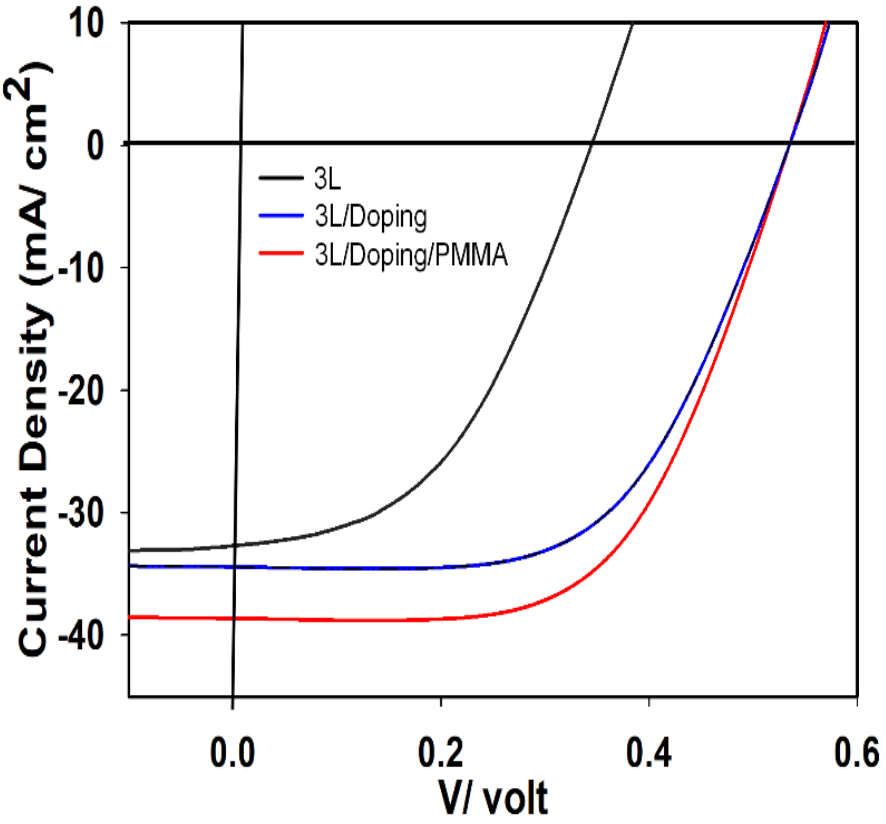

Figure 5- 6 J-V of graphene/n-Si Schottky junction solar cells with multiple graphene layers before and after doping.

The factors of devices submerged for longer than 5.5 hours had saturation values, as shown in Figures 5.4b and 5.4c, respectively. In addition, it lends credence to the notion that the reaction time of 5.5 hours between the samples and the formamide reaching the point of saturation, making it the optimal dipping time for the reduction of residue. As can also be seen in Fig. 5.4b, the V_{OC} of the devices decreases with increasing amounts of time spent submerged in the chemical solutions. This further demonstrates that the amount of PMMA residue that was left behind was reduced. After the treatment, I_D-V_G curves of GFETs also show a shift in the Dirac points in the direction of a lower voltage (from 23 to 15 V), indicating that the residue of PMMA decreases (see Fig. 5.4d). The four-probe measurement also shows that the sheet resistivity of GFET samples dipped for 5.5 h was 240 Ohm/sq. When the formamide process had reached its peak efficiency after 5.5h, multi-graphene layers, known as MGL, were included. Each layer of graphene was given the optimal treatment of formamide. The measured *J-V* of devices that have been manufactured with more than one layer is presented in Fig. 5.5. Compared to the *J-V* curves of devices created

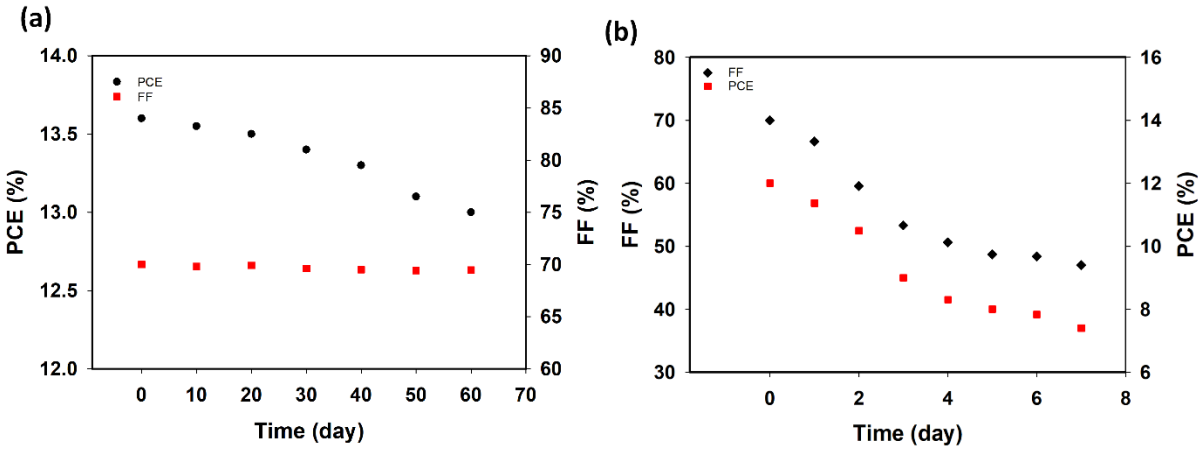

Figure 5- 7 (a) and (b) *PCE* and *FF* values of doped and stored solar cells with and without coated PMMA films.

with a mono-graphene layer, the *J-V* curves of devices prepared with a multi-graphene layer exhibit a substantial expansion. Additionally, it was discovered that the *FF* and *PCE* increased from 43 to 50 % and from 3.1 to 5.6 %, respectively (see Figs. 5.5b and 5.5c). Devices with 3MGLs also had a J_{SC} of 33.2 mA/cm^2, and a V_{OC} of 0.344 V. This finding indicates that the *PCE* and *FF* moved forward by approximately 75% and 25%, respectively. It also demonstrates that MGL successfully improved the fill factor of devices after the residue was reduced. The developed factors for devices treated with more than three layers of graphene are also shown in Figures 5.5b and 5.5c, respectively. As the transparency of graphene layers with more than three layers has been reduced, it is possible to detect that the corresponding factors of devices have experienced a minor drop. Once more, it demonstrates that the optimal number of graphene layers for achieving high solar cell efficiency is three. The doping procedure was reached by using HNO_3 for ninety seconds to improve the performance of the samples further. In Figure 5.6, comparisons of *J-V* curves of devices before and after doping can be seen. After doping, the photovoltaic characteristics of the devices were as follows: a *PCE* of 12%, *FF* of 70%, J_{SC} of 34.4 mA/cm^2, and V_{OC} of 0.5 V. After putting the doping method into effect, it has been shown that there are significant increases in the performance of the device. These enhancements are accomplished by increasing the graphene's conductivity, which leads to the benefits mentioned earlier. Nevertheless, because dopants evaporate with time, the efficiency of devices that have been doped decreases during that period of time (as shown in Fig. 5.7b). Devices were coated with PMMA, so the problem of evaporation was solved. During this process, the relevant values for coated devices were as follows: a *PCE* of 13.6%, *FF* of 70%, J_{SC} of 38.6 mA/cm^2, and V_{OC} of 0.5 V. (see Fig. 5.6). Comparison with

devices that have not been coated, it is clear that coated PMMA layers contribute to an improvement in the values of J_{SC}. The coated layers also minimize the reflection that is produced by devices as described in the previous chapter. In addition, as shown in Figure 5.7a, coated devices made with PMMA layers retain a high degree of stability even after being exposed to air for a period of two months. The *PCE* of the devices used in this process was 13%, which indicates that after being stored, the devices recalled about 95% of their previous performance. In contrast, the *PCE* for non-coated devices was 7.6%, which indicates that these devices lost around 55% of their initial state, as seen in Fig.5.7b. In the light of this information, it is evident that the coating process, in comparison to previous work, notably enhances the stability of the doped devices.

5.3 Ammonia-treated novel graphene/n-Si Schottky junction solar cells

The procedure for preparing graphene/silicon solar cells is depicted in Figure 5.8. Ammonia solution was used to dip samples. Hence, molecules of NH_3 are located on the surface of the graphene. Analyses using Raman spectroscopy were carried out to judge the influence of the reduction on the unaltered graphene. The spectra of transferred graphene before and after dipping are displayed in Figure 5.9a. It is possible to see in Fig. 5.9a that the G and 2D-bands of samples submerged in ammonia for two hours are at 1594 and 2692 cm^{-1}, respectively, which suggests a red shift in the spectra of graphene samples obtained after they have been soaked in ammonia, in contrast to samples immersed in acetone. The red shift again proves that the amount of PMMA residue has decreased. Studies using XPS were carried out to investigate the decrease of the PMMA residue. The corresponding XPS spectra of graphene samples are shown in Figures 5.9b and 5.9d. These compare samples before and after the residue was reduced. It has been demonstrated that

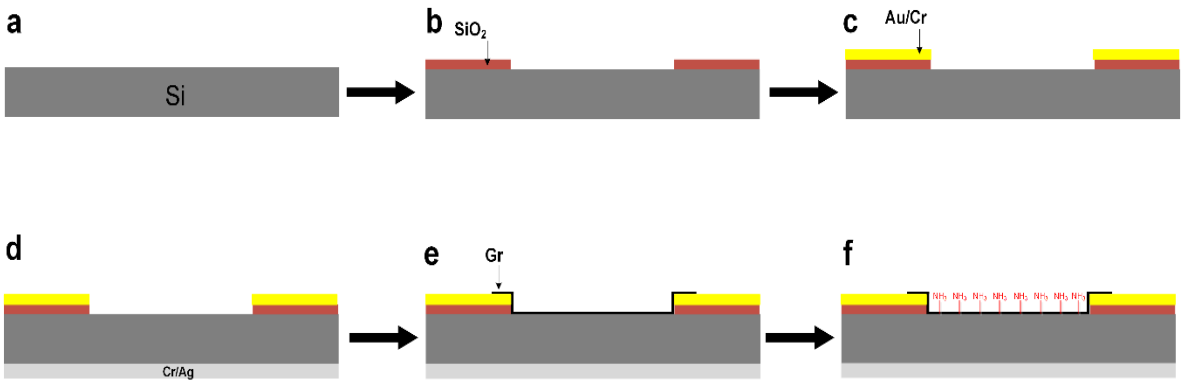

Figure 5- 8 Top-window structure preparation process of solar cell devices. (a), (b), (c) and (d) Cleaning Si substrate, forming SiO_2 and contacts. (e) Transferring a graphene layer onto substrates. (f) Immersing sample in ammonia.

dipping graphene in ammonia results in a great improvement in the sp^2 component of the material compared to graphene in its natural state of acetone and formamide PMMA, specifically sp^3, C-O, and C=O, exhibit a clear decrease following the treatments when they are compared with those of the graphene in its natural state. It suggests that the chemical treatments accomplished by both solutions effectively reduced the amount of PMMA residue that remained after the process. Besides, the ammonia treatments remove more residue as the components of the residue were reduced, compared with the residue found after other procedures. The *J-V* measurements of the samples before and after the dipping operation are displayed in Fig.5.10a. The *PCE*, *FF*, J_{SC}, and V_{OC} of the samples before the dipping operation (with acetone treatment, black line) are the same as those described in Section 5.2. (shown in Fig.5.9c). Moreover, other components of the residue of Photovoltaic values of 3.6%, 47%, 22.3 mA/cm^2, and 0.345 V were measured for the samples treated with ammonia (red line) for two hours. This improvement demonstrates that removing the residue is the most effective way for obtaining optimal *J-V* curves with exceptional

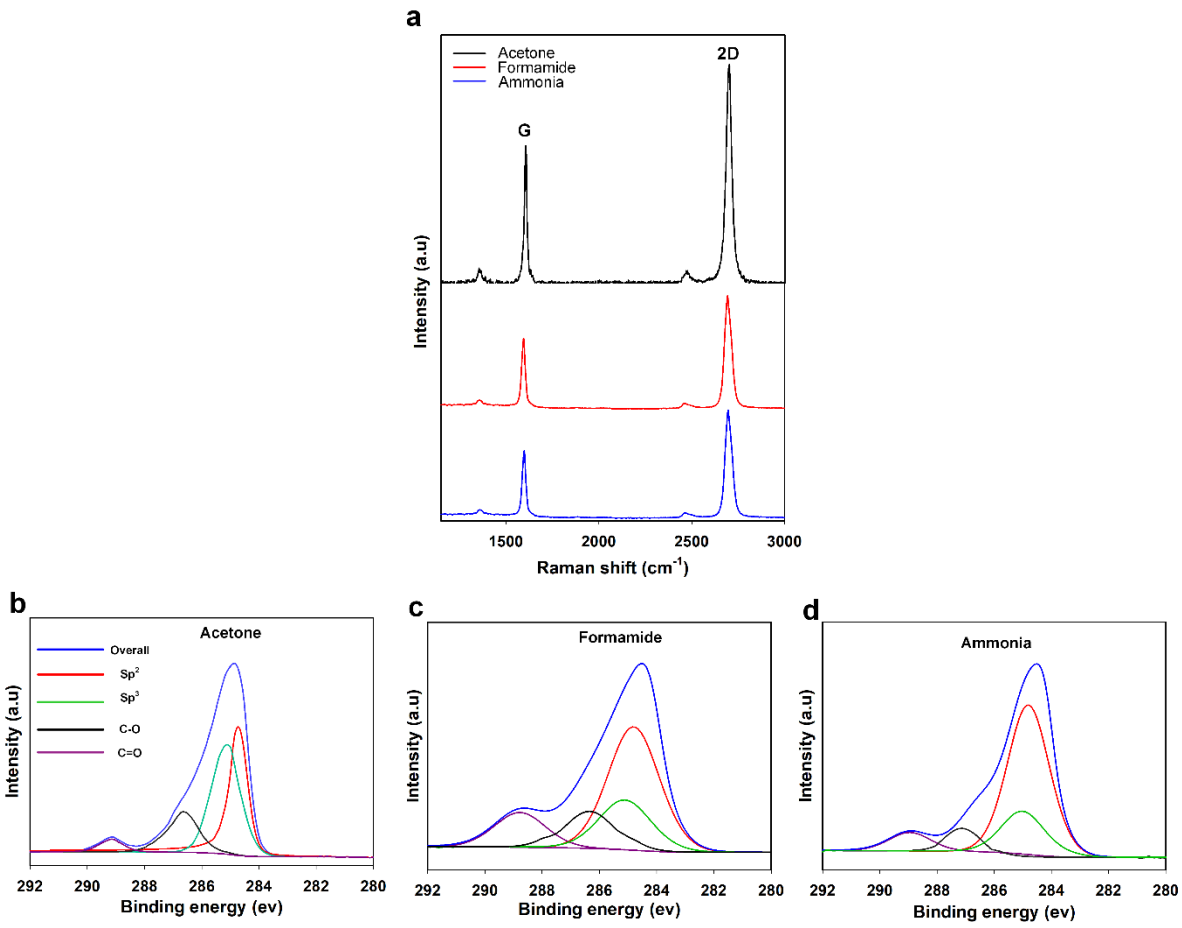

Figure 5- 9 Transferred graphene data of Raman (a) and XPS (b,c and d) before and after chemical treatments.

factors in graphene/Si Schottky junction solar cells. It also shows that the procedure using ammonia is simpler, faster and more efficient in eliminating the residue than a formamide method. This assumes that the adsorption of ammonia on graphene is better than that of formamide. This is because molecules of ammonia are smaller than those of formamide, and it is the reason for the significant improvement of devices processed with ammonia. The EQE analysis of samples similarly verifies that applying ammonia to devices results in higher efficiency than that of undipped devices (see Fig. 5.10b). This shows that the results obtained from the *J-V* curves are consistent

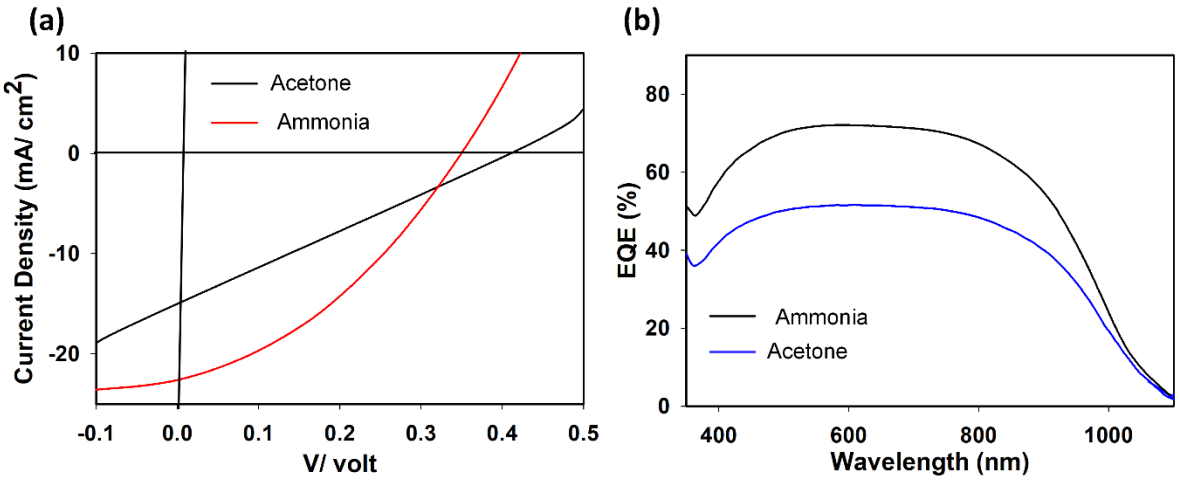

Figure 5- 10 (a) and (b) J-V characteristics and EQE spectra of graphene/Si Schottky solar cells before and after ammonia procedure, respectively.

with the EQE finding. In the next stage, the ammonia treatment was methodically investigated throughout a variety of periods to explore the impact on the functioning of the devices. Figure 5.11a illustrates how the photovoltaic characteristics of devices improved after submersion in ammonia for varying amounts of time. After treatment lasting for two hours, the J_{SC} showed a substantial increase, ranging from 14.7 to 22.3 mA/cm^2. The results showed that there is an increase in the *FF* from 23 to 47% and a rise in the *PCE* from 1.4 to 3.6%. It can be noticed that the dipping treatment duration of two hours extended the *PCE* by greater than three times compared to that of samples before the dipping treatment. The saturation threshold was attained for the factors of devices submerged for more than two hours, as shown in Figures 5.11b and 5.11c, which lends credence to the notion that the reaction time of two hours between the samples and the ammonia achieved the saturation threshold. This is the optimal dipped time (2h) for reducing residue. Similarly, it suggests that the reaction period between the samples and the ammonia should be saturated; at this time, the amount of residue was reduced to its most effective level.

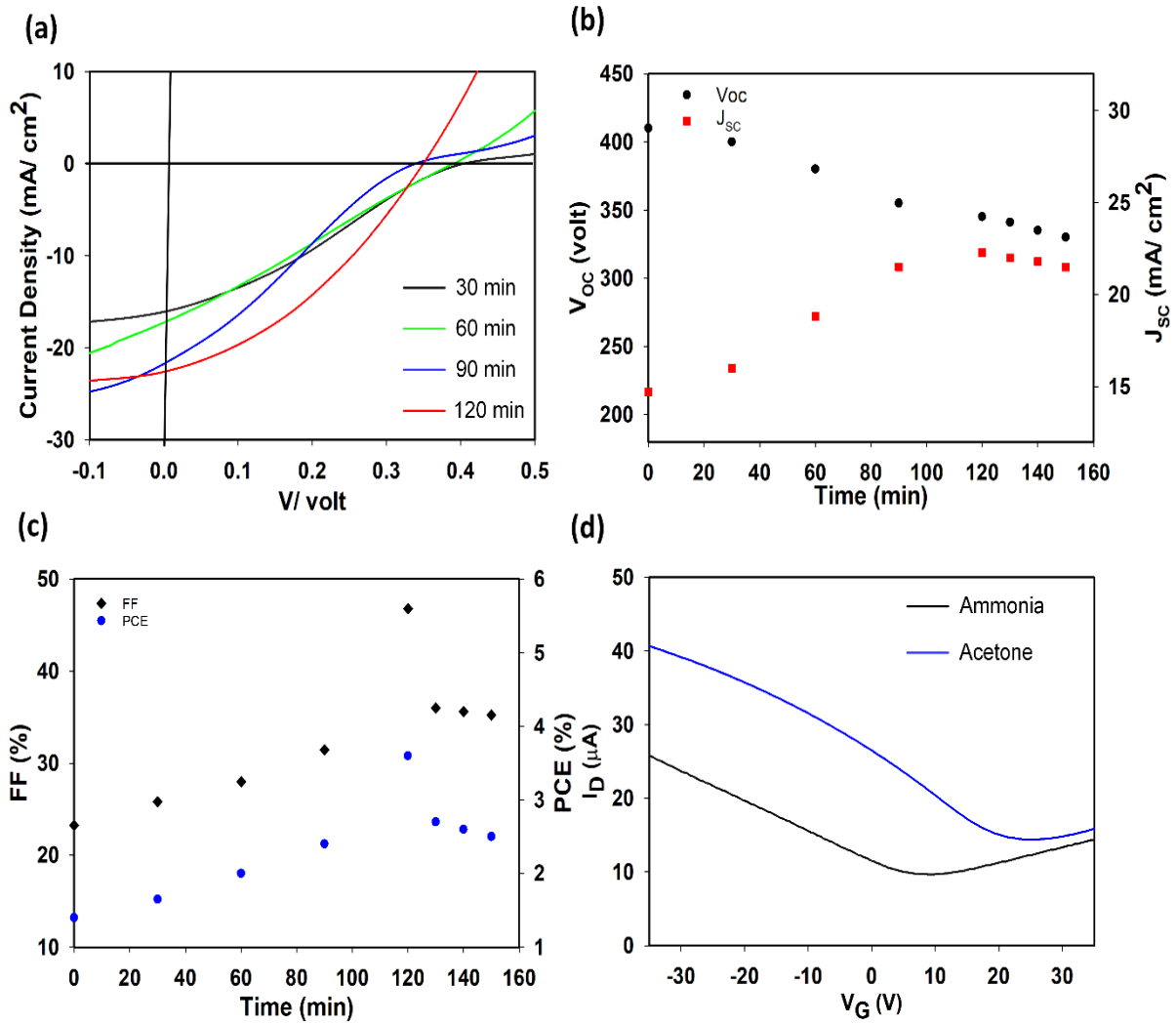

Figure 5- 11 (a), (b) and (c) J-V curves and enhanced factors of graphene/n-Si Schottky junction solar cells dipped in Formamide for various periods. (d) (I_D-V_G) curves of GFETs before and after chemical treatment in the air at room temperature and V_D = 0.1 V.

As can be seen in Fig. 5.11b, the V_{OC} of the devices decreases with increasing amounts of time spent submerged in ammonia. This further substantiates the finding that the amount of PMMA residue left after the treatment is decreased. GFETs were also prepared to examine the shift of Dirac points after the treatment. I_D-V_G curves confirm that a shift in the Dirac points towards a lower voltage (from 23 to 9 V) was obtained, indicating that the residue of PMMA decreases after the ammonia

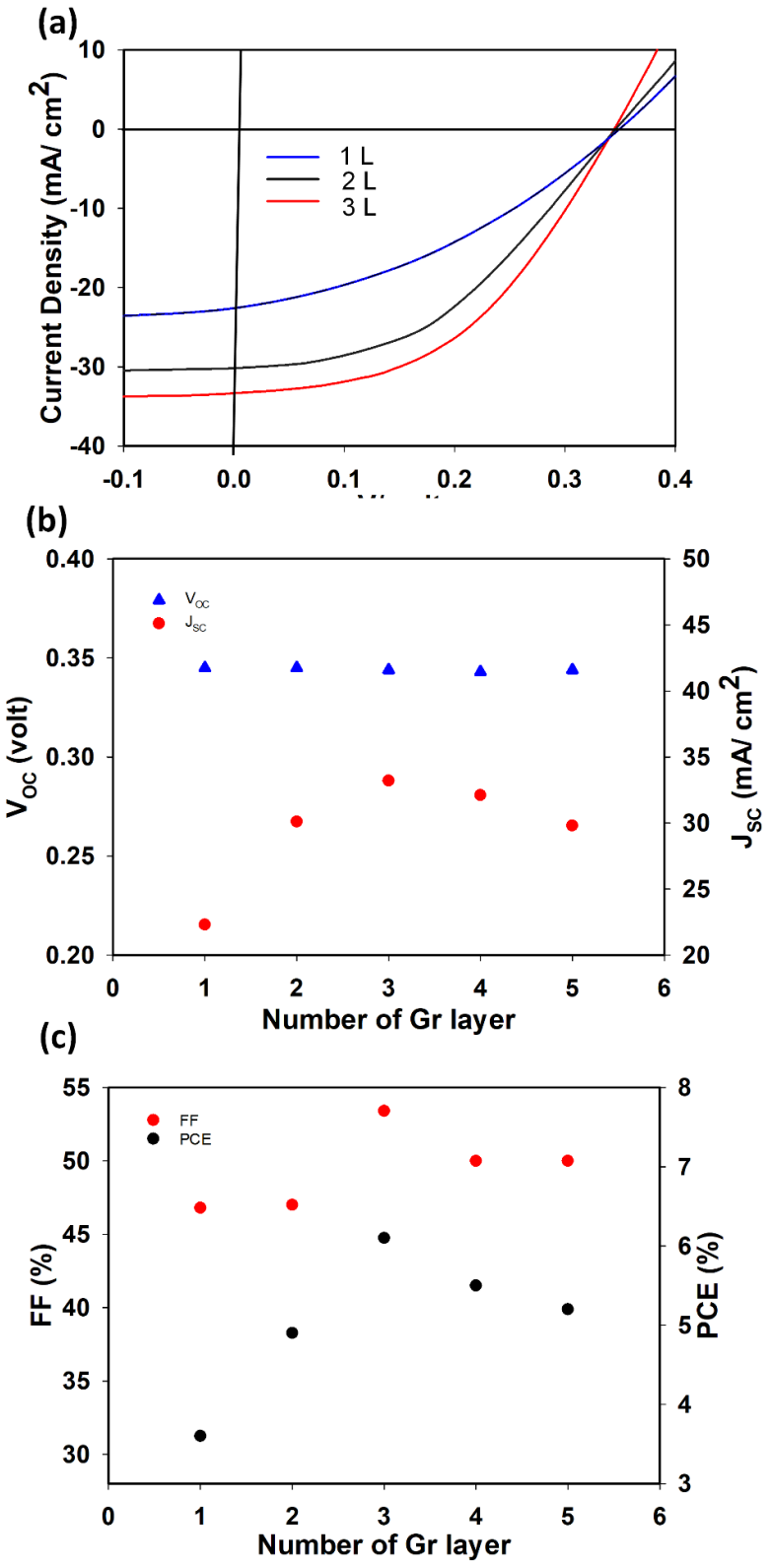

Figure 5- 12 (a), (b) and (c) *J-V* curves and improved factors of graphene/n-Si Schottky junction solar cells prepared with various layers of transferred graphene after chemical treatments.

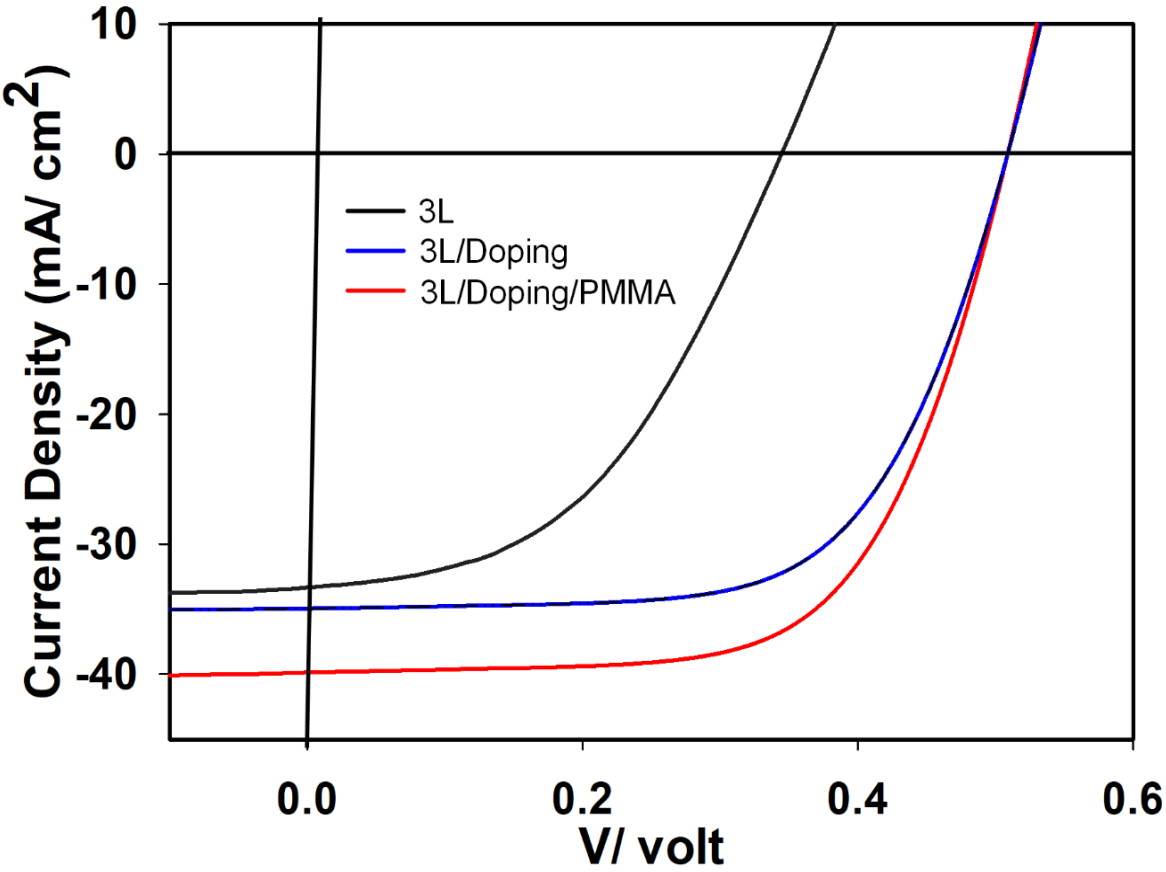

Figure 5- 13 J-V behaviours of graphene/n-Si Schottky junction solar cells that have been produced using three layers of graphene before and after doping.

treatment (see Fig. 5.11d). The sheet resistivity of samples dipped for 2 h was about 225 Ohm/sq. The methodology of MGL was also applied to further improve the *FF* of devices after minimizing the residue by ammonia treatment for each graphene layer. Fig. 5.12 presents the determined *J-V* of devices prepared with multi-graphene layers that bathed in ammonia. The *J-V* curves of devices show a sizable growth compared with devices prepared with more than a mono-graphene layer. 3 MGL devices had a *PCE* of 6.31%, *FF* of 55%, J_{SC} of 33.32 mA/cm^2 and V_{OC} of 0.3445 V. This indicates that the *PCE* and *FF* expanded by about 75% and 25%. This also shows that MGL successfully improved the fill factor of devices after the reduction of

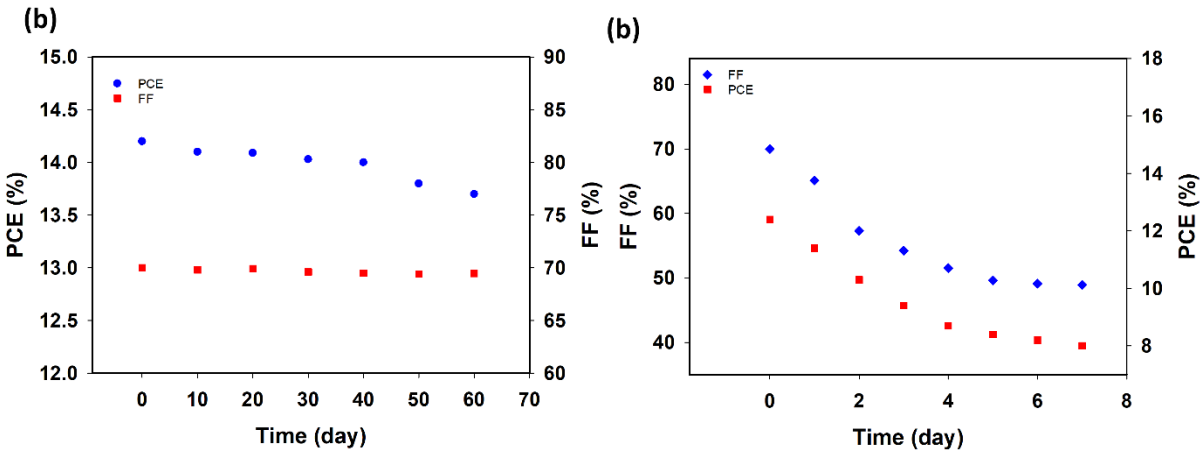

Figure 5- 14 PCE and *FF* values of doped and stored graphene/Si Schottky solar cells with and without coated PMMA layers, respectively, are shown in (a) and (b), respectively.

the residue. Additionally, it can be seen that MGL devices that were dipped in ammonia had greater efficiency than that of devices dipped in the formamide solution. The developed factors of devices prepared with more than three graphene layers were calculated, as shown in Figs. 5.12 b and 5.12c. It can be stated that the relating factors of devices faintly diminished since the transparency of more than 3 graphene layers declined. This verifies the finding that three graphene layers are ideal for obtaining high solar cell efficiency. The efficiency of 6.3% is an innovative finding associated with those described devices that were processed without annealing in forming gas, doping, texturing procedures and anti-reflection coatings. The doping procedure using HNO_3 was introduced to explore its impact on the development of device performance. After doping, the extracted values, which were obtained from Figure 5.13, of devices were as follows: a *PCE* of 12.4%, *FF* of 70%, J_{SC} of 34.9 mA/cm^2, and V_{OC} of 0.51 V. After putting the doping method into effect, it has been shown that there are significant increases in the performance of the device. These enhancements are accomplished by increasing the conductivity of doped graphene layers, which leads to the benefits mentioned earlier. Nevertheless, since dopants evaporate

with time, the efficiency of devices that have been doped will decrease over time. The PMMA was used to cover the doped graphene layers so that dopants would not suffer from evaporation. The associated metrics of coated devices for this technique were a *PCE* of 14.2%, *FF* of 70%, J_{SC} of 39.8 mA/cm^2, and V_{OC} of 0.51 V (see Fig. 5.13). When compared to devices that have not been coated, it is clear that coated PMMA layers contribute to an improvement in the values of J_{SC}, due to reduction of the reflection from Si substrates. In addition, as shown in Figure 5.14a, coated devices made with PMMA layers retain a high degree of stability even after being exposed to air for two months. The performance coefficient of *PCE* for devices used in this step was 13.7%, which indicates that the devices recalled more than 95% of their performance after being stored. On the other hand, the *PCE* for non-coated devices was 7.6%, which indicates that these devices lost 55% of their starting state, as seen in Figure 5.14b. In light of this information, it is clear that the coating process, when compared to earlier efforts, significantly expands the stability of doped devices.

5.3 Conclusion

In this chapter, two novel methods that make use of solutions of formamide and ammonia were presented. Both approaches effectively remove any trace of PMMA, ultimately leading to improvements in device functionality. Moreover, it was discovered that the ammonia method is more effective and requires less time than the formamide method. Since molecules of ammonia are smaller than those of formamide. It is assumed that the adsorption of ammonia on graphene will be better than that of formamide. This is the reason for the significant improvement of devices processed with ammonia. Correspondingly, the fill factor was effectively enhanced by employing multi-graphene layers rather than monolayer graphene to achieve the Schottky junction for devices after reducing PMMA

residue, which increased efficiency. After going through the doping procedure with HNO_3, the devices' performance rose even higher. With the addition of an encapsulated PMMA layer, the doped devices similarly demonstrated remarkable performances, with a *PCE* of 14.2% and stability for two months.

6. Conclusions and future work

6.1 Summary

A new method for fabricating graphene/Si Schottky junction solar cells has been introduced. This process simplifies the fabrication of samples by eliminating the need for the complex etching of the top window SiO_2, as reported in previous works. In the current work, conventional lithography and sputtering were employed to form a SiO_2/Ag/Au top window. Sputtered SiO_2 with a thickness of 250 nm was found to be sufficient to produce this window. Research into how the performance of devices was affected by the thickness of SiO_2 was conducted. Three methods were used to reduce the PMMA residue left behind after the wet transfer procedure and enhance the performance of the devices.

The combination method (including annealing and DUV) is the first technique, and it takes three steps to minimize the amount of PMMA residue. The first step is to expose the PMMA to the DUV for ten minutes, leading to weakening the chemical bonds that hold the PMMA together and making the PMMA more soluble. After completing the previous step, the PMMA was subjected to an acetone treatment. The residue was effectively removed during annealing in forming gas, which is the third step, for three hours. This process effectively results in ideal curves of prepared devices. Chemical treatments were the second and third techniques for removing the residue. The two techniques simplify the elimination process of the residue compared with the previous technique (annealing). It was found that applying formamide treatment for 5.5 h efficiently eliminated the residue without annealing, where samples were dipped in this solution after the acetone treatment. Additionally, it was found that using ammonia treatment for 2 h is more efficient in the elimination of the residue

compared with formamide. This also means that the ammonia treatment is the fastest and simplest technique for removing the residue compared with others. Raman spectroscopy and XPS were used to investigate the transferred graphene's inherent physical characteristics. Both of these instruments confirmed no trace of the high amount of residue left behind. When the reduction procedure of residue was applied, *J-V* curves were ideal. Because of this, there is a significant improvement in the overall performance of devices. By using more than one layer of graphene to produce the Schottky junction, the fill factor of the devices raised even further, compared to the efficiency of devices manufactured using a mono-graphene layer. This results in a significant improvement in efficiency. The doping technique contributed to further increase the effacement of samples. The problem of reported instability in the published works was solved by encapsulating the doped graphene layer. That was accomplished by putting a layer of PMMA onto the top of doped graphene layers. Consequently, it is feasible to derive the following conclusions regarding the contributions made to the body of knowledge resulting of this work:

- An innovative method for the production of graphene/silicon Schottky junction solar cells using a sputtering approach to simplify the previous fabrication process.
- Investigating the causes of the s-shape observed in *J-V* curves in graphene/Si solar cells, which adversely affects the solar cell performance.
- Applying three innovative approaches for getting rid of the PMMA residue that was left behind, leading to an efficient improvement in solar cell performance.

- The development of a fill factor for devices was accomplished by reducing the residue, using multi-graphene layers and doping.
- Introducing a developed technique using a capsulated PMMA layer to achieve stable and highly efficient doped devices for about 2 months.
- An efficiency of about 17% was recorded, which is comparable to that of commercial p-n junction Si solar cells. Furthermore, the current fabrication process is simpler than that of Si p-n solar cells.

6.2 Future work

The research significantly improved the performance of graphene/n-Si Schottky junction solar cells by adding multiple graphene-free residue layers and doping procedures. As a result, the efficiency of the cells is now comparable to that of devices made of p-n junctions. Moreover, the methods developed in this study can be applied in the construction of graphene/p-Si Schottky junction solar cells. Because of the residue, this category of devices has a tough time creating n-type graphene that is efficient and stable. As a result, cutting-edge techniques for eliminating residue may be used. Next, n dopants may be used to create the n-graphene layer. In order to generate stable n graphene, a layer of PMMA that has been coated onto devices will be applied at the end. In order to develop graphene/p-Si Schottky junction solar cells, it is essential to research this task, which means that it is highly vital to investigate. The free leftover graphene produced in this work could be used in a manufacturing process of heterojunction intrinsic thin-layer (HIT) and perovskite solar cells. The functionality of devices may improve as a result. The impact of graphene area on the performance of graphene solar cells is another potential research topic for the future work. The efficiency of graphene/silicon Schottky junction solar cells will be significantly

boosted due to an increase in the active area of samples. Furthermore, the use of reduced graphene oxide (rGO) rather than CVD-graphene in the process of fabricating graphene/Si Schottky junction solar cells may result in a reduction in the overall cost of the process.

7. List of Resources

1. Mbayachi, V.B., et al., *Graphene synthesis, characterization and its applications: A review.* Results in Chemistry, 2021. 3: p. 100163.
2. Green, M.A., *Solar cells: operating principles, technology, and system applications.* 1982.
3. Nelson, J., *The physics of solar cells*. 2003: World Scientific Publishing Co Inc.
4. Goetzberger, A. and V.U. Hoffmann, *Photovoltaic solar energy generation*. Vol. 112. 2005: Springer Science & Business Media.
5. Sze, S.M. and K.K. Ng, *Physics of semiconductor devices*. 2006: John wiley & sons.
6. Shockley, W. and W. Read Jr, *Statistics of the recombinations of holes and electrons.* Physical review, 1952. 87(5): p. 835.
7. Soga, T., *Nanostructured materials for solar energy conversion*. 2006: Elsevier.
8. McDonald, D. and A. Cuevas, *Reduced fill factors in multicrystalline silicon solar cells due to injection-level dependent bulk recombination lifetimes.* 2000.
9. Meemongkolkiat, V., *Development of high efficiency monocrystalline silicon solar cells through improved optical and electrical confinement*. 2008: Georgia Institute of Technology.
10. McIntosh, K.R., *Lumps, humps and bumps: Three detrimental effects in the current-voltage curve of silicon solar cells*. 2001: University of New South Wales.
11. Taguchi, M., et al., *HITTM cells—high-efficiency crystalline Si cells with novel structure.* Progress in Photovoltaics, 2000. 8(5): p. 503-514.
12. Hall, R.N., *Electron-hole recombination in germanium.* Physical Review, 1952. 87(2): p. 387.
13. Dziewior, J. and W. Schmid, *Auger coefficients for highly doped and highly excited silicon.* Applied Physics Letters, 1977. 31(5): p. 346-348.
14. Sinton, R.A. and R.M. Swanson, *Recombination in highly injected silicon.* Electron Devices, IEEE Transactions on, 1987. 34(6): p. 1380-1389.
15. Altermatt, P.P., et al., *Assessment and parameterisation of Coulomb-enhanced Auger recombination coefficients in lowly injected crystalline silicon.* Journal of Applied Physics, 1997. 82(10): p. 4938-4944.
16. Schlangenotto, H., H. Maeder, and W. Gerlach, *Temperature dependence of the radiative recombination coefficient in silicon.* physica status solidi (a), 1974. 21(1): p. 357-367.
17. Green, M.A., *The path to 25% silicon solar cell efficiency: History of silicon cell evolution.* Progress in Photovoltaics: Research and Applications, 2009. 17(3): p. 183-189.
18. Macleod, H. and T.-F.O. Filters, *Macmillan Publishing Company.* New York, 1986.
19. Ali, K., S.A. Khan, and M.M. Jafri, *Enhancement of silicon solar cell efficiency by using back surface field in comparison of different antireflective coatings.* Solar Energy, 2014. 101: p. 1-7.
20. Birmann, K., M. Zimmer, and J. Rentsch, *Fast alkaline etching of monocrystalline wafers in KOH/CHX.* 23rd European PVSEC, 2008.
21. Chu, A., et al., *A simple and cost-effective approach for fabricating pyramids on crystalline silicon wafers.* Solar Energy Materials and Solar Cells, 2009. 93(8): p. 1276-1280.
22. King, D.L. and M.E. Buck. *Experimental optimization of an anisotropic etching process for random texturization of silicon solar cells*. in *Photovoltaic Specialists Conference, 1991., Conference Record of the Twenty Second IEEE*. 1991. IEEE.
23. Palik, E.D., *Gallium Arsenide (GaAs).* Handbook of optical constants of solids, 1985. 1: p. 429-443.

24. Masuko, K., et al., *Achievement of more than 25% conversion efficiency with crystalline silicon heterojunction solar cell.* IEEE Journal of Photovoltaics, 2014. 4(6): p. 1433-1435.
25. Schroder, D.K., N.R. Thomas, and J.C. Swartz, *Free carrier absorption in silicon.* Solid-State Circuits, IEEE Journal of, 1978. 13(1): p. 180-187.
26. Standard, A., *G173,"Standard Tables for Reference Solar Spectral Irradiances: Direct Normal and Hemispherical on 37 Tilted Surface," Amer.* Society for Testing Matls., West Conshocken PA, USA, 2007.
27. Yablonovitch, E., *Statistical ray optics.* JOSA, 1982. 72(7): p. 899-907.
28. Yablonovitch, E. and G.D. Cody, *Intensity enhancement in textured optical sheets for solar cells.* Electron Devices, IEEE Transactions on, 1982. 29(2): p. 300-305.
29. Goetzberger, A. *Optical confinement in thin Si-solar cells by diffuse back reflectors*. in *15th Photovoltaic Specialists Conference*. 1981.
30. Ramanujam, J. and U.P. Singh, *Copper indium gallium selenide based solar cells–a review.* Energy & Environmental Science, 2017. 10(6): p. 1306-1319.
31. Kettle, J., et al., *Review of technology specific degradation in crystalline silicon, cadmium telluride, copper indium gallium selenide, dye sensitised, organic and perovskite solar cells in photovoltaic modules: Understanding how reliability improvements in mature technologies can enhance emerging technologies.* Progress in Photovoltaics: Research and Applications, 2022. 30(12): p. 1365-1392.
32. Bonnet, D., *Cadmium telluride solar cells.* Clean electricity from photovoltaics, 2001: p. 245-269.
33. Mitzi, D.B., K. Chondroudis, and C.R. Kagan, *Organic-inorganic electronics.* IBM journal of research and development, 2001. 45(1): p. 29-45.
34. Neukom, M.T., *Charge carrier dynamics of methylammonium lead-iodide perovskite solar cells.* arXiv preprint arXiv:1611.06425, 2016.
35. Riazimehr, S., et al., *High Photocurrent in Gated Graphene-Silicon Hybrid Photodiodes.* ACS Photonics, 2017.
36. Li, X., et al., *Graphene-on-silicon Schottky junction solar cells.* Advanced Materials, 2010. 22(25): p. 2743-2748.
37. M. Green, K.E., D.L. King, SIgari, W. Warta, *Progress in Photovoltaics, Research and Applications.* Research and Applications, 2005. 1349e1354
38. Kray, D., et al. *Comprehensive experimental study on the performance of very thin laser-fired high-efficiency solar cells*. in *Proceedings of the 19th European Photovoltaic Solar Energy Conference*. 2004. WIP Renewable Energies Paris, France.
39. Ralph, E.L., Proceedings of 11th IEEE Photovoltaics Specialist Conference, 1975: p. 315.
40. Saga, T., *Advances in crystalline silicon solar cell technology for industrial mass production.* npg asia materials, 2010. 2(3): p. 96-102.
41. Wronski, C.R. and D.E. Carlson, *Amorphous silicon solar cells*. Vol. 199. 2001: Imperial College Press, London, UK.
42. Miles, R., K. Hynes, and I. Forbes, *Photovoltaic solar cells: An overview of state-of-the-art cell development and environmental issues.* Progress in Crystal Growth and Characterization of Materials, 2005. 51(1-3): p. 1-42.
43. Staebler, D. and C. Wronski, *Reversible conductivity changes in discharge-produced amorphous Si.* Applied Physics Letters, 1977. 31(4): p. 292-294.
44. Wu, B.-S., et al. *Hybrid multi-layer graphene/Si Schottky junction solar cells*. in *Photovoltaic Specialists Conference (PVSC), 2013 IEEE 39th*. 2013. IEEE.
45. Abbas, A., et al. *The effect of cadmium chloride treatment on close spaced sublimated cadmium telluride thin film solar cells*. in *2012 IEEE 38th Photovoltaic Specialists Conference (PVSC) Part 2*. 2012. IEEE.

46. Dharmadasa, I., et al., *Fabrication of CdS/CdTe-based thin film solar cells using an electrochemical technique.* Coatings, 2014. 4(3): p. 380-415.
47. Barbato, M., et al., *CdTe solar cells: technology, operation and reliability.* Journal of Physics D: Applied Physics, 2021. 54(33): p. 333002.
48. Visoly-Fisher, I., et al., *Factors affecting the stability of CdTe/CdS solar cells deduced from stress tests at elevated temperature.* Advanced Functional Materials, 2003. 13(4): p. 289-299.
49. Klinkert, T., *Compréhension et optimisation du dépôt de Cu (In, Ga) Se2 par co-évaporation en tant qu'absorbeur pour le développement de cellules solaires en couches minces à très haut rendement*. 2015, Paris 6.
50. Theelen, M., *Degradation of CIGS solar cells.* 2015.
51. Repins, I., et al. *Characterization of 19.9%-efficient CIGS absorbers*. in *2008 33rd IEEE photovoltaic specialists conference*. 2008. IEEE.
52. Stolt, L. *Solibro CIGS to the next level*. in *5th International Workshop on CIGS Solar Cell Technology*. 2014.
53. Khoshsirat, N. and N.A.M. Yunus, *Copper-Indium-Gallium-Diselenide (CIGS) nanocrystalline bulk semiconductor as the absorber layer and its current technological trend and optimization.* Nanoelectronics and Materials Development, 2016: p. 41.
54. Dhere, N.G., *Present status and future prospects of CIGSS thin film solar cells.* Solar energy materials and solar cells, 2006. 90(15): p. 2181-2190.
55. Sinha, S., et al., *A review on atomic layer deposited buffer layers for Cu (In, Ga) Se2 (CIGS) thin film solar cells: Past, present, and future.* Solar Energy, 2020. 209: p. 515-537.
56. Saji, V.S., I.-H. Choi, and C.-W. Lee, *Progress in electrodeposited absorber layer for CuIn (1− x) GaxSe2 (CIGS) solar cells.* Solar Energy, 2011. 85(11): p. 2666-2678.
57. Chopra, K., P. Paulson, and V. Dutta, *Thin-film solar cells: an overview.* Progress in Photovoltaics: Research and applications, 2004. 12(2-3): p. 69-92.
58. Spear, W. and P. Le Comber, *Substitutional doping of amorphous silicon.* Solid state communications, 1975. 17(9): p. 1193-1196.
59. Carlson, D.E. and C.R. Wronski, *Amorphous silicon solar cell.* Applied Physics Letters, 1976. 28(11): p. 671-673.
60. Canham, L.T., *Silicon quantum wire array fabrication by electrochemical and chemical dissolution of wafers.* Applied physics letters, 1990. 57(10): p. 1046-1048.
61. Dyer, A.C.R., *Synergism between single event effects and total ionising dose*. 2015: University of Surrey (United Kingdom).
62. Lu, J., *Biomolecular sensing using wavelength-scanning reflective interferometry (ws-RI)*. 2006: University of Rochester.
63. Green, M.A., *Crystalline and thin-film silicon solar cells: state of the art and future potential.* Solar energy, 2003. 74(3): p. 181-192.
64. Goodrich, A., et al., *A wafer-based monocrystalline silicon photovoltaics road map: Utilizing known technology improvement opportunities for further reductions in manufacturing costs.* Solar Energy Materials and Solar Cells, 2013. 114: p. 110-135.
65. Musztyfaga-Staszuk, M., A. Czupryński, and R. Radev, *Review of the chosen methods of producing front contacts to transparent conductive oxides layers in photovoltaic structures.* Energies, 2022. 15(23): p. 9026.
66. Arici, E., et al., *Core/shell nanomaterials in photovoltaics.* International Journal of Photoenergy, 2003. 5(4): p. 199-208.
67. Sariciftci, N.S., et al., *Photoinduced electron transfer from a conducting polymer to buckminsterfullerene.* Science, 1992. 258(5087): p. 1474-1476.
68. Yu, G., et al., *Polymer photovoltaic cells: enhanced efficiencies via a network of internal donor-acceptor heterojunctions.* Science, 1995. 270(5243): p. 1789-1791.

69. Smestad, G.P., et al., *A technique to compare polythiophene solid-state dye sensitized TiO2 solar cells to liquid junction devices.* Solar Energy Materials and Solar Cells, 2003. 76(1): p. 85-105.
70. Gebeyehu, D., et al., *Hybrid solar cells based on dye-sensitized nanoporous TiO2 electrodes and conjugated polymers as hole transport materials.* Synthetic Metals, 2001. 125(3): p. 279-287.
71. Sicot, L., et al., *Dye sensitized polythiophene solar cells.* Synthetic metals, 1999. 102(1-3): p. 991-992.
72. Beek, W.J., M.M. Wienk, and R.A. Janssen, *Hybrid solar cells from regioregular polythiophene and ZnO nanoparticles.* Advanced Functional Materials, 2006. 16(8): p. 1112-1116.
73. Alivisatos, A.P., *Semiconductor clusters, nanocrystals, and quantum dots.* science, 1996. 271(5251): p. 933-937.
74. Huynh, W.U., J.J. Dittmer, and A.P. Alivisatos, *Hybrid nanorod-polymer solar cells.* science, 2002. 295(5564): p. 2425-2427.
75. Greenham, N.C., X. Peng, and A.P. Alivisatos, *Charge separation and transport in conjugated-polymer/semiconductor-nanocrystal composites studied by photoluminescence quenching and photoconductivity.* Physical review B, 1996. 54(24): p. 17628.
76. McDonald, S.A., et al., *Solution-processed PbS quantum dot infrared photodetectors and photovoltaics.* Nature materials, 2005. 4(2): p. 138-142.
77. Arici, E., N.S. Sariciftci, and D. Meissner, *Hybrid solar cells based on nanoparticles of CuInS2 in organic matrices.* Advanced Functional Materials, 2003. 13(2): p. 165-171.
78. Arici, E., N.S. Sariciftci, and D. Meissner, *Hybrid solar cells.* Encyclopedia of Nanoscience and Nanotechnology, 2004. 3: p. 929-944.
79. Grätzel, M., *Solar energy conversion by dye-sensitized photovoltaic cells.* Inorganic chemistry, 2005. 44(20): p. 6841-6851.
80. Nogueira, A., C. Longo, and M.-A. De Paoli, *Polymers in dye sensitized solar cells: overview and perspectives.* Coordination Chemistry Reviews, 2004. 248(13-14): p. 1455-1468.
81. Grätzel, M., *Perspectives for dye-sensitized nanocrystalline solar cells.* Progress in photovoltaics: research and applications, 2000. 8(1): p. 171-185.
82. Halme, J., *Performance limiting factors in flexible dye solar cells*. 2009: Teknillinen korkeakoulu.
83. Günes, S. and N.S. Sariciftci, *Hybrid solar cells.* Inorganica Chimica Acta, 2008. 361(3): p. 581-588.
84. Alferov, Z.I., *State-of-the art and prospects of A III B V science and technology.* Czechoslovak Journal of Physics B, 1980. 30(3): p. 245-261.
85. Rappaport, P., *The photovoltaic effect and its utilization.* Solar Energy, 1959. 3(4): p. 8-18.
86. Wagner, S., et al., *p− InP/n− CdS solar cells and photovoltaic detectors.* Applied Physics Letters, 1975. 26(5): p. 229-230.
87. Green, M.A., et al., *Solar cell efficiency tables (version 26).* Progress in Photovoltaics: Research and Applications, 2005. 13(5): p. 387-392.
88. Shi, Z. and A.H. Jayatissa, *Perovskites-Based Solar Cells: A Review of Recent Progress, Materials and Processing Methods.* Materials, 2018. 11(5).
89. Jeon, N.J., et al., *Compositional engineering of perovskite materials for high-performance solar cells.* Nature, 2015. 517(7535): p. 476.
90. Kojima, A., et al., *Organometal halide perovskites as visible-light sensitizers for photovoltaic cells.* Journal of the American Chemical Society, 2009. 131(17): p. 6050-6051.
91. Saliba, M., et al., *Cesium-containing triple cation perovskite solar cells: improved stability, reproducibility and high efficiency.* Energy & environmental science, 2016. 9(6): p. 1989-1997.
92. Ye, Y., et al., *Schottky junction photovoltaic devices based on CdS single nanobelts.* Nanotechnology, 2009. 20(37): p. 375202.

93. Zhou, Z., et al., *Schottky solar cells with amorphous carbon nitride thin films prepared by ion beam sputtering technique.* Solar energy materials and solar cells, 2002. 70(4): p. 487-493.
94. Luther, J.M., et al., *Schottky solar cells based on colloidal nanocrystal films.* Nano letters, 2008. 8(10): p. 3488-3492.
95. Sun, Y., Q. Wu, and G. Shi, *Graphene based new energy materials.* Energy & Environmental Science, 2011. 4(4): p. 1113-1132.
96. Ye, Y. and L. Dai, *Graphene-based Schottky junction solar cells.* Journal of Materials Chemistry, 2012. 22(46): p. 24224-24229.
97. Beams, R., L.G. Cançado, and L. Novotny, *Raman characterization of defects and dopants in graphene.* Journal of Physics: Condensed Matter, 2015. 27(8): p. 083002.
98. Peres, N., *The transport properties of graphene.* Journal of Physics: Condensed Matter, 2009. 21(32): p. 323201.
99. Jeong, H.J., et al., *Improved transfer of chemical-vapor-deposited graphene through modification of intermolecular interactions and solubility of poly (methylmethacrylate) layers.* Carbon, 2014. 66: p. 612-618.
100. Kim, K.S., et al., *Large-scale pattern growth of graphene films for stretchable transparent electrodes.* nature, 2009. 457(7230): p. 706.
101. Thomsen, C. and S. Reich, *Double resonant Raman scattering in graphite.* Physical review letters, 2000. 85(24): p. 5214.
102. Saito, R., et al., *Probing phonon dispersion relations of graphite by double resonance Raman scattering.* Physical review letters, 2001. 88(2): p. 027401.
103. Pimenta, M., et al., *Studying disorder in graphite-based systems by Raman spectroscopy.* Physical chemistry chemical physics, 2007. 9(11): p. 1276-1290.
104. Lespade, P., et al., *Caracterisation de materiaux carbones par microspectrometrie Raman.* Carbon, 1984. 22(4-5): p. 375-385.
105. Lucchese, M.M., et al., *Quantifying ion-induced defects and Raman relaxation length in graphene.* Carbon, 2010. 48(5): p. 1592-1597.
106. Cançado, L.G., et al., *Quantifying defects in graphene via Raman spectroscopy at different excitation energies.* Nano letters, 2011. 11(8): p. 3190-3196.
107. Eckmann, A., et al., *Probing the nature of defects in graphene by Raman spectroscopy.* Nano letters, 2012. 12(8): p. 3925-3930.
108. Cancado, L., et al., *Influence of the atomic structure on the Raman spectra of graphite edges.* Physical review letters, 2004. 93(24): p. 247401.
109. Casiraghi, C., et al., *Raman spectroscopy of graphene edges.* Nano letters, 2009. 9(4): p. 1433-1441.
110. Beams, R., L.G. Cançado, and L. Novotny, *Low temperature Raman study of the electron coherence length near graphene edges.* Nano letters, 2011. 11(3): p. 1177-1181.
111. Tuinstra, F. and J.L. Koenig, *Raman spectrum of graphite.* The Journal of Chemical Physics, 1970. 53(3): p. 1126-1130.
112. Saito, R., et al., *Raman spectroscopy of graphene and carbon nanotubes.* Advances in Physics, 2011. 60(3): p. 413-550.
113. Tivanov, M., et al., *Significant G peak temperature shift in Raman spectra of graphene on copper.* Journal of Materials Science: Materials in Electronics, 2016. 27(9): p. 8879-8883.
114. Souza, M., et al., *Single-and double-resonance Raman G-band processes in carbon nanotubes.* Physical Review B, 2004. 69(24): p. 241403.
115. Felten, A., et al., *Radio-frequency plasma functionalization of carbon nanotubes surface O 2, NH 3, and CF 4 treatments.* Journal of applied physics, 2005. 98(7): p. 074308.
116. Jorio, A., et al., *G-band resonant Raman study of 62 isolated single-wall carbon nanotubes.* Physical Review B, 2002. 65(15): p. 155412.
117. Ferrari, A.C., et al., *Raman spectrum of graphene and graphene layers.* Physical review letters, 2006. 97(18): p. 187401.

118. Cançado, L., et al., *Geometrical approach for the study of G' band in the Raman spectrum of monolayer graphene, bilayer graphene, and bulk graphite.* Physical Review B, 2008. 77(24): p. 245408.
119. Lindvall, N., *Towards graphene-based devices: Fabrication and characterization.* 2012.
120. Li, C., *Superconducting proximity effect in graphene and Bi nanowire based junctions*. 2014, Université Paris Sud-Paris XI.
121. Wang, X., et al., *N-doping of graphene through electrothermal reactions with ammonia.* Science, 2009. 324(5928): p. 768-771.
122. Tombros, N., et al., *Electronic spin transport and spin precession in single graphene layers at room temperature.* Nature, 2007. 448(7153): p. 571-574.
123. Katsnelson, M., K. Novoselov, and A. Geim, *Chiral tunnelling and the Klein paradox in graphene.* Nature physics, 2006. 2(9): p. 620-625.
124. Li, X., et al., *Large-area synthesis of high-quality and uniform graphene films on copper foils.* Science, 2009. 324(5932): p. 1312-1314.
125. Wang, Y., et al., *Top-grid monolayer graphene/Si Schottkey solar cell.* Journal of Solid State Chemistry, 2015. 224: p. 102-106.
126. Suhail, A., et al., *Improved efficiency of graphene/Si Schottky junction solar cell based on back contact structure and DUV treatment.* Carbon, 2018. 129: p. 520-526.
127. Xu, Y., et al., *Contacts between two-and three-dimensional materials: Ohmic, schottky, and p–n heterojunctions.* ACS nano, 2016. 10(5): p. 4895-4919.
128. Miao, X., et al., *High efficiency graphene solar cells by chemical doping.* Nano letters, 2012. 12(6): p. 2745-2750.
129. Yang, L., et al., *Interface engineering for efficient and stable chemical-doping-free graphene-on-silicon solar cells by introducing a graphene oxide interlayer.* Journal of Materials Chemistry A, 2014. 2(40): p. 16877-16883.
130. Yu, X., et al., *The enhanced efficiency of graphene-silicon solar cells by electric field doping.* Nanoscale, 2015. 7(16): p. 7072-7.
131. Lin, Y., et al., *Graphene/semiconductor heterojunction solar cells with modulated antireflection and graphene work function.* Energy & Environmental Science, 2013. 6(1): p. 108-115.
132. Shi, E., et al., *Colloidal antireflection coating improves graphene–silicon solar cells.* Nano letters, 2013. 13(4): p. 1776-1781.
133. Song, Y., et al., *Role of interfacial oxide in high-efficiency graphene–silicon Schottky barrier solar cells.* Nano letters, 2015. 15(3): p. 2104-2110.
134. An, X., F. Liu, and S. Kar, *Optimizing performance parameters of graphene–silicon and thin transparent graphite–silicon heterojunction solar cells.* Carbon, 2013. 57: p. 329-337.
135. Shi, Y., et al., *Work function engineering of graphene electrode via chemical doping.* ACS nano, 2010. 4(5): p. 2689-2694.
136. Wadhwa, P., et al., *Electronic junction control in a nanotube-semiconductor Schottky junction solar cell.* Nano letters, 2010. 10(12): p. 5001-5005.
137. Wadhwa, P., et al., *Electrolyte-induced inversion layer Schottky junction solar cells.* Nano letters, 2011. 11(6): p. 2419-2423.
138. Li, X., et al., *Anomalous behaviors of graphene transparent conductors in graphene–silicon heterojunction solar cells.* Advanced Energy Materials, 2013. 3(8): p. 1029-1034.
139. Choi, Y., et al., *The effect of the graphene integration process on the performance of graphene-based Schottky junction solar cells.* Journal of Materials Chemistry A, 2017. 5(35): p. 18716-18724.
140. Cui, T., et al., *Enhanced efficiency of graphene/silicon heterojunction solar cells by molecular doping.* Journal of Materials Chemistry A, 2013. 1(18): p. 5736-5740.
141. Suhail, A.M., *Graphene/silicon Schottky junction solar cells with high efficiency*. 2019, University of Plymouth.

142. Gao, L., et al., *Total color difference for rapid and accurate identification of graphene.* ACS nano, 2008. 2(8): p. 1625-1633.
143. Schrader, B., *Infrared and Raman spectroscopy: methods and applications*. 2008: John Wiley & Sons.
144. Suk, J.W., et al., *Enhancement of the electrical properties of graphene grown by chemical vapor deposition via controlling the effects of polymer residue.* Nano letters, 2013. 13(4): p. 1462-1467.
145. Suhail, A., et al., *Reduction of polymer residue on wet–transferred cvd graphene surface by deep UV exposure.* Applied Physics Letters, 2017. 110(18): p. 183103.
146. Suhail, A., et al., *Effective chemical treatment for high efficiency graphene/si schottky junction solar cells with a graphene back-contact structure.* Advanced Materials Letters, 2017. 8(10): p. 977-982.
147. Suhail, A., et al., *Reduction of polymer residue on wet–transferred CVD graphene surface by deep UV exposure.* Applied Physics Letters, 2017. 110(18).
148. Holder, J.K.L., *Quantum structures in photovoltaic devices*. 2013, University of Oxford.
149. Bhushan, B. and O. Marti, *Scanning probe microscopy–principle of operation, instrumentation, and probes*. 2010: Springer.
150. Abramovitch, D.Y., et al. *A tutorial on the mechanisms, dynamics, and control of atomic force microscopes*. in *2007 American Control Conference*. 2007. IEEE.
151. Novoselov, K.S., et al., *Electric field effect in atomically thin carbon films.* science, 2004. 306(5696): p. 666-669.
152. Lee, Y., et al., *Wafer-scale synthesis and transfer of graphene films.* Nano letters, 2010. 10(2): p. 490-493.
153. Li, X., et al., *Evolution of graphene growth on Ni and Cu by carbon isotope labeling.* Nano letters, 2009. 9(12): p. 4268-4272.
154. Land, T., et al., *STM investigation of single layer graphite structures produced on Pt (111) by hydrocarbon decomposition.* Surface Science, 1992. 264(3): p. 261-270.
155. Nagashima, A., et al., *Electronic states of monolayer graphite formed on TiC (111) surface.* Surface Science, 1993. 291(1): p. 93-98.
156. Li, Z., et al., *Chemical Vapor Deposition Growth of Graphene using Other Hydrocarbon Sources.* arXiv preprint arXiv:1101.5664, 2011.
157. Li, X., et al., *Graphene films with large domain size by a two-step chemical vapor deposition process.* Nano letters, 2010. 10(11): p. 4328-4334.
158. Reina, A., et al., *Growth of large-area single-and bi-layer graphene by controlled carbon precipitation on polycrystalline Ni surfaces.* Nano Research, 2009. 2(6): p. 509-516.
159. Grüneis, A., K. Kummer, and D.V. Vyalikh, *Dynamics of graphene growth on a metal surface: a time-dependent photoemission study.* New Journal of Physics, 2009. 11(7): p. 073050.
160. Wang, H., et al., *Controllable synthesis of submillimeter single-crystal monolayer graphene domains on copper foils by suppressing nucleation.* Journal of the American Chemical Society, 2012. 134(8): p. 3627-3630.
161. Zhang, Y., et al., *Comparison of graphene growth on single-crystalline and polycrystalline Ni by chemical vapor deposition.* The Journal of Physical Chemistry Letters, 2010. 1(20): p. 3101-3107.
162. Yu, J., et al., *Synthesis of high quality two-dimensional materials via chemical vapor deposition.* Chemical science, 2015. 6(12): p. 6705-6716.
163. Li, B., et al., *Deep UV hardening of photoresist for shaping of graphene and lift-off fabrication of back-gated field effect biosensors by ion-milling and sputter deposition.* Carbon, 2017. 118: p. 43-49.
164. Song, Y., et al., *Role of interfacial oxide in high-efficiency graphene–silicon Schottky barrier solar cells.* Nano letters, 2015. 15(3): p. 2104-2110.

165. Schreiber, H.U. and E. Fröschle, *High Quality RF-Sputtered Silicon Dioxide Layers.* Journal of The Electrochemical Society, 1976. 123(1): p. 30.
166. Yu, X., *Transfer-Free Development of Graphene-on-Silicon Heterojunction Solar Cells*. 2017, University of Illinois at Chicago.
167. Xie, C., et al., *Monolayer graphene film/silicon nanowire array Schottky junction solar cells.* Applied Physics Letters, 2011. 99(13): p. 133113.
168. Jiao, T., et al., *Flexible solar cells based on graphene-ultrathin silicon Schottky junction.* Rsc Advances, 2015. 5(89): p. 73202-73206.
169. Yu, X., et al., *The enhanced efficiency of graphene–silicon solar cells by electric field doping.* Nanoscale, 2015. 7(16): p. 7072-7077.
170. Jehad, A.K., *Preparation and Characterization of Different Graphene Based-Materials and Investigation in Graphene*. 2021, Dokuz Eylul Universitesi (Turkey).
171. Alnuaimi, A.A.R., *Graphene Synthesis and Interface Engineering for Graphene/Silicon Schottky Junction Solar Cells.* 2017.
172. Kim, S.H., et al., *Performance optimization in gate-tunable Schottky junction solar cells with a light transparent and electric-field permeable graphene mesh on n-Si.* Journal of Materials Chemistry C, 2017. 5(12): p. 3183-3187.
173. Wu, B.-S., et al. *Hybrid multi-layer graphene/Si Schottky junction solar cells*. in *2013 IEEE 39th Photovoltaic Specialists Conference (PVSC)*. 2013. IEEE.
174. Tongay, S., et al., *Stable hole doping of graphene for low electrical resistance and high optical transparency.* Nanotechnology, 2011. 22(42): p. 425701.
175. Singh, E. and H.S. Nalwa, *Stability of graphene-based heterojunction solar cells.* RSC Advances, 2015. 5(90): p. 73575-73600.
176. Li, C., et al., *Performance improvement of graphene/silicon solar cells via inverted pyramid texturation array.* Silicon, 2022. 14(16): p. 10485-10493.

8. Appendix

8.1 Lithography Designs

Various patterns have been developed and employed for the shaping and production of devices.

8.1.1 Designs for gFET devices

Fig. A-1 displays the patterns utilized for creating the 7-electrode gFET device with an adjacent channel length of 90 µm. It also illustrates the design for shaping a graphene channel with a length of 720 µm and a width of 80 µm

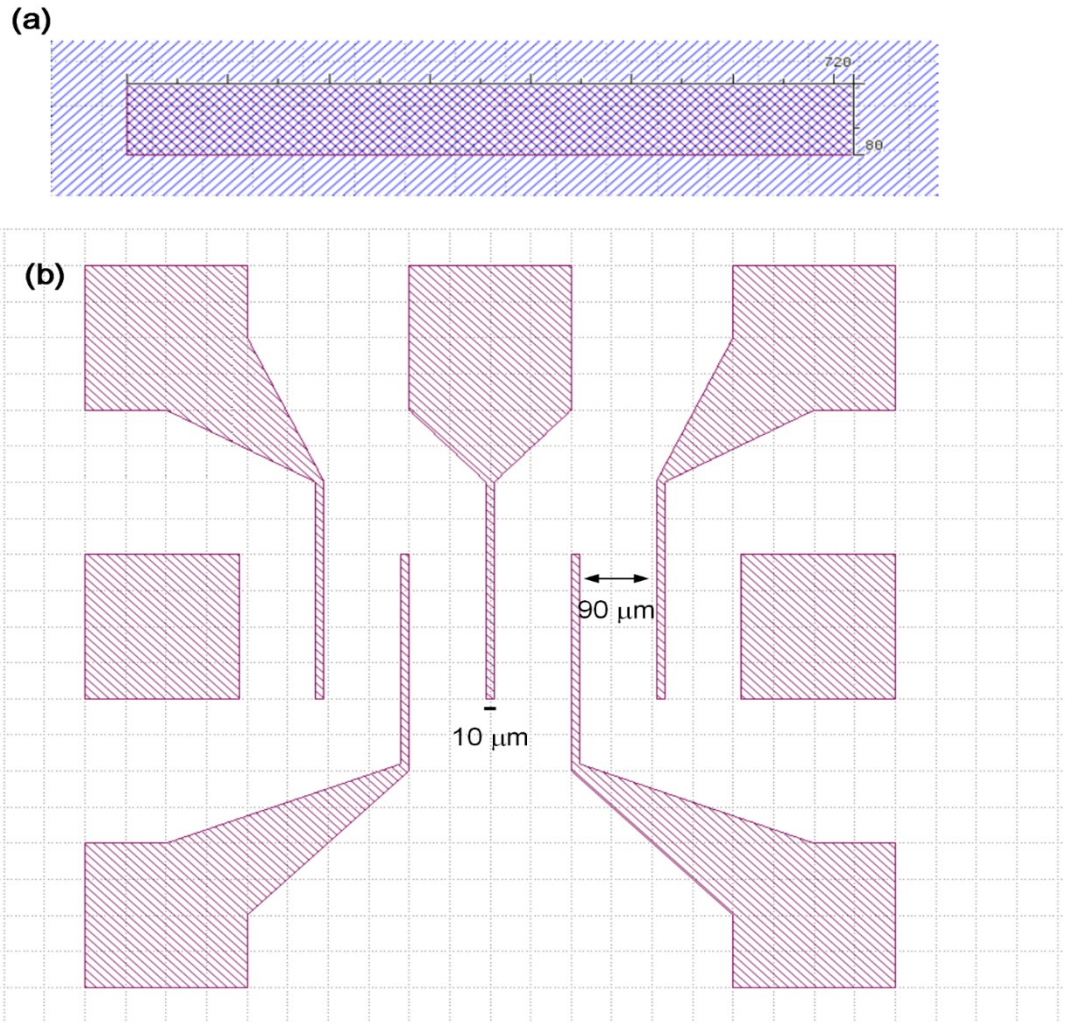

Figure A- 1 Designs for creating the 7-electrode device. (a) and (b) represent the graphene shaping channels and electrode deposition designs, respectively.

8.1.2 Schottky junction graphene/Si solar cells designs

The diagram in Fig. A-2 illustrates the fabrication process for graphene/Si Schottky junction solar cells with an area of 0.1 cm^2.

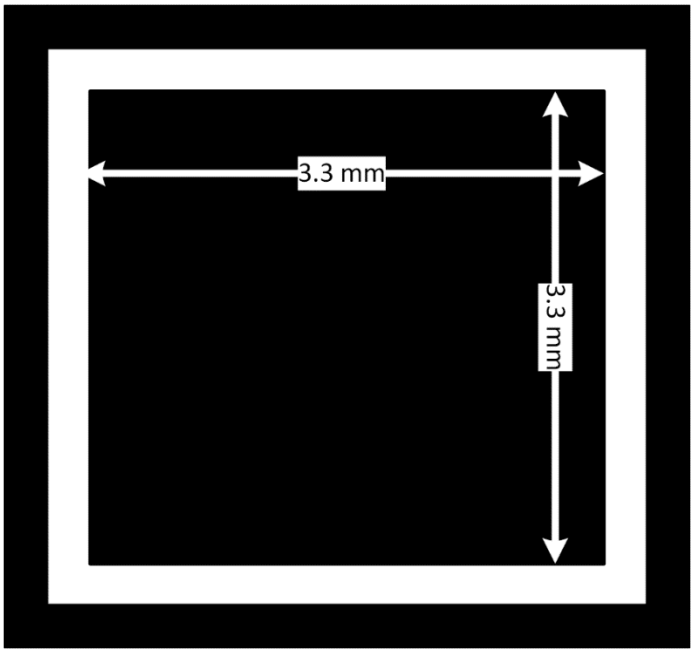

Figure A- 2 A Schottky junction fabrication for graphene/Si solar cell.

8.2 Materials

4-inch Au target, 99.99% purity (*Kurt J. Lesker, US*)

4-inch Si (200 µm) wafer (*Siltronix, US*)

4-inch Si (500 µm) wafer with 300nm SiO_2 (*Siltronix, US*)

5-inch Ag target, 99.99% purity (*Kurt J. Lesker, US*)

6-inch Cr target, 99.99% purity (*Kurt J. Lesker, US*)

7-inch SiO_2 target (*Kurt J. Lesker, US*)

Acetone, general purpose grade (*BDH chemicals LTD, UK*)

Ammonium hydroxide, NH_4OH *(Sigma-Aldrich, UK)*

Ammonium persulfate, $(NH_4)_2S_2O_8$ *(Sigma-Aldrich, UK)*

Argon/Hydrogen, Ar/H_2 (*BOC, UK*)

DUV light (*UVP, UK*)

Fan Oven (*WTB binder, Germany*)

Formamide, CH_3NO *(Sigma-Aldrich, UK)*

Graphene (*Graphene Supermarket, USA*)

Hotplate SH8 (*STUART SCIENTIFIC*)

Hydrochloric acid, 37%HCl (*Fisher scientific, UK)*

Hydrogen fluoride, HF *(Sigma-Aldrich, UK)*

Hydrogen peroxide, 27%H_2O_2 *(Sigma-Aldrich, UK)*

IPA, general purpose grade (*BDH Chemicals LTD, UK*)

Liquid nitrogen (*BOC, UK*)

Microposit developer 351 (*Rohm and has electrical materials Europe, UK*)

Microposit remover 1165 (*Rohm and has electrical materials Europe, UK*)

Nitric acid, 70%HNO_3 *(Sigma-Aldrich, UK)*

Oxygen-free nitrogen, N_2 (*BOC, UK*)

Poly (methyl methacrylate), PMMA *(Sigma-Aldrich, UK)*

Potassium hydroxide, KOH *(Sigma-Aldrich, UK)*

Pure argon, Ar (*BOC, UK*)

S1805 Positive photoresist (*Rohm and has electrical materials Europe, UK*)

Sulfuric acid, H_2SO_4 *(Sigma-Aldrich, UK)*

Ultrasonic Cleaner (*CBEST, US*)

Vacuum spinner 14E (*DAGE PRECIMA INTERNATIONAL*)

8.3 Supporting data

8.3.1 Improved fabrication process of graphene/Si Schottky junction solar cells

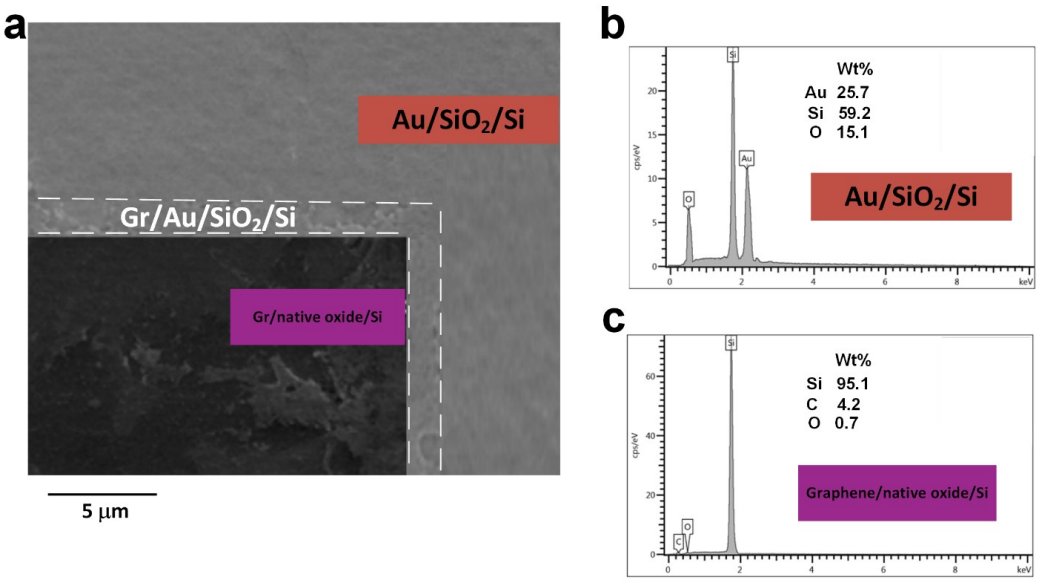

Figure A- 3 (a) SEM image of the topography of graphene/Si Schottky . (b) and (c) EDS spectra of Au/ SiO_2/Si and graphene/native oxide/Si layers for prepared devices with sputtered 50 nm SiO_2.

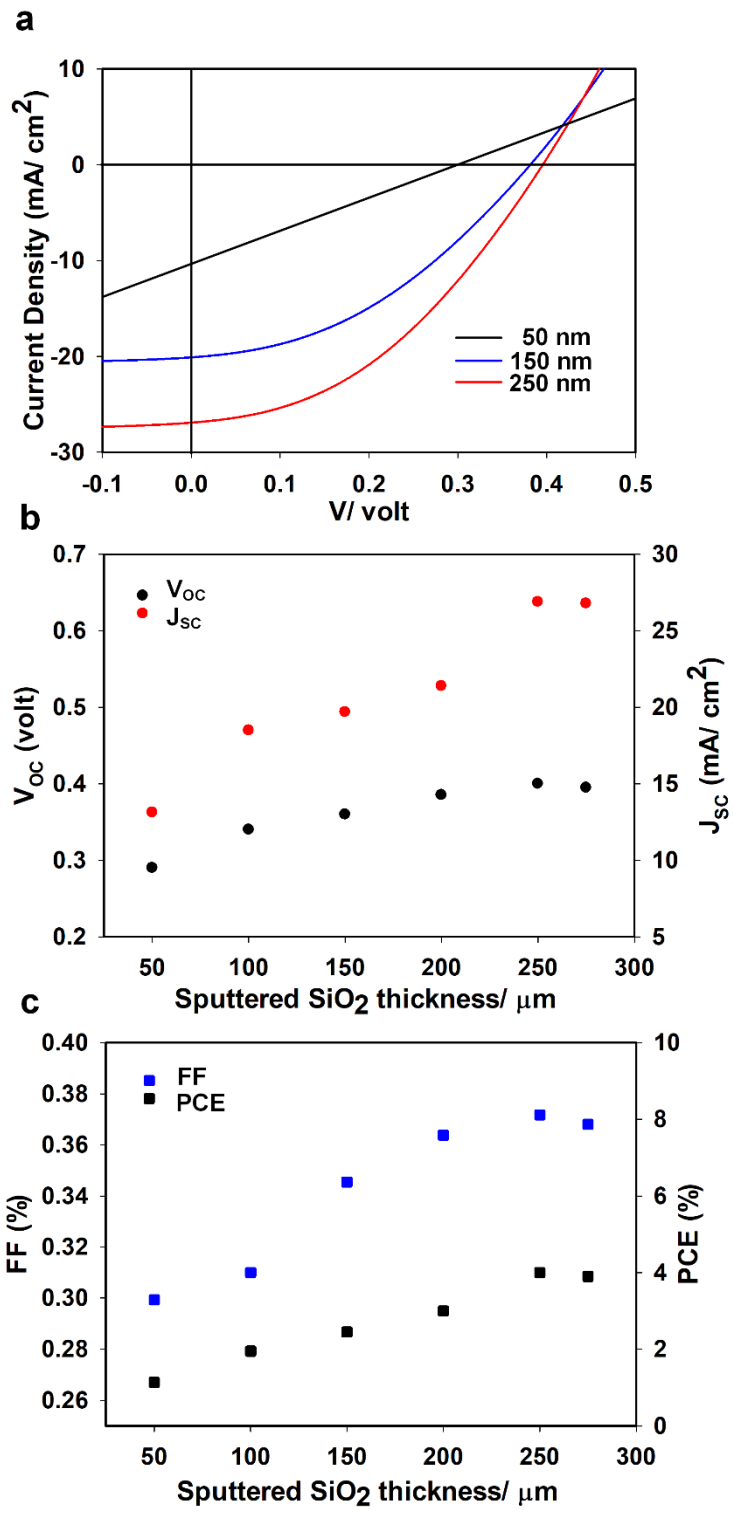

Figure A- 4 (a) SiO_2 patterns of different thicknesses prepared to get J-V curves of graphene/n-Si Schottky junction solar cells. (b) and (c) different thicknesses of SiO_2 patterns prepared to developments of V_{OC}, J_{SC}, FF, and PCE.

7.5.3 Developed performance of devices prepared with multigraphene layers and the combination process

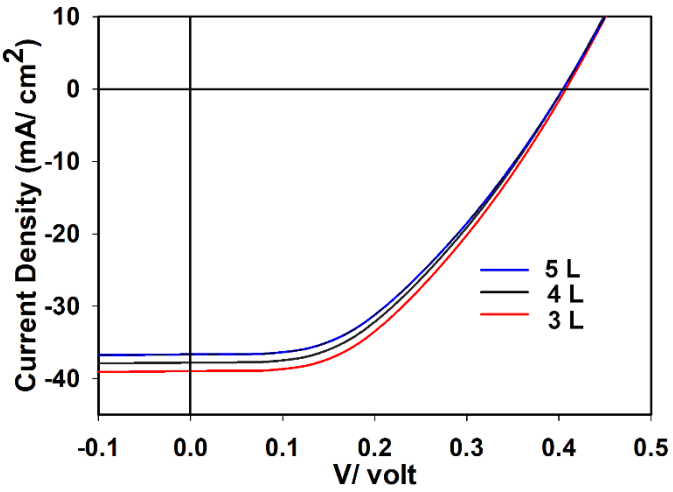

Figure A- 5 J-V curves of graphene/n-Si Schottky junction solar cells prepared with a different number of graphene layers, indicating the ideal 3 graphene layers for prepared devices.

7.5.4 Developed wet transfer process based on chemical treatments

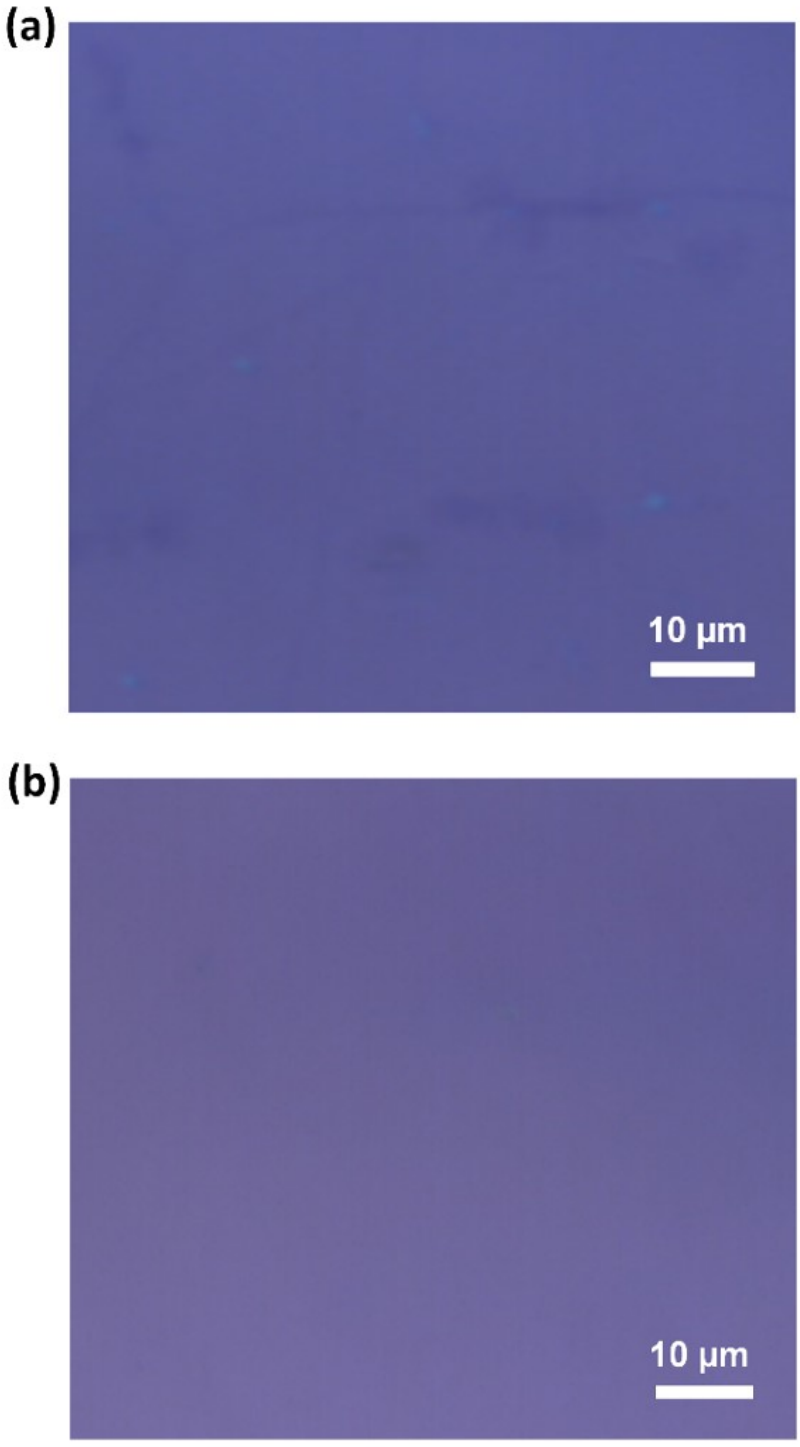

Figure A- 6 Optical images labelled as (a) and (b) of transferred graphene show the graphene before and after chemical treatments, revealing dark spots associated with the PMMA residue..